# Gradient-Free Aeroacoustic Shape Optimization Using High-Order Implicit Large Eddy Simulation

Mohsen Hamedi

A Thesis

In the Department

of

Mechanical, Industrial, and Aerospace Engineering

Presented in Partial Fulfillment of the

Requirements for the Degree of

Doctor of Philosophy (Mechanical Engineering)

at Concordia University

Montreal, Quebec, Canada

January 2024

**CONCORDIA UNIVERSITY SCHOOL**

**OF GRADUATE STUDIES**

This is to certify that the thesis

prepared By: *Mohsen Hamedi*

Entitled: *Gradient-Free Aeroacoustic Shape Optimization Using High-Order Implicit Large Eddy Simulation*

and submitted in partial fulfillment of the requirements for the degree of

DOCTOR OF PHILOSOPHY (Mechanical Engineering)

complies with the regulations of the University and meets the accepted standards with respect to originality and quality.

Signed by the final Examining Committee:

_____ Chair
*Dr. Jerin John*

_____ External Examiner
*Dr. Luc Mongeau*

_____ Arm's Length Examiner
*Dr. Sheng Samuel Li*

_____ Examiner
*Dr. Mojtaba Kheiri*

_____ Examiner
*Dr. Hoi Dick Ng*

_____ Thesis Supervisor
*Dr. Brian Vermeire*

Approved by _____
Graduate Program Director, *Dr. Muthukumaran Packirisamy*

January 30, 2024 _____
Dean, *Dr. Mourad Debbabi*

# ABSTRACT

**Gradient-Free Aeroacoustic Shape Optimization Using High-Order Implicit Large Eddy Simulation**

**Mohsen Hamedi, Ph.D.**

**Concordia University, 2024**

Aviation noise poses significant challenges to both the quality of life for those living near airports and the sustainable growth of the aviation industry. Accurate aeroacoustic shape optimization methods are required to reduce this noise. To address this, we propose an innovative approach for aeroacoustic shape optimization using Large Eddy Simulation (LES). The gradient-free Mesh Adaptive Direct Search (MADS) algorithm minimizes sound pressure levels for observers at varying distances. Near-field predictions rely on a high-order unstructured flow solver, while far-field predictions employ an acoustic solver based on the Ffowcs Williams and Hawkings (FW-H) time-domain formulation. The acoustic solver is verified and validated using analytical test cases and comparison with results obtained directly from the flow solver. The optimization framework is implemented in parallel, enabling concurrent objective function evaluations at each iteration. This removes the dependency of the computational runtime of the MADS algorithm on the total number of design variables, given the availability of sufficient resources. Different problems are considered to evaluate the performance of the proposed optimization framework, including flow over a deep open cavity, tandem cylinders configuration, and a NACA 4-digit airfoil. Initially, noise reduction for a near-field observer is addressed for these geometries under low Reynolds numbers and in two-dimensional settings. Subsequently, the approach is extended to three dimensions, and finally, shape optimization is conducted to minimize noise for a far-field observer. The results affirm the efficacy of the proposed optimization framework by significant noise reduction across all cases.

# Acknowledgements

First and foremost, I would like to extend my deepest and most heartfelt gratitude to my wife, Hora. Throughout the entire journey of my studies, she has been my unwavering source of support. Her patience and boundless love have carried me through the most challenging times. Over the past year, as I devoted myself to my studies, Hora bore the immense responsibility of caring for our precious daughter, ensuring that she had the love, care, and attention she needed. Her sacrifice was immeasurable. Hora's determination, her unwavering support, and her belief in my aspirations have been the cornerstone of my success. I am profoundly grateful to have her as my partner in life, and I dedicate my academic achievements to her.

My heartfelt thanks go to my parents, Mohammad Hossein and Fatemeh, whose unwavering support has been a constant source of strength and encouragement throughout my life. Despite being separated by thousands of kilometres, their love, guidance, and selflessness have bridged the distance. Their belief in my dreams and their willingness to support me have been an enduring source of inspiration. My accomplishments are a testament to their love and guidance, and I am forever indebted to them for their boundless support.

I would like to extend my warmest gratitude to my supervisor, Dr. Brian Vermeire, whose mentorship and guidance have been invaluable throughout my academic journey. His unwavering commitment to fostering the intellectual growth of his students is truly remarkable. From the earliest hours of the morning to the late hours of the night, Brian was there, patiently addressing my questions and pushing me to explore the depths of engineering. Brian not only improved my technical skills but also illuminated a path towards personal growth. His dedication to excellence and his ability to teach not just engineering but also how to be a better human being have had a profound impact on me. My academic journey would not have been the same without Brian's exceptional guidance.

Last but not least, I would like to acknowledge my labmates, who have made our lab an enjoyable and vibrant environment. The insightful discussions, the sharing of concerns, and the camaraderie have been invaluable. I want to extend special thanks to Carlos for his unwavering

support and valuable discussions. Whenever I faced disappointments or hurdles in my thesis, you were there to help and motivate me. I also want to thank Hamid for the illuminating discussions we had about scientific topics. To Ramin and Siavash, with whom I have built strong academic and personal relationships, I am grateful for all the wonderful moments we have shared. Finally, I would like to express my appreciation to Patrick. Although your time in our lab was short, your influence was lasting. Your initiation of acoustic work in our lab paved the way for me to delve into this topic.

To my beloved wife, *Hora* ;

and my beautiful daughter, *Leah* .

تا بدانجا رسید دانش من

که بدانم همی که نادانم

ابن سینا

“I gained knowledge up to the point
that I came to know how much I do not know.”

Ibn Sina (Avicenna) - (980-1037)

# Contents

# List of Figures

# List of Tables

# Nomenclature

**Abbreviations**

| | |
|---|---|
| CAA | Computational AeroAcoustics |
| CFD | Computational Fluid Dynamics |
| CFL | Courant-Friedrichs-Lewey |
| DG | Discontinuous Galerkin |
| DNS | Direct Numerical Simulation |
| ENO | Essentially Non-Oscillatory |
| ESDIRK | Explicit Singly Diagonally Implicit Runge-Kutta |
| FDM | Finite-Differene Method |
| FEM | Finite-Element Method |
| FR | Flux Reconstruction |
| FVM | Finite-Volume Method |
| FW-H | Ffowcs Williams and Hawkings |
| GA | Genetic Algorithm |
| GPS | Generalized Pattern Search |
| HORUS | High-ORder Unstructured Solver |
| IATA | International Air Transport Association |
| ILES | Implicit Large Eddy Simulation |
| LES | Large Eddy Simulation |
| MADS | Mesh Adaptive Direct Search |

| | |
|---|---|
| MAV | Micro Aerial Vehicle |
| MUSCL | Monotonic Upstream-Centered Schemes for Conservation Laws |
| NACA | National Advisory Committee for Aeronautics |
| PDE | Partial Differential Equation |
| P-ERK | Paired Explicit Runge-Kutta |
| PSD | Power Spectral Density |
| PSO | Particle Swarm Optimization |
| RANS | Reynolds-Averaged Navier-Stokes |
| RK | Runge-Kutta |
| SGS | Sub-Grid Scale |
| SIL | Sound Intensity Level |
| SPL | Sound Pressure Level |
| UAV | Unmanned Aerial Vehicles |
| WENO | Weighted Essentially Non-Oscillatory |
| WHO | World Health Organization |

**Symbols**

| | |
|---|---|
| $A$ | Amplitude |
| $C_D$ | Drag coefficient |
| $C_L$ | Lift coefficient |
| $C_p$ | Pressure coefficient |
| $c$ | Airfoil's chord length |
| $c_0$ | Speed of sound |
| $c^a_{max}$ | Maximum camber of the airfoil |
| $D$ | Depth of the cavity or diameter of the cylinder |
| $\mathbf{d}$ | Direction vector |
| $e$ | Total energy |

| | |
|---|---|
| $F$ | Force per unit width |
| $f$ | Flux function in the x-direction (in the context of CFD) |
| $f$ | Acoustic data surface |
| $g$ | Correction function |
| $H$ | Heaviside function |
| $h$ | Grid size |
| $\mathbf{I}$ | Identity matrix |
| $I$ | Sound intensity |
| $I_0$ | Reference intensity |
| $J$ | Jacobian matrix |
| $k$ | Grid point/volume/element |
| $L$ | Length of the cavity/cylinder |
| $L$ | Loading term (in the context of FW-H formulation) |
| $L_d$ | Linear dimension of computational domain |
| $L_z$ | Length of data surface duplication in the spanwise direction |
| $l$ | Largest integral length scale |
| $M$ | Mach number |
| $M$ | Mapping function (in the context of flux reconstruction) |
| $N_e$ | Total number of elements |
| $N_p$ | Total number of solution points |
| $n$ | Total number of design variables |
| $P$ | Frame of MADS optimization (in the context of optimization) |
| $P$ | Stability polynomial (in the context of temporal schemes) |
| $P$ | Compressive stress tensor (in the context of FW-H formulation) |
| $Pr$ | Prandtl number |
| $p$ | Static pressure |
| $p'_L$ | Loading acoustic pressure |

| | |
|---|---|
| $p'_Q$ | Quadrupole acoustic pressure |
| $p'_T$ | Thickness acoustic pressure |
| $Q$ | Thickness term (in the context of FW-H formulation) |
| $q$ | Heat flux |
| $R$ | Phase radii |
| $R_g$ | Gas constant |
| $R^\star$ | Amplitude radii |
| $Re$ | Reynolds number |
| $\mathbf{r}$ | Vector of distance between the source and the observer(s) (in the context of FW-H formulation) |
| $r$ | Ratio between the upstream and downstream cylinders' diameters |
| $St$ | Strouhal number |
| $s$ | Distance between the tandem cylinders |
| $T$ | Lighthill's stress tensor (in the context of FW-H formulation) |
| $T$ | Period |
| $t$ | Time |
| $t_c$ | Convective time |
| $t^a_{max}$ | Maximum thickness of the airfoil |
| $U_\infty$ | Free-stream velocity |
| $u$ | Conserved variable (in the context of flux reconstruction) |
| $v$ | Speed of data surface (in the context of FW-H formulation) |
| $W$ | Weighting function (in the context of flux reconstruction) |
| $W$ | Width of the cavity |
| $\mathbf{x}$ | Vector of source location (in the context of FW-H formulation) |
| $x_{c^a_{max}}$ | Location of the maximum camber of the airfoil |
| $\mathbf{y}$ | Vector of observer location (in the context of FW-H formulation) |
| $\mathcal{D}$ | Design space |
| $\mathcal{F}$ | Objective function |

$\mathcal{I}$ Interpolation operator

$\mathcal{M}$ MADS optimization mesh

$\mathcal{P}$ Solution polynomial degree

$\mathcal{R}$ Residual (semi-discrete space operator)

$\mathcal{S}$ Set of trial points

$\mathcal{X}$ Design variables

**Greek Letters**

$\alpha$ Angle of attack

$\alpha$ Characteristic wave speed (in the context of CFL number)

$\alpha$ Constant lifting coefficient (in the context of flux reconstruction)

$\Delta^m$ Mesh size parameter

$\Delta^p$ Poll size parameter

$\delta$ Boundary layer thickness

$\delta_{ij}$ Kronecker delta

$\ell$ Eddy size

$\eta$ Kolmogorov length scale (in the context of turbulence)

$\gamma$ Specific heat ratio

$\mu$ Dynamic viscosity

$\xi$ Standard reference space

$\rho$ Density

$\nu$ Kinematic viscosity

$\sigma$ Viscous stress tensor

$\tau$ Shear stress tensor

$\tau$ Source time (in the context of FW-H formulation)

$\vartheta$ Correction field

$\varphi_d$ Complex velocity potential for stationary dipole

$\varphi_m$ Complex velocity potential for stationary monopole

$\lambda$ Wavelength

$\Omega$ Computational domain

$\omega$ Angular velocity

**Superscripts**

$\square'$ Perturbed quantity

$\overline{\square}$ Time-averaged of a quantity

$\square^R$ Riemann flux

$\square^\delta$ Numerical approximation of a quantity

$\dot{\square}$ Temporal derivative

$\tilde{\square}$ Spatial derivative

**Subscripts**

$\square_C$ Continuous flux function

$\square_D$ Discontinuous flux function

$\square_i$ Component in the $x$-direction

$\square_i$ Solution point number in the $x$-direction (in the context of flux reconstruction)

$\square_{inv}$ Inviscid component

$\square_j$ Component in the $y$-direction

$\square_j$ Solution point number in the $y$-direction (in the context of flux reconstruction)

$\square_k$ Component in the $z$-direction

$\square_k$ Element number, where $k = 1, 2, ..., N_e$ (in the context of flux reconstruction)

$\square_k$ MADS optimization iteration number (in the context of optimization)

$\square_{obs}$ Observer quantities

$\square_{ref}$ Reference value

$\square_{rms}$ Root-mean-squared quantity

$\square_{vis}$ Viscous component

$\square_{\infty}$ Free-stream quantity

# Chapter 1

# Introduction

## 1.1 Motivation

Robert Koch, the Nobel Prize winner in physiology and medicine in 1905, anticipated in 1910 that "One day, man will have to fight noise as fiercely as cholera and pest." The World Health Organization (WHO) estimates that there is a loss of more than a million healthy life years in Western Europe annually due to noise-induced diseases [7]. The negative impacts of noise on the environment and human health have been studied thoroughly in the past decades [8, 9]. Environmental impacts include disruptions to wildlife behaviour and habitat [10], while human health impacts can range from hearing loss and sleep disturbance to increased stress levels and cardiovascular disease [9]. In the last two decades, global air passenger traffic demand has increased. In 2019, the annual number of air passengers was 4.5 billion [11]. The International Air Transport Association (IATA) predicts that total air transport could double, following the pre-pandemic trends, in the next two decades [12]. Hence, there is considerable debate about the environmental impacts of air travel, and the noise impacts of aviation must be considered and reduced accordingly.

## 1.2 Thesis Objectives and Contributions

This thesis is driven by the overarching goal of advancing the field of aeroacoustic design and optimization for aerospace vehicles through the development and application of innovative frameworks. The research is structured into four distinct parts to comprehensively address various aspects of aeroacoustic optimization and prediction.

In the first part, the focus is on near-field aeroacoustic shape optimization for two-dimensional flows. Leveraging the High-ORder Unstructured Solver (HORUS), this section showcases the efficacy of the developed framework in reducing near-field noise, particularly at low Reynolds numbers. The utilization of the Mesh Adaptive Direct Search (MADS) optimization algorithm facilitates efficient exploration of design spaces without the need for gradients, demonstrating its adaptability and robustness.

Building upon the success of the two-dimensional optimization, the second part extends the framework to three-dimensional turbulent flows using high-order Implicit Large Eddy Simulation (ILES). This advancement signifies a crucial step forward in accurately addressing the complexities of turbulent flows. By incorporating high-fidelity simulations, this allows for a more comprehensive exploration of aeroacoustic phenomena, contributing to the reduction of noise in turbulent flows.

The third part introduces an aeroacoustic solver based on the Ffowcs Williams and Hawkings (FWH) formulation, coupled with HORUS, enabling the prediction of noise at any far-field observer, contributing a crucial tool for assessing the acoustic impact of aerospace vehicles over varying distances.

The final part extends the optimization framework to address far-field noise concerns in three-dimensional turbulent flows. This stage, empowered by the HORUS solver, FWH solver, and MADS optimization algorithm, emphasizes the importance of holistic aeroacoustic shape optimization to meet the evolving demands of aerospace design.

These research endeavors collectively contribute to the imperative need for advanced aeroacoustic frameworks in the design and optimization of contemporary aerospace vehicles. The uti-

lization of a high-order flow solver like HORUS is instrumental in capturing intricate flow physics accurately, ensuring a more reliable representation of real-world scenarios. The FWH acoustic solver adds a vital predictive dimension, enabling a comprehensive assessment of noise impact over various distances. The adoption of the gradient-free MADS optimization algorithm aligns with the challenges posed by complex, multi-dimensional design spaces, offering a versatile and efficient optimization tool. The significance of reducing noise in aerospace vehicles, including air taxis, drones, and unmanned aerial vehicles, is underscored by its potential to meet stringent noise regulations, facilitate quiet take-off and landing, and enhance overall urban air mobility. These contributions collectively address critical challenges in the aerospace industry, advancing noise reduction strategies and paving the way for more sustainable and community-friendly aerial transportation solutions.

## 1.3 Thesis Outline

This thesis presents the governing equations and available numerical methods in Chapter 1. Chapter 2 presents methodology used in this study, providing a comprehensive overview of the approach employed. Then, near-field aeroacoustic shape optimization is investigated in two and three dimensions in Chapters 3 and 4, respectively. The implementation, verification, and validation of the far-field noise prediction framework are explained in Chapter 5, showcasing the robustness and accuracy of the developed framework. Furthermore, coupling of the optimization framework with the far-field noise prediction framework is investigated, exploring its potential for aeroacoustic shape optimization in the far-field. Finally, Chapter 6 concludes the thesis with a summary of the findings, recommendations for future work, and potential research applications.

## 1.4 Aviation History

Pioneering advancements in human flight began with the Montgolfier brothers in France, who introduced balloons in 1783 [1], shown in Figure 1.1. Subsequently, in the 1890s, Otto Lilienthal

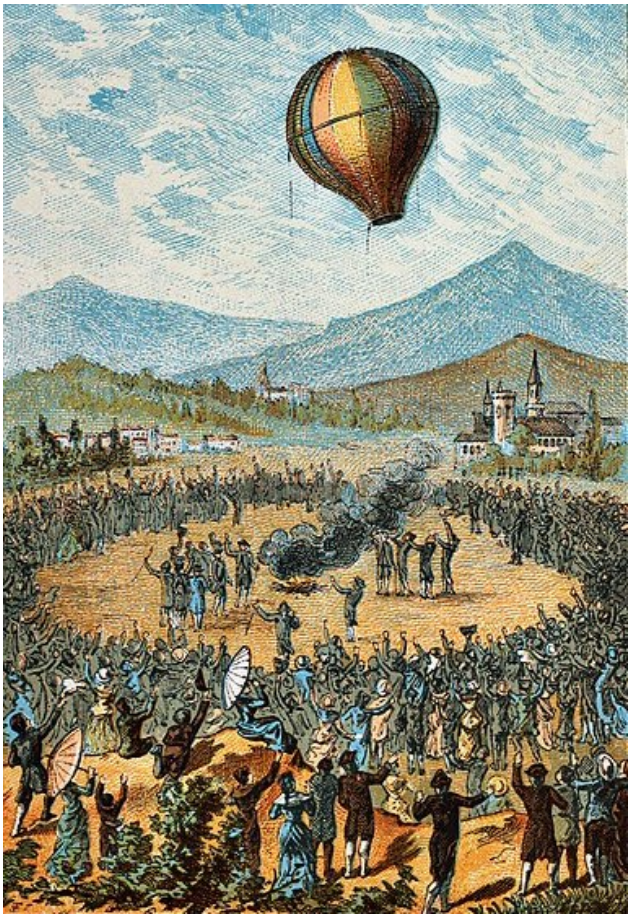

Figure 1.1. First public demonstration of Montgolfier brothers' balloon in Annonay, France [1].

made significant progress in glider technology, becoming the first person to construct and fly gliders successfully as shown in Figure 1.2. Building upon Lilienthal's achievements, the American brothers Wilbur and Orville Wright developed a fully functional biplane glider by 1902, capable of controlled flight. Expanding upon their innovations, the Wrights added a small engine and two propellers to another biplane, leading to the historical event of the world's first successful human-carrying engine-powered flight on December 17, 1903, at Kitty Hawk, North Carolina. Their aircraft, the Wright Flyer, is shown in Figure 1.3.

The aviation field has undergone significant transformations since the pioneering efforts of the Wright brothers in the early 20th century. The early aircraft designed by the Wright brothers were biplane gliders with wooden frames covered in fabric. The pilot's body movements controlled these aircraft, and their flights were relatively short in duration. Over the years, aircraft design has


Figure 1.2. Lilienthal glider [2].

Figure 1.3. Wrights' first powered airplane [3].

Figure 1.4. Messerschmitt Me 262 aircraft [4].

evolved significantly in terms of size, materials, aerodynamics, propulsion, and related technologies. A significant milestone in aviation history was the introduction of all-metal aircraft in the 1930s, which replaced the fabric-covered wooden frames of earlier designs. This shift to all-metal fuselage and wings improved aircraft's durability, strength, and performance.

The advent of World War II brought about further advancements in aviation technology. Jet engines were introduced, allowing for higher speeds and greater efficiency than piston-engined propeller aircraft. The first operational jet-powered aircraft, the Messerschmitt Me 262, shown in Figure 1.4, was developed by Germany during the war, followed by other countries such as the United Kingdom, the United States, and the Soviet Union. After World War II, the commercial aviation industry experienced rapid growth with the introduction of jet airliners. In the 1950s, aircraft manufacturers such as Boeing and Airbus emerged as significant players in the aviation industry, developing innovative and advanced aircraft designs. Boeing introduced the Boeing 707 capable of carrying passengers at higher speeds and over longer distances. Airbus, a European consortium of aircraft manufacturers, was formed in the 1970s and introduced the Airbus A300, shown in Figure 1.5, which featured advanced aerodynamics, materials, and avionics.

Since then, aircraft designs have continued to evolve with advancements in technology and en-


Figure 1.5. Airbus A300 aircraft [5].

gineering. Modern commercial aircraft feature advanced composite materials, sophisticated aerodynamic designs, fly-by-wire systems, and cutting-edge avionics. As a result, these aircraft can fly at higher speeds, longer distances, and with improved fuel efficiency, comfort, and safety features. Recently, there has been a growing emphasis on environmental sustainability in aircraft design [13, 14, 15, 16]. For example, manufacturers are exploring alternative propulsion systems, such as electric and hybrid-electric engines, to reduce greenhouse gas emissions and noise pollution. Additionally, there is ongoing research in areas such as supersonic and hypersonic flight, autonomous aircraft, and electric and hybrid aircraft, which may shape the future of aviation.

As we delve into the rich history of aviation, it becomes evident that aircraft design has always been in a constant state of evolution. Traditionally, aircraft optimization relied on analytical analysis and physical model testing, which is expensive and not economically viable. However, with the advent of computer technology, computational methods have become indispensable for optimizing aircraft design. While such technologies have led to significant advancements in the aerodynamic design of aircraft, there is still ongoing work to be done in the realm of aeroacoustic design.

## 1.5 Aeroacoustics

Aviation noise has become a significant concern for both operators and regulators due to the increasing evidence of adverse health impacts, continuous community complaints, and the availability of cost-effective programs to reduce exposure to aircraft noise. More stringent international policies have also added to this pressure [17].

The concerns related to aircraft noise encompass community annoyance, sleep disturbance, health impacts, and potential effects on children's learning, with studies indicating associations between aircraft noise and elevated blood pressure and stress hormone levels in children, though conclusive evidence is lacking and other factors may contribute [9].

The imperative of addressing aviation noise concerns has given rise to aeroacoustic shape optimization. By developing robust and reliable optimization frameworks, it becomes feasible to minimize the aviation noise. These optimization frameworks play a pivotal role in not only meeting regulatory requirements but also in proactively reducing community annoyance and potential health impacts associated with aviation noise. As the industry increasingly emphasizes sustainable practices, the integration of aeroacoustic shape optimization emerges as a crucial strategy for achieving quieter and more community-friendly aviation operations. The acoustic terminology used in this study is briefly explained in the following section.

### 1.5.1 Acoustic Terminology

In this section, we explore some essential acoustic terminology, namely, acoustic waves, acoustic intensity, and sound pressure level. Understanding these concepts is of utmost importance for comprehending aeroacoustics and, in particular, the contents of this thesis.

#### 1.5.1.1 Acoustic Waves

Acoustic waves are mechanical waves that propagate through a medium, such as air, resulting from the periodic compression and rarefaction of the medium [18]. They can be generated by a vibrating source, such as a musical instrument or vocal cords, and are perceived as sound by the

human ear. Acoustic waves have various applications in fields like communication, music, and medical imaging. Furthermore, aeroacoustic waves are typically generated by the interaction of a fluid flow with solid objects, typically in the context of aerodynamics. When a fluid, such as air, flows over or around solid objects, such as an aircraft wing or a car body, it can create complex flow patterns that generate sound waves. These aeroacoustic waves are often characterized by their frequency, amplitude, and directionality and can have significant implications for noise control, environmental impact, and vehicle design. When a fluid flow becomes turbulent, it undergoes rapid changes in velocity and pressure, which can generate aeroacoustic waves as the flow interacts with solid objects or turbulent structures decay. Turbulent flows can be a significant source of aeroacoustic waves, especially in high-speed flows or flow around complex geometries. Understanding and predicting the generation of aeroacoustic waves from turbulent flows is an important area of research in computational aeroacoustics.

#### 1.5.1.2 Acoustic Measurements

Measuring noise is critical in understanding its characteristics and evaluating its impact. Noise is typically measured using specialized instruments called sound level meters or noise dosimeters. These instruments measure the sound pressure level, which is the magnitude of the pressure fluctuations caused by the sound waves, and are expressed in units of decibels (dB). Sound level measurements can quantify the intensity or loudness of noise and determine its frequency, content, and duration.

Frequency, amplitude, pitch, and decibel are essential parameters that describe noise characteristics. Frequency refers to the number of cycles or oscillations of a sound wave per unit of time and is measured in Hertz (Hz). It determines the perceived pitch of the sound, with higher frequencies corresponding to higher pitches and lower frequencies corresponding to lower pitches. On the other hand, the amplitude is the magnitude or strength of the sound wave and is typically measured as the maximum pressure fluctuation or displacement of the medium caused by the sound wave. It determines the perceived volume or loudness of the sound, with larger amplitudes corresponding

| SPL ($dB$) | Source (distance from source) | Human Perception |
|---|---|---|
| 180+ | Rocket launch ($50m$) | |
| 160 – 168 | Shotgun blast ($< 1m$) | Hearing loss |
| 146 – 162 | Firecracker ($3m$) | |
| 135 – 140 | Air raid siren ($30m$) | |
| 115 – 130 | Live rock concert ($5m$) | Threshold of pain |
| 112 – 125 | Snowmobile ($< 1m$) | |
| 109 – 120 | Jack hammer ($< 1m$) | |
| $\approx 110$ | Boeing 707 before landing ($1800m$) | Very loud |
| 93 – 114 | Subway train ($5m$) | |
| 98 – 112 | Hand-hell drill ($< 1m$) | |
| $\approx 90$ | Boeing 787 before landing | Loud |
| 82 – 100 | Heavy traffic ($5m$) | |
| 72 – 93 | Restaurant ($< 1m$) | |
| 71 – 91 | Electric mixer ($< 1m$) | Quiet |
| 45 – 70 | Joby eVTOL ($< 500m$) | |
| 0 | Human threshold of hearing | |

Table 1.1. Sound pressure level scale of human hearing, adopted from [6]

to louder sounds. Finally, the pitch is a subjective perception of the frequency of a sound and can vary depending on the individual's hearing sensitivity and perception. Decibel is a logarithmic unit that expresses the ratio of one sound intensity or pressure level to another. It is commonly used to represent the noise magnitude, with higher decibel values corresponding to louder sounds. Decibels provide a convenient way to compare and quantify different noise levels and assess their potential impact on human health and the environment. Table 1.1 illustrates the typical range of the decibel scale and presents many acoustic sources along with their corresponding perceived levels to the human ear.

Acoustic intensity is a fundamental physical quantity used to quantify the power carried by sound waves per unit area in a direction perpendicular to that area. The sound intensity unit is measured in watts per square meter, $W/m^2$. It is important to note that sound intensity and pressure are not the same physical quantities, although they are related. A Sound Intensity Level (SIL) is a unit of measurement that quantifies sound intensity in decibels, $dB$, relative to a reference intensity level. Although SIL is related to sound intensity, it is not directly proportional. The SIL is measured on a logarithmic scale, while sound intensity is measured on a linear scale. However,

the relationship between the two can be described mathematically using the following equation

$$\text{SIL} = 10\log_{10}\left(\frac{I}{I_0}\right), \tag{1.1}$$

where $I$ is the sound intensity, and $I_0$ is the reference intensity, usually $10^{-12}W/m^2$. Therefore, the SIL increases as the sound intensity increases, but not at a constant rate. While sound intensity measures the amount of power carried by sound waves, human hearing is sensitive to sound pressure, the physical quantity used to measure the loudness of sound humans can hear. The Sound Pressure Level (SPL) can be obtained using the following equation

$$\text{SPL} = 20\log_{10}\left(\frac{p'_{rms}}{p_{ref}}\right), \tag{1.2}$$

where $p_{ref} = 20\mu Pa$ is the reference pressure, and $p'_{rms}$ is the root-mean-squared of the pressure perturbation, $p'$, which is calculated by subtracting the time-averaged pressure, $\overline{p}$, from the instantaneous pressure, $p$, i.e. $p' = p - \overline{p}$.

In general, there are various noise measurements commonly used in sound analysis. Apart from IPL and SPL, one can consider the steady equivalent continuous sound level over a specified period, typically measured in decibels $dB$ and known as equivalent continuous sound level (Leq). It provides a single value that summarizes the overall sound level over a duration, often used to assess average noise exposure. Furthermore, the overall sound pressure level (OASPL) calculates the total sound pressure level over a designated time period; perceived noise level (PENL) accounts for human perception of noise by weighting sound levels based on psychoacoustic factors to better represent the perceived loudness of different frequencies; and A-weighted equivalent sound level (LAeq) calculates the equivalent continuous sound level with A-weighting applied attenuating low and high frequencies to better match human hearing sensitivity.

## 1.6 Governing Equations

The governing equations of fluid flow are a set of Partial Differential Equations (PDEs) for conservation of mass, momentum, and energy. Solving these equations is essential to understanding and predicting fluid flow in various applications, from aircraft design to weather forecasting. Despite their fundamental importance, these equations are notoriously difficult to solve analytically, and require advanced analytical and computational techniques to obtain accurate approximations. The conservation of mass, momentum, and energy equations are explained in this chapter, along with the ideal gas law as the closure equation of state. Then, the unsteady compressible Navier-Stokes equations are given in their compact form.

### 1.6.1 Reynolds Transport Theorem

There are two different approaches in analysing fluid flows, the Lagrangian approach and the Eulerian approach. In the Lagrangian approach, individual fluid particles are tracked as they move through space and time. Each fluid particle is labelled and its position, velocity, and other properties are described as functions of time. The Lagrangian approach focuses on following the motion of individual particles. Physical laws, such as Newton's laws and conservation principles, are directly applied to each particle. The Lagrangian approach is well-suited for analyzing a small number of particles, but it becomes impractical for complex flow fields with a large number of particles. In the Eulerian approach, a control volume is defined in the flow field, and fluid flow properties of interest are expressed as fields within this control volume. Individual fluid particles are not identified or tracked; instead, the focus is on specific locations in space as time passes. Properties like pressure, velocity, acceleration, and other flow variables are described as functions of space and time within the control volume. Eulerian methods are better suited for studying complex fluid dynamics with a high particle count. Physical laws, including Newton's laws and conservation principles, need to be translated or reformulated for use with the Eulerian description.

The Reynolds transport theorem [19] provides a mathematical framework for the transformation from the Lagrangian to the Eulerian description. It allows us to relate the time rate of change of

an extensive property within a system to the rate of change of that property within a control volume, as well as the net flow of the property across the control surface. By applying the Reynolds transport theorem, we can establish a relationship between the Lagrangian and Eulerian approaches, enabling us to use the conservation laws in the Eulerian framework of Computational Fluid Dynamics (CFD).

### 1.6.2 Conservation of Mass

Conservation of mass states that the total mass of a fluid in a closed system remains constant over time. This principle is essential in CFD as it provides a fundamental equation that must be satisfied for any simulation to be physically meaningful. The PDE form of conservation of mass equation is

$$\frac{\partial \rho}{\partial t} + \frac{\partial}{\partial x_i}(\rho u_i) = 0, \tag{1.3}$$

where $\rho$ is the density, $t$ is time, $u_i$ are the components of the velocity vector, and $x_i$ are the components of the coordinate system. This equation ensures that the mass of the fluid remains constant within the system being simulated and provides a mathematical constraint that must be satisfied by any numerical simulation of fluid flow.

### 1.6.3 Conservation of Momentum

Momentum is a physical quantity defined as the product of an object's mass and velocity. Conservation of momentum is a fundamental principle in physics that states that the total amount of momentum within a closed system remains constant. This principle implies that momentum cannot be created or destroyed but can only be transferred or transformed from one object to another within the system. Additionally, conservation of momentum applies independently in all Cartesian directions, which can present challenges in predicting the behaviour of complex fluid systems, particularly in the presence of forces acting in multiple directions. The conservation of

momentum equation is expressed as

$$\frac{\partial}{\partial t}(\rho u_i) + \frac{\partial}{\partial x_j}(\rho u_i u_j) = -\frac{\partial p}{\partial x_i} + \frac{\partial}{\partial x_j}(\tau_{ij}), \tag{1.4}$$

where $p$ is the pressure, and $\tau_{ij}$ is the shear stress tensor. The first term on the left-hand side of the equation represents the rate of change of momentum with respect to time, while the second term represents the convective acceleration of momentum. The right-hand side of the equation represents the forces acting on the fluid, including pressure and viscous forces. The shear stress tensor, $\tau_{ij}$, represents the viscous forces acting on the fluid and is a function of the fluid's velocity gradients. The shear stress tensor has nine components representing the stresses in the three-dimensional space. In general, the shear stress tensor is a function of the viscosity of the fluid and the velocity gradients. It plays a critical role in predicting fluid flow behaviour, particularly in the boundary layer regions of the fluid where the velocity gradients are high. The shear stress tensor is defined as

$$\tau_{ij} = \mu\left(\frac{\partial u_i}{\partial x_j} + \frac{\partial u_j}{\partial x_i} - \frac{2}{3}\frac{\partial u_k}{\partial x_k}\delta_{ij}\right), \tag{1.5}$$

where $\delta_{ij}$ is the Kronecker delta, and $\mu$ is the dynamic viscosity.

### 1.6.4 Conservation of Energy

Conservation of energy states that energy in an isolated system cannot be created or destroyed but can be converted from one form to another. This equation represents the rate of change of the total energy of a fluid system with respect to time and space and is written in differential form as

$$\frac{\partial}{\partial t}(\rho e) + \frac{\partial}{\partial x_j}(\rho u_j e) = -\frac{\partial}{\partial x_j}(p u_j) + \frac{\partial}{\partial x_j}(\tau_{ij} u_i) - \frac{\partial q_j}{\partial x_j}, \tag{1.6}$$

where $e$ is the total energy, and $q_j$ is the heat flux. On the left-hand side, the first term represents the time rate of change of the total energy of the fluid system, and the second term represents the convective transport of energy by the fluid. The terms on the right-hand side represent the work

done on the fluid by pressure and viscous forces, respectively, and the heat transfer rate due to thermal conduction and radiation. The heat flux is defined as

$$q_j = -\frac{\mu}{Pr}\frac{\partial}{\partial x_j}\left(e + \frac{p}{\rho} - \frac{1}{2}u_k u_k\right), \tag{1.7}$$

where $Pr$ is the Prandtl number.

### 1.6.5 Ideal Gas Law

The ideal gas law is a fundamental equation of state for an ideal gas. In CFD simulations, the ideal gas law can be used to close the governing equations of motion, which describe the behaviour of the fluid. To close the equations, we need to relate the pressure and energy of the fluid by assuming that the fluid is an ideal gas. The pressure and density of the fluid are related to the total energy through the following equation

$$p = (\gamma - 1)\rho\left(e - \frac{1}{2}u_k u_k\right). \tag{1.8}$$

Closure using the ideal gas law allows us to write the equations of motion in terms of the fluid's density, velocity, and energy and to solve them numerically using computational methods.

### 1.6.6 Navier-Stokes Equations

The Navier-Stokes equations describe the motion of viscous fluid in a given domain and provide a fundamental basis for understanding fluid mechanics. The equations are a set of PDEs consisting of a time-dependent conservation of mass equation, three time-dependent conservation of momentum equations, and a time-dependent conservation of energy equation. The primitive variables in the problem are pressure, density, velocity, and temperature. The independent variables are the spatial coordinates of the domain and the time. The compressible unsteady Navier-Stokes

equations can be cast in the following general form

$$\frac{\partial \boldsymbol{u}}{\partial t} + \boldsymbol{\nabla} \cdot \boldsymbol{F} = 0, \tag{1.9}$$

where $\boldsymbol{u}$ is the vector of conserved variables

$$\boldsymbol{u} = \begin{bmatrix} \rho \\ \rho u_i \\ \rho e \end{bmatrix}, \tag{1.10}$$

and the inviscid and viscous Navier-Stokes fluxes are

$$\boldsymbol{f}_{inv,j}(\boldsymbol{u}) = \begin{bmatrix} \rho u_j \\ \rho u_i u_j + \delta_{ij} p \\ u_j(\rho e + p) \end{bmatrix}, \tag{1.11}$$

and

$$\boldsymbol{f}_{vis,j}(\boldsymbol{u}, \nabla \boldsymbol{u}) = \begin{bmatrix} 0 \\ \tau_{ij} \\ -q_j - u_i \tau_{ij} \end{bmatrix}, \tag{1.12}$$

respectively.

The Navier-Stokes equations are difficult to solve analytically, leading to the use of numerical methods. The challenges in solving these equations arise from their partial differential form and non-linearity of the modelled flow phenomena. Therefore, numerical methods are necessary to obtain approximated solutions to these equations, which are critical for predicting and optimizing the behaviour of fluids in various applications.

## 1.7 Numerical Methods

The development of numerical techniques and algorithms for solving PDEs using CFD has revolutionized the field of fluid dynamics. CFD has enabled many essential applications in the aerospace industry, including the prediction of noise and acoustics. Computational AeroAcoustic (CAA) is a relatively new field that combines numerical methods, fluid mechanics, and acoustics to model and predict noise sources and propagation in complex flows. CFD plays a crucial role in CAA by providing accurate and efficient solutions to the governing equations of fluid dynamics and acoustics. The ability to predict and control aviation noise is critical for reducing the environmental impacts of aviation and improving the safety and comfort of air travel [7]. Therefore, developing advanced CFD techniques for noise prediction is paramount to the aerospace industry [20].

To mitigate the impact of aviation noise, it is necessary to employ optimization techniques that can be integrated with CFD and CAA frameworks. Different optimization approaches, such as gradient-based and gradient-free methods, can be considered. In addition, these techniques can help in identifying optimal designs and operational conditions. Integrating optimization techniques with CFD and CAA provides a comprehensive framework for predicting and mitigating noise, contributing to advancements in noise reduction technology and improving the overall acoustic performance of aircraft.

This section is structured into three parts. First, we discuss turbulent flow and predictive methods. Next, we briefly touch upon CFD and CAA techniques. Lastly, we explore various optimization techniques and explain the gradient-free MADS optimization algorithm.

### 1.7.1 Turbulence

Turbulence is complex flow behaviour that arises in various practical applications. Chaotic fluctuations in velocity, pressure, and other flow properties characterize turbulence. Due to their prevalence in real-world scenarios, precisely predicting turbulent flows is very important. Mathematical models can be used to predict the evolution of turbulent flows thanks to the development of digital computers.

An important parameter in predicting the onset of turbulence is the Reynolds number, $Re$, which is the ratio of inertial forces to viscous forces in a fluid. It is a dimensionless number comprised of the physical characteristics of the flow. An increasing Reynolds number indicates an increasing turbulence of flow. In the context of turbulent flows, the Reynolds number is used to predict the critical velocity at which the flow transitions from laminar to turbulent.

One of the fundamental concepts in turbulence is the energy cascade, which describes energy transfer between different scales of motion. In a turbulent flow, large-scale eddies break down into smaller eddies. This process continues, with energy being transferred from larger to smaller scales until it reaches the smallest scales of turbulence known as the Kolmogorov length scale, $\eta$, where kinetic energy is dissipated into heat through viscous dissipation [21]. Turbulent flows are characterized by a wide range of scales that can vary over several orders of magnitude, and each scale contributes to the overall behaviour of the turbulent flow. The larger scales of turbulence are typically associated with the energy-containing or energy-producing range, while the smaller scales are associated with the energy-dissipating or energy-consuming range.

To simulate and predict turbulent flows, various approaches are developed. The most accurate one is the Direct Numerical Simulation (DNS), where all turbulence scales are resolved. However, DNS is computationally expensive for most practical engineering problems. Alternatively, turbulence modelling approaches can be used to predict turbulent flows. These models aim to capture turbulence's complex and multiscale nature by providing approximations or closures for the unresolved turbulent scales. Commonly used turbulence models are Large Eddy Simulation (LES) and Reynolds-Averaged Navier-Stokes (RANS) approach. Each model offers different accuracy and computational efficiency levels based on the turbulence scales that they model or resolve. Figure 1.6 shows the energy cascade of turbulence and the scales that are either resolved or modelled within each approach. In the following sections, each of these approaches is briefly discussed.

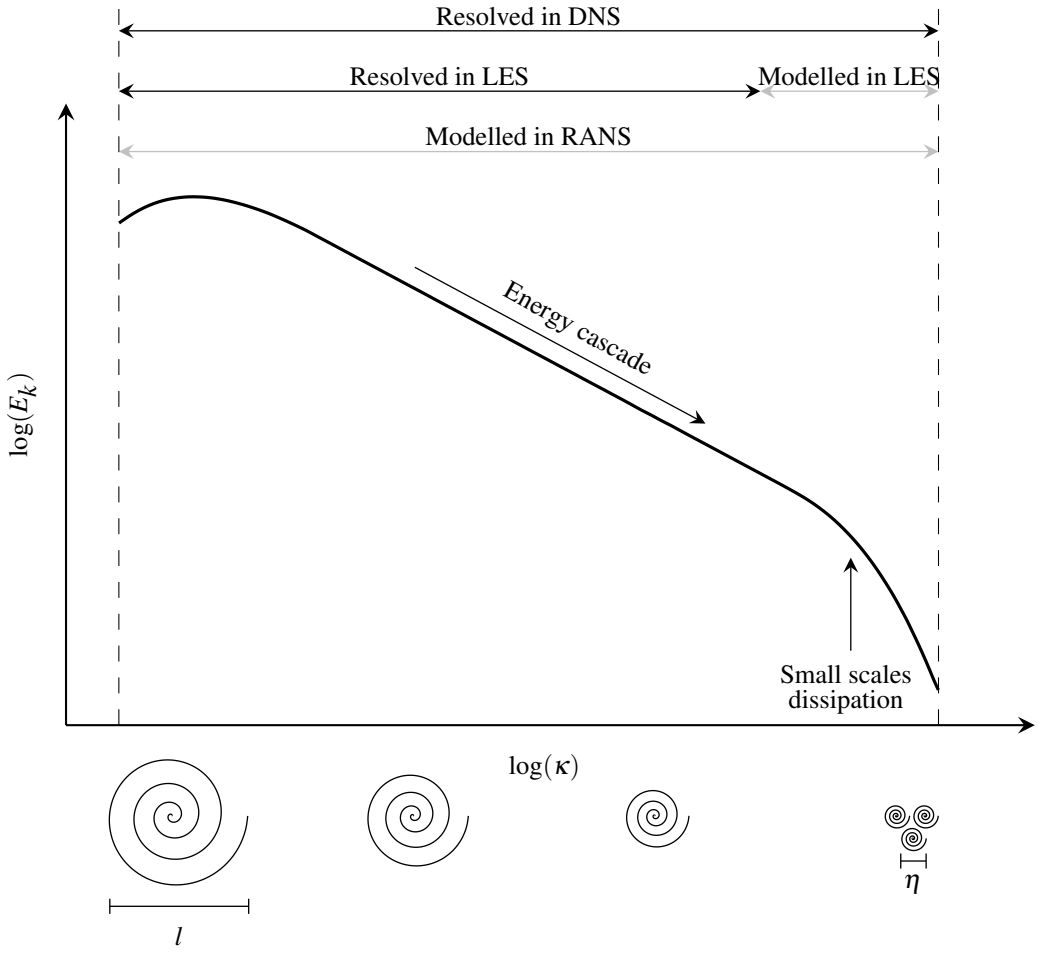


Figure 1.6. Energy cascade in turbulence and the resolved/modelled regions in different turbulence modelling approaches.

#### 1.7.1.1 Direct Numerical Simulation

In DNS, the Navier-Stokes equations are solved numerically without any turbulence model, resulting in the direct computation of all scales of motion in the flow, from the largest to the smallest. This means that DNS provides a highly accurate and detailed prediction of the entire flow field, including the complex interactions between the large and small eddies that characterize turbulent flows. The resolution of the numerical grid used in DNS must be fine enough to accurately resolve the smallest turbulent structures in the flow, spanning a wide range of scales. In order to solve all of the scales from the largest integral length scale, $l$, to the smallest Kolmogorov length scale, $\eta$, the grid spacing size, $\Delta x$, must be proportional to $\eta$. So, the minimum grid-spacing size required for DNS scales like [21]

$$\Delta x \sim \eta \sim l\, Re^{-\frac{3}{4}}. \tag{1.13}$$

For any three-dimensional domain, $L_d$ being the linear dimension of the computational domain, the minimum number of sampling points required for DNS will scale like [21]

$$N \sim \left(\frac{L_d}{\Delta x}\right)^3 \sim \left(\frac{L_d}{l}\right)^3 Re^{\frac{9}{4}}. \tag{1.14}$$

This shows that a vast number of grid points is required for DNS to simulate high Reynolds number regimes, making it prohibitively expensive to most flows of interest for engineers, like the flow over an aircraft where the Reynolds number is typically in the order of millions.

One of the main advantages of DNS is its ability to provide highly accurate predictions of turbulent flows, as it directly resolves all the scales of motion without any turbulence modelling assumptions. DNS is beneficial for studying fundamental turbulence phenomena, such as the energy cascade and the dynamics of vortical structures, and validating and calibrating turbulence models used in other approaches, such as LES and RANS. However, the computational cost of DNS makes simulating industrial scale problems unattainable with today's computational power. As a result, DNS is typically limited to relatively low Reynolds numbers, where the smallest scales of motion are still computationally manageable.

#### 1.7.1.2 Large Eddy Simulation

In LES, the large eddies responsible for most of the energy transfer and transport in turbulent flows are directly resolved, while the small-scale structures are modelled typically using Sub-Grid Scale (SGS) models. In LES, the numerical grid used is coarser than that used in DNS, as the small-scale structures are modelled rather than resolved. The filtered or resolved equations, obtained by applying a spatial filter to the governing equations, are then solved iteratively in time to obtain the time evolution of the large-scale flow field. Finally, the unresolved, small-scale structures are modelled using SGS models, typically based on the local flow properties and the resolved large-scale structures. These models aim to capture the effects of small-scale structures on large scales, such as energy transfer and SGS turbulence production. Various SGS models, such as the Smagorinsky model [22], the dynamic Smagorinsky model [23], and the scale similarity models [24], can be used in LES, depending on the flow characteristics and the desired level of accuracy.

One of the main advantages of LES over DNS is its lower computational cost, as it uses a coarser grid. Therefore, for equivalent cost, LES is capable of predicting turbulent flows at higher Reynolds numbers, making it more suitable for practical engineering applications. LES can also provide insights into the dynamics and physics of turbulent flows, such as the behaviour of large-scale structures and their interactions, which are essential for understanding and predicting complex flows in real-world scenarios. LES is a widely used approach for predicting the evolution of turbulent flows, striking a balance between accuracy and computational cost. However, the accuracy of LES predictions depends on the quality of the SGS models used [25], which are still an active area of research and may only sometimes accurately capture the small-scale turbulence dynamics [26]. LES is also limited by the spatial and temporal resolutions of the numerical grid, which can affect the accuracy of the predicted flow field.

#### 1.7.1.3 Implicit Large Eddy Simulation

Implicit large eddy simulation is a recent approach that facilitates LES without an explicit SGS model [27]. The key idea in ILES is to use an inherently dissipative numerical discretization, such

as a high-order upwinded approach. These schemes introduce numerical dissipation at the small scales of the flow, effectively dampening the small-scale turbulence without the need for explicit SGS models. As a result, the small-scale structures are implicitly modelled by the numerical dissipation of the discretization, while the large-scale structures are directly resolved.

One of the main advantages of ILES over LES is its ability to accurately capture small-scale turbulence without explicit SGS models, which can be challenging to model accurately in LES. ILES also avoids some of the limitations of DNS, such as the high computational cost associated with resolving all scales of turbulence. Additionally, ILES can handle complex geometries and unstructured grids, making it applicable to a wide range of practical engineering problems. However, ILES also has some limitations. For example, the accuracy of ILES predictions depends on the accuracy of the numerical discretization scheme used, and not all numerical schemes are suitable for ILES [27]. Furthermore, the dissipation level introduced by the numerical scheme must be carefully controlled to ensure accurate modelling of small-scale structures [28]. Additionally, ILES may still require some form of modelling or treatment for near-wall turbulence, as the small-scale structures in the near-wall region are particularly challenging to capture accurately [29].

#### 1.7.1.4 Reynolds-Averaged Navier-Stokes Approach

RANS is a widely used technique that employs statistical averaging to predict the behaviour of turbulent flows. In RANS, the governing equations are averaged over time to obtain time-averaged quantities. This averaging process allows for the simulation of turbulent flows at reduced computational cost compared to approaches like DNS, LES, and ILES. Furthermore, it eliminates the need to resolve all the turbulent scales in time and space. One of the key requirements of RANS is the use of turbulence models to account for the unresolved time-dependent terms on the time-averaged flow variables. These models are based on statistical assumptions and empirical correlations and provide additional closure equations that are solved along with the Navier-Stokes equations to account for the unresolved turbulent scales.

One of the main advantages of RANS is computational efficiency. It does not require the

explicit resolution of turbulent scales, making it suitable for various engineering applications with complex geometries. RANS also provides insights into the statistical behaviour of turbulence, as it predicts time-averaged quantities that are often of interest in engineering analysis and design. One of the main limitations of RANS is its reliance on turbulence models, which introduce additional assumptions and uncertainties into the simulations. The accuracy of RANS predictions depends on the accuracy of the turbulence model used, and different models may perform differently for different flow configurations [30]. RANS also struggles to accurately capture highly transient and unsteady flows, as the time-averaging process may smooth out important transient features [30]. Additionally, RANS may not accurately capture some complex physics associated with turbulence, such as turbulent mixing and coherent structures [31]. These effects are inherently transient and difficult to capture using time-averaging.

#### 1.7.1.5 Comparison

DNS, LES, and ILES are known as scale-resolving techniques. Despite providing fairly accurate results, the computational cost of these techniques is more expensive than RANS. DNS is the most accurate method; however, it needs a large number of degrees of freedom to resolve all of the eddy sizes. In DNS, the most expensive part of the computation is the intermediate to small-scale eddies. Since energy cascades from the larger eddies down to the smaller ones, the large-scale eddies might not be heavily influenced by the small-scale eddies [21]. So, one can think of LES instead of DNS, where those small-scale eddies can remain unresolved and modelled, whereas the largest scales to the intermediate ones are solved accurately. In LES, the effect of unresolved small-scale eddies on the turbulent flow is modelled using SGS models. However, ILES relies on truncation error to act as the SGS model.

As stated by the National Aeronautics and Space Administration (NASA), scale-resolving techniques are expected to enable unprecedented insight into the aerodynamic design process, enabling superior designs at reduced cost and risk [20]. The ability of current RANS-based CFD methods is limited to problems that require an extensive experience base and are unreliable for turbulent-

separated flows. RANS approaches poorly model turbulent-separated flows, so scale-resolving techniques are of industrial interest due to their capability in these regimes.

In aeroacoustics, the sound is generated from unsteady flow features. Thus, steady RANS techniques are not suitable, and unsteady RANS techniques are usually insufficient to model unsteady turbulent behaviour of the flow due to the inherent unsteadiness of noise-generating sources [32]. Scale-resolving techniques are considered attractive alternatives; however, the affordability of such techniques is an open question. LES is a promising approach for noise prediction at Reynolds number of practical engineering interest [33]. The accuracy of LES is affected by the dissipation of the discretization techniques. The turbulent eddies and their associated sound spectra can be damped artificially due to numerical dissipation, especially in the high-frequency ranges [32]. LES using different SGS models is compared to unsteady RANS results, showing its appropriateness [34]. The ILES technique, which has no explicit SGS model, saves significant computational cost [35]. ILES has been used for sound computation by other researchers demonstrating promising results [36, 37, 38].

### 1.7.2 Computational Fluid Dynamics

The modern history of fluid dynamics dates back to the seventeenth century when pure experimental approaches were established. In the eighteenth and nineteenth centuries, improvements in theoretical fluid dynamics led researchers to combine experimental and theoretical approaches in the twentieth century. The advent of powerful computers and numerical algorithms revolutionalized this area of science. Hence, a third approach, CFD, appeared [39].

CFD is a branch of fluid dynamics that utilizes digital computers and applied mathematics to produce cost-effective quantitative predictions of real fluid flow phenomena based on approximate numerical solutions of fluid motion conservation laws. CFD has developed quickly during the past several decades, which has led to improved simulations of aerodynamic flows. Implementing advanced CFD techniques to design aircraft reduces ground-based and in-flight tests, wind tunnel time for an aircraft development program, and the cost and risk of optimizing designs. As a

physics-based simulation technology, CFD improves our understanding and insight into critical physical phenomena. Designing and analyzing engineering systems often requires experimental tests that are impractical due to model complexity or wind tunnel limitations, giving rise to the inevitable need for CFD. Thus, developing CFD techniques is necessary to make such studies feasible and reduce the cost and risk of designing such systems.

The utility of CFD also arises due to the lack of a general analytical solution to the governing equations. The first step in solving PDEs using CFD is discretization, which is transferring the continuous PDE system into a discrete approximation of that PDE to solve it numerically. The approximate numerical solution of any PDE gives answers only at a set of discrete points in the domain, known as grid points. In contrast, the analytical solution gives a continuous solution that varies continuously throughout the domain. Different methods are available to discretize a PDE temporally and spatially, and a few of them are explained here.

#### 1.7.2.1 High-Order Methods

High-order CFD techniques have garnered significant interest due to their potential to achieve a higher levels of accuracy and efficiency in simulating fluid flows. One of the key advantages of high-order CFD techniques is their ability to capture complex flow features and resolve fine details in the solution.

The adoption of high-order methods in industrial applications poses notable challenges. For instance, the formulation and implementation of high-order methods require careful consideration and robust algorithms. These techniques are inherently more complex than traditional lower-order methods, and the design of stable and accurate numerical schemes can be challenging. Ensuring that high-order methods maintain stability and do not introduce spurious oscillations is a crucial concern in practice. Various techniques are available to ensure the stability of high-order simulations, such as modal filtering [40, 41] and anti-aliasing [42, 43, 44], amongst others. Additionally, transitioning from conventional lower-order CFD methods to high-order methods often requires re-engineering existing simulation workflows and software infrastructure. This adaptation process

can be resource-intensive and may deter some industrial applications from making the switch.

High-order methods, while more complex, can achieve comparable accuracy to low-order methods on a coarser mesh, potentially making them more computationally cost-effective [45]. Furthermore, various techniques have been introduced to lower the computational cost of high-order methods, including polynomial adaptation [46, 47, 48], mesh adaptation [49, 50, 51], and hybridized and embedded FR approaches [52]. Moreover, adaptive time-stepping [53] can be combined with novel temporal schemes to accelerate simulations, such as Paired Explicit Runge-Kutta (P-ERK) [54], Embedded P-ERK [55], and optimal explicit RK schemes [56].

In the realm of acoustic studies, the choice to transition to higher-order CFD methods becomes particularly compelling. This is due to the fact that the accuracy of noise prediction is intimately linked to the accuracy of the underlying flow solver. High-order CFD methods, with their capacity to capture intricate flow features and resolve fine details, offer a significant advantage in improving the precision of the flow solver. This enhanced accuracy not only contributes to more reliable predictions of the flow field but also has a direct impact on the quality of noise predictions. The benefits of high-order CFD techniques in acoustic studies extends beyond merely improving accuracy. They can lead to more insightful analyses of noise sources and propagation, which is crucial for understanding and mitigating noise-related issues.

#### 1.7.2.2 Spatial Discretization Methods

Common techniques for spatial discretization include Finite-Difference Method (FDM), Finite-Volume Method (FVM), and Finite-Element Method (FEM). Each method has strengths and limitations and may be better suited to specific problems or applications.

The simplest and historically oldest method for spatial discretization of PDEs is the FDM. In FDM, the solution is approximated at regularly arranged discrete points, illustrated in Figure 1.7. Operator discretization via the FD approach is often straightforward, leading to efficient schemes. Additionally, the explicit semi-discrete form allows for flexibility in selecting appropriate time stepping methods. Moreover, these methods can be extended to higher-order approximations

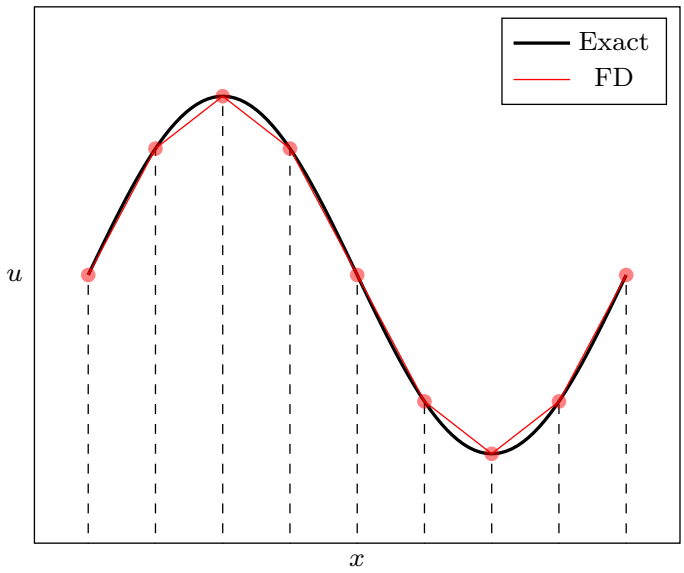


Figure 1.7. Finite-difference method.

with relative ease. However, a limitation of the method is its reliance on a local one-dimensional polynomial approximation via a Taylor series expansion, which enforces a simple dimension-by-dimension structure in higher dimensions [40], making the native FDM ill-suited for complex geometries. One way to address this limitation is by using curvilinear grids in combination with the FD approach. By transforming the grid from Cartesian to curvilinear coordinates, the FD method can be applied on these grids, providing a more suitable framework for solving problems with somewhat complex geometries [57, 58, 59]. Nevertheless, it remains challenging to apply the FD method to high-geometric complexity.

To achieve greater geometric flexibility, an element-based discretization is introduced, i.e. the FV method. Hence, the computational domain, $\Omega$, is represented by a collection of non-overlapping elements, $\Omega_k$, and a volume average approximates the solution on each volume, in its simplest form, as depicted in Figure 1.8. Typically, these elements are arranged in an unstructured manner to fully cover the physical domain. To increase the order of accuracy of the method,

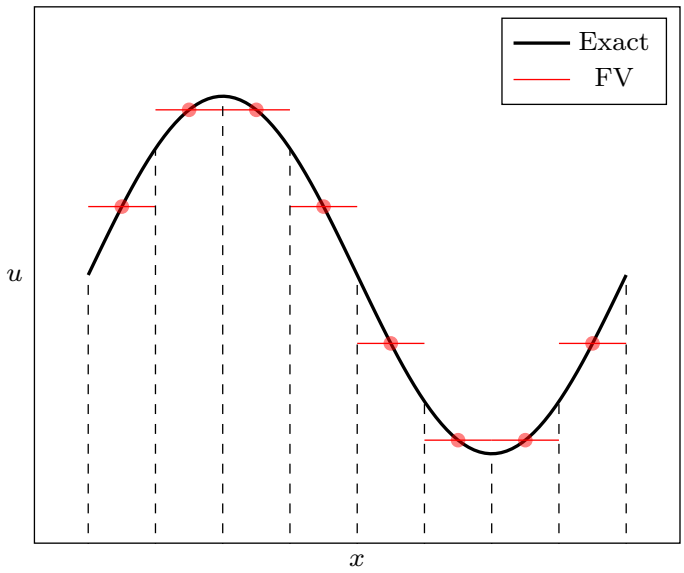


Figure 1.8. Finite-volume method.

information from the neighbouring elements is required. This is achievable for the simple one-dimensional case, similar to the FDM. However, in the case of higher dimensions, a particular grid structure is required. However, other FV techniques have been developed to eliminate particular grid structure requirement, namely, Essentially Non-Oscillatory (ENO) [60], Weighted ENO (WENO) [61], Monotonic Upstream-Centered Schemes for Conservation Laws (MUSCL) [62], amongst others. FV methods are widely used in industry; however, it is challenging to extend them to high-order and these methods are generally limited by memory bandwidth making them ill-suited for modern hardware architectures [63].

To simplify extension to higher orders, more degrees of freedom can be introduced within each volume by adding a set of solution points to the volumes and edges between them. This method is known as the FEM, which splits the computational domain into a number of discrete elements. FEM typically uses continuous basis functions within each element, and the elements are connected in a globally continuous manner. Thus, the solution is approximated as a continu-

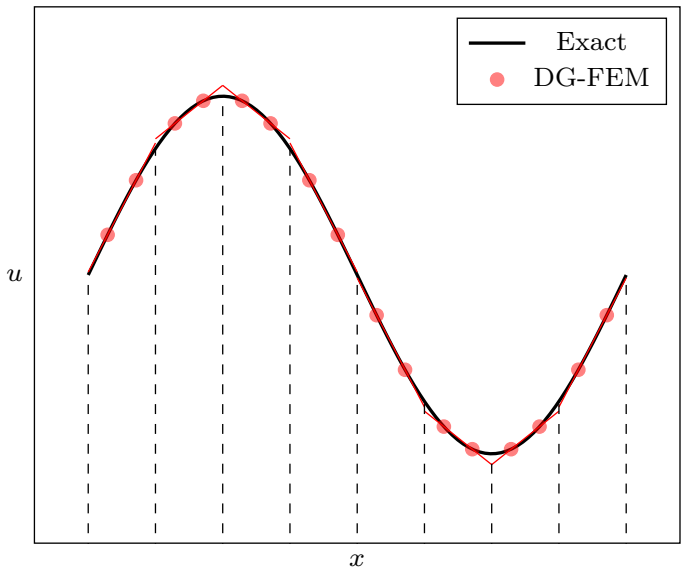


Figure 1.9. Discontinuous Galerkin finite-element method for $\mathcal{P}1$ discretization.

ous function over the entire domain, and continuity is maintained across element boundaries. The solution is approximated locally within each element using a set of basis functions. An intelligent combination of FVM and FEM leads to the Discontinuous Galerkin FEM (DG-FEM), which is well-suited for high-order accuracy in the vicinity of complex geometries [40]. In the DG-FEM method, the solution is approximated using piecewise polynomials of a desired degree within each element, allowing for discontinuities at the element interfaces. These discontinuities are handled through the use of numerical fluxes that explicitly account for the jumps in the solution at element interfaces. The solution and flux are approximated numerically within each element by a polynomial of degree $\mathcal{P} = N_p - 1$, where $N_p$ is the total number of solution points within each element as depicted in Figure 1.9. A space of test functions is defined, $\mathcal{V}^\delta$, and the residual is required to be orthogonal to all test functions in this space. In the DG-FEM, the test functions are the nodal basis functions [40].

Finally, Huynh [64] introduced a new high-order accurate approach capable of recovering some

existing schemes, such as DG, and formulating new ones. This approach is known as Flux Reconstruction (FR). The accuracy, generality, and robustness of the FR method, along with its suitability for modern hardware, have made it appealing to solve problems that benefit from complex geometries and high-order accuracy [65]. Moreover, FR can provide more accurate solutions in less computational time than other standard low-order numerical methods [45]. Mills [6] investigated the applicability of the FR approach for direct CAA revealing significant promise in its potential utilization.

### 1.7.3 Computational Aeroacoustics

CAA is a specialized field of CFD that focuses on the simulation and prediction of sound generated by aerodynamic flows. It involves the numerical modelling and simulation of fluid flow and its interaction with solid structures, considering the generation, propagation, and radiation of sound waves. The methodologies used in CAA range from semi-empirical schemes [66, 67, 68] to high-fidelity unsteady flow simulations [69, 70]. Semi-empirical schemes estimate the noise sources using mean-flow and turbulence statistics, while high-fidelity simulations resolve the sound generation process by directly applying the fundamental conservation principles. The sound can be computed in a limited region close to the sources, known as the near-field sound. However, the study of sound far from these sources, known as the far-field sound, is of primary interest to the aviation industry.

In recent years, advancements in computational power and numerical methods have greatly enhanced the capabilities of CAA. For example, high-fidelity simulations, such as LES and DNS, have allowed for more accurate and detailed predictions of aerodynamic noise [71, 72, 73]. These simulations resolve the turbulent structures and flow fluctuations contributing to noise generation, providing valuable insights into the underlying physics of sound propagation. On the other hand, simplified models like RANS are commonly used for quick and practical noise predictions [74, 75]. However, they may have limitations in capturing the full acoustic spectrum of noise generation [76].

#### 1.7.3.1 Direct Approach in CAA

In general, there are two approaches to noise prediction. The first, being the most accurate and computationally expensive, is the direct approach. In this approach, the sound field is computed together with the unsteady turbulent flow field using CFD techniques, which means that the sound is predicted at any point by computing the acoustic pressure directly from the CFD results at that point. Thus, the observer must be inside the computational domain, and the accuracy of the sound prediction relies on the accuracy of CFD results. This approach is the most accurate numerical noise prediction technique but is challenging. One of the main challenges of the direct approach is the scale separation between the flow field and the sound-field. In an unconfined region, the time-scale of a sound wave matches that of its fluid dynamic source [32]. However, the length-scale of a sound wave is related to its fluid dynamic source by the fluctuating Mach number as $\lambda = \ell/M$, $\lambda$ being the wavelength and $\ell$ the eddy size [32]. Thus, a large length-scale separation exists in low-fluctuating-Mach-number flows, requiring extremely small time steps on numerics due to the acoustic Courant-Friedrichs-Lewey (CFL) number. The primary shortcoming of the direct approach is that by increasing the distance of the observer position, the computational domain has to be larger, which increases the computational cost of the simulation. Therefore, even if the current growth level in supercomputers' speed remains the same in the forthcoming years, this method remains prohibitively expensive for general CAA problems in the aviation industry.

#### 1.7.3.2 Hybrid Approaches in CAA

The second approach, being more computationally efficient for far-field CAA, is the hybrid approach. Different methods or models are combined to efficiently and accurately predict sound generation, propagation, and radiation from aerodynamic flows. In hybrid approaches, high-frequency sound waves, known as near-field noise, are typically generated by turbulent flow structures and require high-resolution numerical methods to capture their details accurately. On the other hand, low-frequency sound waves, known as far-field noise or sound radiation, are generated by large-scale flow features. Notably, in the far-field, the flow is quasi-linear with minimal turbulence and

small pressure perturbation. Acoustic waves can be propagated using a linear acoustic analogy, allowing for the use of simpler and computationally inexpensive models like Kirchhoff's or the Ffowcs Williams and Hawkings (FW-H) equation [77] to predict far-field noise. The hybrid approach may involve using a high-fidelity numerical method, such as LES or DNS, to capture the near-field noise while using a more straightforward and computationally inexpensive model to predict the far-field noise.

The second approach, being more computationally efficient for far-field CAA, is the hybrid approach. Different methods or models are combined to efficiently and accurately predict sound generation, propagation, and radiation from aerodynamic flows. In hybrid approaches, high-frequency sound waves, known as near-field noise, are typically generated by turbulent flow structures and require high-resolution numerical methods to capture their details accurately. On the other hand, low-frequency sound waves, known as far-field noise or sound radiation, are generated by large-scale flow features and can be predicted using simpler models or methods. The hybrid approach may involve using a high-fidelity numerical method, such as LES or DNS, to capture the near-field noise while using a more straightforward and computationally inexpensive model, such as Kirchhoff's or Ffowcs Williams and Hawkings (FW-H) equation [77], to predict the far-field noise. Furthermore, in hybrid approaches, it is assumed that the non-linear near-field affects the propagation of the generated sound waves; however, the sound waves have no significant effect on the fluid flow field. Since this assumption is only valid for low fluctuating Mach number flows, applying hybrid approaches is restricted to such flows [32], as this approach assumes a one-way coupling of the flow field and sound field.

The hybrid approach in CAA allows for a trade-off between accuracy and computational cost. It is a practical approach for predicting aerodynamic sound in real-world engineering applications where accuracy and efficiency are important considerations. Lighthill's analogy [78], also known as Lighthill's theory, is a pioneering concept in CAA that relates the generation of sound by aerodynamic flows to the motion of fluid particles. It was first introduced by Sir James Lighthill in the 1950s [78] and has since served as a fundamental framework for understanding and predicting

aerodynamic sound.

#### 1.7.3.3 Lighthill's Acoustic Analogy

Lighthill's theory [78] estimates the sound radiated from a fluctuating fluid flow into free space and is based on the equations of motion. In Lighthill's theory, conservation of mass is maintained as in Equation 1.3; however, conservation of momentum is re-written as

$$\frac{\partial}{\partial t}(\rho u_i) + c_0^2 \frac{\partial \rho}{\partial x_i} = -\frac{\partial T_{ij}}{\partial x_j}, \tag{1.15}$$

where $c_0$ is the speed of sound, and $T_{ij}$ is the Lighthill's stress tensor defined as

$$T_{ij} = \rho u_i u_j + \Big[(p - p_0) - c_0^2 (\rho - \rho_0)\Big] \delta_{ij} - \sigma_{ij}, \tag{1.16}$$

where $\delta_{ij}$ is the Kronecker's delta and $\sigma_{ij}$ is viscous stress tensor. Finally, the wave equation is defined as

$$\frac{\partial^2 \rho}{\partial t^2} - c_0^2 \nabla^2 \rho = \frac{\partial^2 T_{i,j}}{\partial x_i \partial x_j}, \tag{1.17}$$

that describes the propagation of acoustic waves in the fluid, which are responsible for generating sound. It relates the pressure fluctuations in the fluid to the rate of change of velocity fluctuations and governs the behaviour of sound waves in the fluid medium. Equations 1.3, 1.15, and 1.17 are the basic equations of the theory of aerodynamic sound production that provides a framework for understanding and predicting the generation of sound by aerodynamic flows [78].

Lighthill estimates the acoustic power output of a fluid's motion [79], based on the exact equations of motion of a gas, for a subsonic flow condition. Curle [80] extended the Lighthill analogy to include the influence of the presence of solid and stationary surfaces on the sound generated aerodynamically. Ffowcs Williams and Hawkings have extended the Lighthill-Curle theory to include the surfaces in arbitrary convective motion [77]. The FW-H equation is considered analytically superior for aeroacoustics as it is founded on the principles of conservation in fluid mechanics, as opposed to being based on the wave equation. This formulation is used in conjunction with

unsteady RANS [34, 81], LES [34, 82, 83, 84, 85, 86], ILES [38, 87, 88], and DNS [89, 90]. The FW-H formulation is thoroughly explained in Chapter 5.

The numerical methods to solve the flow field and predict the noise emitted by an object. The goal of this study is to minimize the noise via shape optimization. Thus, in the next section, we explore some available optimization techniques.

### 1.7.4 Optimization

In optimization problems, engineers are interested in minimizing/maximizing a function via modifying a set of parameters, referred to as an objective function and design parameters, respectively. An optimization problem aims to find the design variables that minimize or maximize the objective function, $\mathcal{F}$. The objective function represents a performance metric of interest, such as aerodynamic efficiency or sound pressure level. The design variables, $\boldsymbol{X}$, are the unknown parameters of the system being optimized, such as the points parametrizing the shape of an airfoil. An optimization problem can have constraints, defining bounds on the feasible design space and limiting the range of acceptable values for the design variables. These bounds can be used to model physical, geometrical, or other limitations when finding the optimal solution. Constraints are typically defined as equalities or inequalities that must be satisfied by the design variables. The initial guess, $\boldsymbol{X_0}$, provides a starting point for the optimization algorithm to search for the optimal solution. The quality of the initial guess can significantly impact the convergence and efficiency of the optimization process. The optimization problem is terminated when specified criteria are met. This can include conditions such as a maximum number of iterations, a minimum change in the objective function, or the satisfaction of certain constraints.

Leveraging the use of optimization techniques to design quieter aircraft is an open question. There is limited research on aeroacoustics optimization to reduce the far-field noise. For instance, the aerodynamically generated noise, emitted by a two-dimensional NACA 0012 airfoil, has been optimized using a discrete-adjoint Newton-Krylov algorithm and FW-H formulation [91]. An optimization method based on artificial neural networks has also been introduced to minimize

noise by Tao and Sun [92]. The far-field noise emitted by a rod-airfoil is minimized using an algorithmic-differentiation-based discrete adjoint solver for optimization and unsteady RANS and FW-H formulation via a hybrid approach [93]. In general, there are two optimizer categories, gradient-based and gradient-free techniques, explained in the following sections.

#### 1.7.4.1 Gradient-Based Optimization

Gradient-based optimization methods are a class of optimization algorithms that use gradient information to improve the design towards an optimum design point iteratively. The gradient of the objective function is used to determine the direction of the steepest descent or ascent, and the algorithm adjusts the variables accordingly [94]. These gradients can be computed using the finite-difference method in the simplest form or complex-step methods if round-off error is a concern [95]. Either approach's computational cost is expensive and proportional to the square of the number of design variables [96]. The adjoint approach, on the other hand, provides a more computationally efficient alternative with a computational cost being almost independent of the number of design variables [97]. The adjoint approach to optimization in fluid dynamics was first introduced by Pironneau [98], and it gained popularity in aerodynamic optimization with the work of Jameson [97]. There are currently two adjoint formulations in use: the continuous approach [99], where the adjoint equations are derived from the governing PDEs and then discretized, and the discrete approach [100, 101, 102], where the discretized governing equations are differentiated to obtain the adjoint equations.

The main benefit of a gradient-based approach is its rapid convergence, which can significantly accelerate the optimization process compared to methods that do not utilize gradients. Furthermore, gradient-based methods offer a clear convergence criterion, as a reduction in the magnitude of the gradient by multiple orders of magnitude indicates attainment of a local optimum.

A drawback of gradient-based methods utilizing adjoints is the development cost, as linearization can be time-consuming whether done manually or using automatic differentiation [103]. Additionally, gradient-based methods may struggle with challenges such as noisy objective function

spaces, inaccurate gradients, categorical variables, and topology optimization [96]. Furthermore, these methods are often limited to finding local optima rather than global optima.

Furthermore, gradient-based optimization via the adjoint method in aerodynamics is usually performed using RANS [104, 105, 106], which has notable limitations, specifically when turbulent transition and flow separation are present. Moreover, conventional adjoint-based optimization techniques diverge for scale-resolving simulations in high Reynolds numbers due to the chaotic nature of the Navier-Stokes equations [107]. Hence, the use of gradient-based optimization methods may not be appropriate for aeroacoustic problems due to the unsteady nature of sound generation and propagation, which necessitates scale-resolving techniques for precise noise prediction.

#### 1.7.4.2 Gradient-Free Optimization

Gradient-free optimization techniques, such as Genetic Algorithms (GA) [108, 109], Particle Swarm Optimization (PSO) [110, 111, 112], and MADS [113, 114], are valuable tools in CFD for solving complex optimization problems where gradient information may not be available or costly to compute. These methods do not rely on gradients but explore the search space through objective function evaluations. Gradient-free optimization techniques benefit CFD applications with noisy, non-convex, or discrete-variable objective functions. They can be effective in aeroacoustic problems where sound generation and propagation are complex. These techniques offer flexibility and robustness in handling diverse optimization challenges, contributing to advancements in CFD and enabling efficient optimization in engineering applications.

#### 1.7.4.3 Mesh Adaptive Direct Search

In this study, the MADS optimization technique is used, which falls between the Generalized Pattern Search (GPS) [115] and the Coope and Price frame-based methods [116]. Unlike GPS, MADS allows for a more flexible design space exploration during the optimization process, making it a more effective solution for unconstrained and linearly constrained optimization [113]. A significant advantage of MADS over GPS is the flexible local exploration, known as poll directions, rather than a fixed set of directions. Two parameters are defined in the context of the MADS

optimization: the mesh size parameter, $\Delta^m$, and the poll size parameter, $\Delta^p$. The mesh size parameter determines the granularity and resolution of the mesh of the design space on which the optimization algorithm operates. A higher resolution leads to a more precise search, while a lower resolution allows for a broader search and a higher chance of finding the global optimal solution. The poll size determines the size of the neighbourhood around the incumbent point where new trial points are chosen. The number of trial points in each design cycle can be $n + 1$, the minimal positive basis, or $2n$, the maximal positive basis [113], where $n$ is the number of design variables.

In the gradient-free MADS optimization procedure, there are two sequential steps in each design iteration: the search and poll steps. The optimization procedure begins with the search step and the initial design point, $\boldsymbol{X}_0 = [X_0^1, X_0^2, ..., X_0^n]$. A finite number of pseudo-random trial points are defined, and infeasible ones are discarded. Infeasible trial points are points within the design space that do not satisfy the constraints of the optimization problem. The trial points are generated based on the current mesh and the direction vectors, $\mathbf{d}_j \in \mathcal{D}$ (for $j = 1, 2, ..., n$), where $\mathcal{D}$ is the design space. $\mathcal{D}$ must be a positive spanning set [117], and each direction, $\mathbf{d}_j$, must be the product of some fixed non-singular generating matrix by an integer vector [113]. The mesh at iteration $k$ is defined as [113]

$$\mathcal{M}_k = \bigcup_{X \in \mathcal{S}_k} \{X + \Delta_k^m \mathcal{D} z : z \in \mathbb{N}^{n_\mathcal{D}}\}, \tag{1.18}$$

where $\mathcal{S}_k$ is the set of trial points at which the objective function is evaluated in iteration $k$. The mesh $\mathcal{M}_k$ is constructed from a finite set of $n_\mathcal{D}$ directions, $\mathcal{D} \subset \mathbb{R}^n$, scaled by a mesh size parameter $\Delta_k^m \in \mathbb{R}_+$. The objective function is evaluated at these trial points. The current iteration stops after the objective function at all trial points is computed or when a lower objective function is found. Then, the next iteration starts with a new incumbent solution $\boldsymbol{X}_{k+1} \in \Omega$ with the objective function of $\mathcal{F}(\boldsymbol{X}_{k+1}) < \mathcal{F}(\boldsymbol{X}_k)$, and a mesh size parameter $\Delta_{k+1}^m \geq \Delta_k^m$. At any iteration, the maximum value of the mesh size parameter is set to one, $\Delta_{max}^m = 1$. Note that the design space of each design variable is scaled to one, and a mesh size parameter of one can cover the entire design space.

On the other hand, if the search step fails to find a new optimum, the poll step is invoked before terminating the current optimization iteration. In the poll step, the mesh size parameter is reduced

to define a new set of trial points closer to the incumbent design variables. The key difference between GPS and MADS is the new poll size parameter, $\Delta_k^p \in \mathbb{R}_+$, that controls the magnitude of distance between the trial points generated by the poll step to the incumbent point. This new set of trial points defined in the poll step is called a frame. The MADS frame at iteration $k$ is defined to be [113]

$$P_k = \{X_k + \Delta_k^m d : d \in \mathcal{D}_k\} \subset \mathcal{M}_k, \tag{1.19}$$

where $\mathcal{D}_k$ is a positive spanning set. In each MADS iteration, the mesh and poll size parameters are defined. The mesh size parameter of the new iteration is defined as [113]

$$\Delta_{k+1}^m = \begin{cases} \frac{1}{4}\Delta_k^m & \text{if the poll step fails to find an improved design point,} \\ 4\Delta_k^m & \text{if an improved design point is found, and if } \Delta_k^m \leq \frac{1}{4}, \\ \Delta_k^m & \text{otherwise.} \end{cases} \tag{1.20}$$

These rules ensure $\Delta_k^m$ is always a power of 4 and never exceeds 1. The poll size parameter is also defined as [113]

$$\Delta_{k+1}^p = \begin{cases} n\sqrt{\Delta_k^m} & \text{if the minimal positive basis construction is used,} \\ \sqrt{\Delta_k^m} & \text{if the maximal positive basis construction is used.} \end{cases} \tag{1.21}$$

Figure 1.10 depicts the search and poll steps for a scaled design space with two design variables. In this example, the minimal positive basis construction results in three trial points per MADS iteration. The incumbent design point is $\boldsymbol{X}_k$, and the trial points, $p_k^1$, $p_k^2$ and $p_k^3$ are chosen in the specified frame defined via the poll size parameter. The objective function is computed at these trial points, and we assume the $p_k^3$ trial point is the new incumbent design point. Then, the search is successful, and the mesh size parameter reduces by a factor of 4. If a new incumbent design point is not found, the search step is unsuccessful, and the poll step is invoked, as depicted in Figure 1.10b. In the poll step, the mesh size parameter is quadrupled, and the objective function is

evaluated at a new set of trial points. Finally, when a new incumbent objective function is found in a design iteration, the optimization may converge or continue depending on the stopping criterion. The optimization problem is terminated when the stopping criteria are met.

Abramson et al. [114] introduced a new way of choosing directions for the MADS class of algorithms, in which the polling directions are orthogonal to each other. In this method, known as OrthoMADS [114], the trial points are not defined pseudo-random, ensuring that the results of a given optimization problem is repeatable. To elucidate the distinctions between the MADS and OrthoMADS algorithms, Figure 1.11 depicts the search and poll steps of the OrthoMADS optimization technique for iteration $k$, employing a maximal positive basis construction. In Figure 1.11a, we assumed that $p_k^3$ is the new incumbent design.

To the author's knowledge, there is minimal literature on optimization in conjunction with high-fidelity flow simulations. The trailing-edge shape is optimized to reduce the noise of a hydrofoil using large eddy simulation [118]. Moreover, LES is used to train the artificial neural network for optimizing gas cyclones [119, 120]. Furthermore, Karbasian [121] explored the utility of MADS algorithm for high-fidelity aerodynamics optimization for low Reynolds number flow over an SD7003 airfoil.

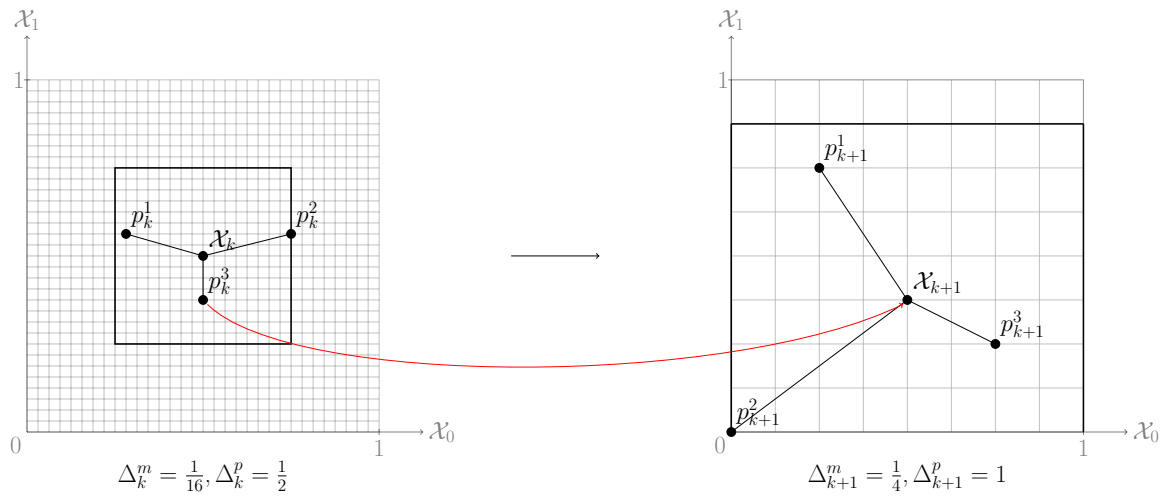


(a) Search step.

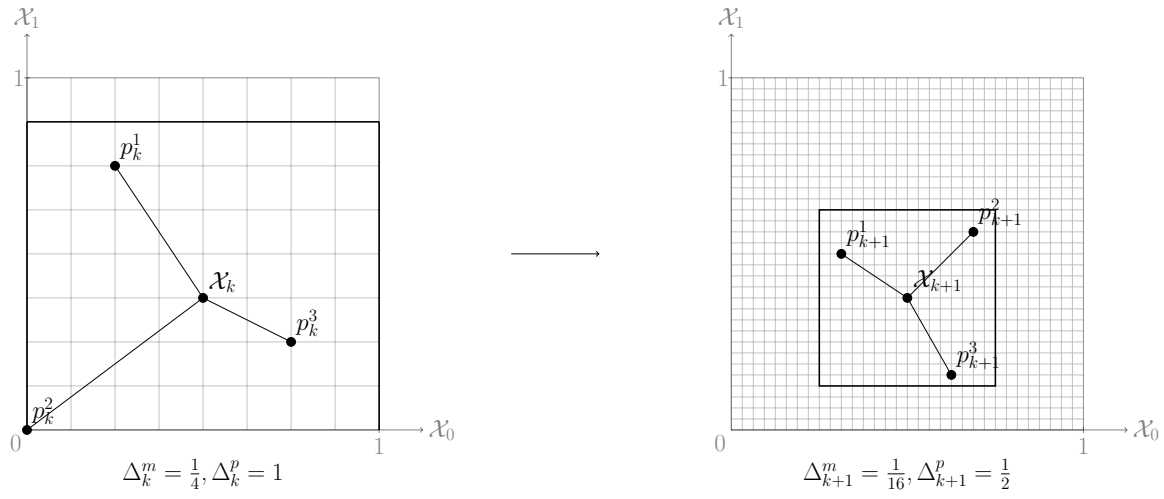


(b) Poll step.

Figure 1.10. Search and poll steps of the MADS optimization techniques for iteration $k$, using maximal positive basis construction.

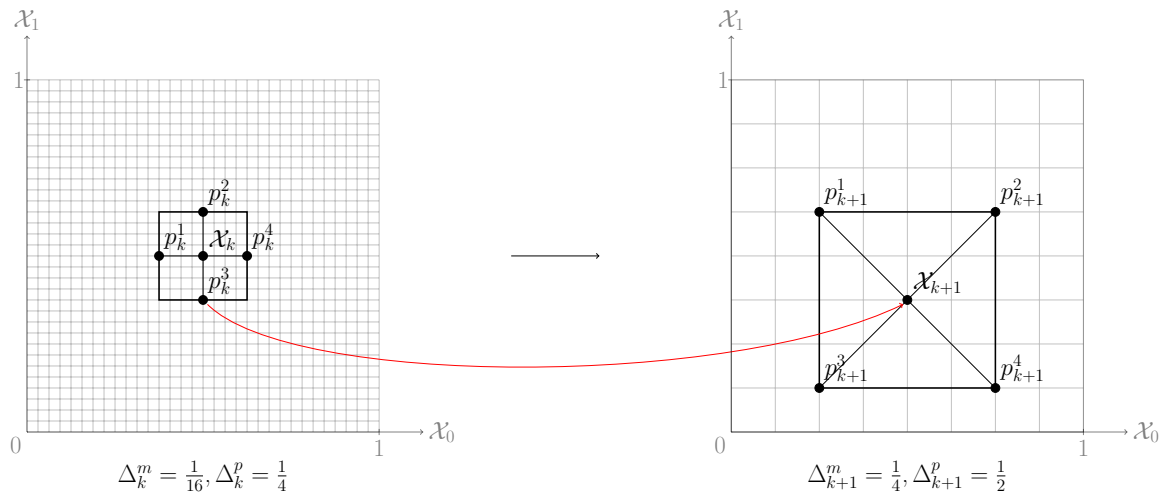


(a) Search step.

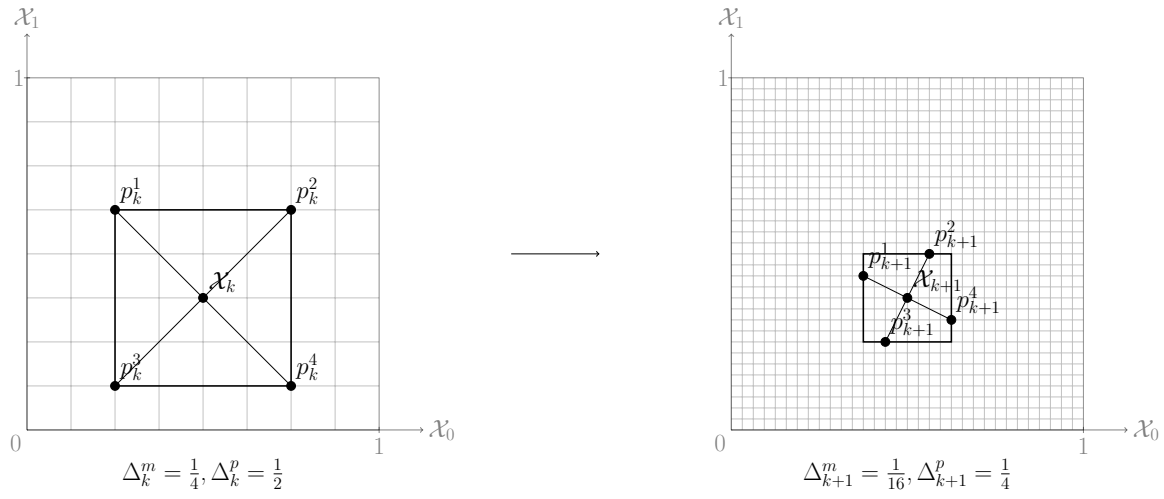


(b) Poll step.

Figure 1.11. Search and poll steps of the OrthoMADS optimization techniques for iteration $k$, using maximal positive basis construction.

# Chapter 2

# Methodology

## 2.1 Introduction

This chapter discusses temporal and spatial discretization techniques in CFD, different CAA approaches for predicting noise, and different optimization techniques. The advantages and disadvantages of each method is discussed to provide a comprehensive understanding of the numerical methods used in this study.

## 2.2 Temporal Discretization Methods

Temporal discretization involves numerically integrating the governing equations forward in time, which is necessary for modelling time-varying flows. Temporal discretization techniques can be classified into explicit and implicit methods. Explicit methods use a forward time differencing formula, and the numerical solution at the current time step is calculated using information only from previous time steps. Implicit methods, on the other hand, use a backward time difference formula, and the numerical solution at the current time step is calculated by solving a system of algebraic equations that includes information from both the future and previous time steps. Implicit methods can permit a larger stable time step size than explicit methods, making them more suitable for solving stiff problems [54]. However, implicit methods require the solution of an extensive

system of non-linear equations at each time step, which can be computationally expensive. The choice of temporal discretization depends on several factors, including the desired accuracy, stability, and computational cost. Despite the success of implicit schemes in CAA applications, explicit schemes are also commonly used [33, 122]. In CAA simulations, a wide range of length scales must be resolved, requiring high grid resolutions, which can result in increased computational costs and memory consumption for implicit methods [33]. Moreover, high-frequency damping in implicit methods sacrifices accuracy for stability [123]. These can cancel out the benefits of larger time step sizes.

The Runge-Kutta (RK) family of schemes is widely used due to their simplicity of implementation. They also extend to higher orders of temporal accuracy without significantly increasing computational cost [56]. However, the disadvantage of explicit time stepping methods is that the maximum allowable time step size is strictly limited by the CFL number defined as

$$CFL = \frac{\alpha \Delta t}{\Delta x}, \tag{2.1}$$

where $\alpha$ is a characteristics wave speed, $\Delta t$ is the time step size, and $\Delta x$ is the grid spacing.

The general form of a conservation law after spatial discretization can be re-written as a system of differential equations

$$\frac{d\boldsymbol{u}}{dt} = \mathcal{R}(\boldsymbol{u}), \tag{2.2}$$

where $\mathcal{R}(\boldsymbol{u})$ is the semi-discrete space operator. Thus, the left-hand-side temporal term must be discretized. A general Runge-Kutta method $\mathrm{RK}_{s,e,p}$ having $s$-stages, of order $p$, and requiring $e$ derivative evaluations, are typically described using a Butcher tableau [124] which has a general compact form of

$$\begin{array}{c|c} \boldsymbol{c} & \boldsymbol{A} \\ \hline & \boldsymbol{b} \end{array} \tag{2.3}$$

that can be expanded as

$$\begin{array}{c|cccc} c_1 & a_{1,1} & a_{1,2} & \cdots & a_{1,s} \\ c_2 & a_{2,1} & a_{2,2} & \cdots & a_{2,s} \\ \vdots & \vdots & \vdots & \ddots & \vdots \\ c_s & a_{s,1} & a_{s,2} & \cdots & a_{s,s} \\ \hline & b_1 & b_2 & \cdots & b_s \end{array} \tag{2.4}$$

where $\boldsymbol{A}$ is the RK matrix, $b_i$ is a weight coefficient with

$$\sum_{i=1}^{s} b_i = 1, \tag{2.5}$$

and $c_i$ contains the intermediate node locations of the intermediate stages, represented as a fraction of the total time step and

$$c_i = \sum_{j=1}^{s} a_{i,j}. \tag{2.6}$$

Then, the solution is approximated at $s$ intermediate stages

$$\boldsymbol{u}^{t+1} = \boldsymbol{u}^t + \Delta t \sum_{i=0}^{s} a_{i,j} \mathcal{R}^i, \tag{2.7}$$

where $\boldsymbol{u}^{t+1}$ is the unknown solution at the next time step, $\boldsymbol{u}^t$ is the known solution at the current time step, and $\mathcal{R}^i$ is the residual at each intermediate stage. If the matrix $A$ is strictly lower-triangle, it is an explicit scheme; otherwise, it is implicit. The RK schemes used in this study are briefly explained in the following sections.

### 2.2.1 Fourth-Order Runge-Kutta

The general form of the Butcher tableau for classical fourth-order four-stage RK (RK44) schemes is [125]

$$\begin{array}{c|cccc} 0 & & & & \\ \frac{1}{2} & \frac{1}{2} & & & \\ \frac{1}{2} & 0 & \frac{1}{2} & & \\ 1 & 0 & 0 & 1 & \\ \hline & \frac{1}{6} & \frac{1}{3} & \frac{1}{3} & \frac{1}{6} \end{array} \tag{2.8}$$

The RK44 temporal scheme is extensively used in the literature, and can be optimized as explained in the following sections.

### 2.2.2 Nasab-Pereira-Vermeire

Runge-Kutta stability polynomials can be optimized to generate new RK schemes that allow larger time step sizes, resulting in speedup factors of up to 1.97 relative to classical RK methods [56]. The general form of the Butcher tableau for the second-order Nasab-Pereira-Vermeire temporal scheme is

$$\begin{array}{c|cccccc} 0 & 0 & & & & & \\ c_2 & a_{2,1} & 0 & & & & \\ c_3 & a_{3,1} & a_{3,2} & 0 & & & \\ c_4 & a_{4,1} & 0 & a_{4,3} & 0 & & \\ \vdots & \vdots & \vdots & \vdots & \ddots & \ddots & \\ c_s & a_{s,1} & 0 & 0 & \cdots & a_{s,s-1} & 0 \\ \hline & 0 & 0 & 0 & \cdots & 0 & 1 \end{array} \tag{2.9}$$

The details for determining such optimum schemes are given by Hedayati et al. [56], who also provides optimal tableau's for FR schemes.

### 2.2.3 Paired Explicit Runge-Kutta

The P-ERK method allows RK schemes with a large number of derivative evaluations and large stability regions to be applied in stiff parts of the domain, while RK schemes with relatively few derivative evaluations can be applied in less stiff regions [54]. This feature globally increases the maximum permissible time step without requiring a large increase in cost per time step, yielding speedup factors of approximately five [54]. A general Butcher tableau for the P-ERK method is

$$\begin{array}{c|cccccc} 0 & 0 & & & & & \\ c_2 & a_{2,1} & 0 & & & & \\ c_3 & c_3 - a_{3,2} & a_{3,2} & 0 & & & \\ c_4 & c_4 - a_{4,3} & 0 & a_{4,3} & 0 & & \\ \vdots & \vdots & \vdots & \vdots & \ddots & \ddots & \\ c_s & c_s - a_{s,s-1} & 0 & 0 & \cdots & a_{s,s-1} & 0 \\ \hline & 0 & 0 & 0 & \cdots & 0 & b_s \end{array} \tag{2.10}$$

Thus, at each stage, a single unknown coefficient exists that can be determined via the general form of the scheme's stability polynomial. This polynomial is typically defined as a function of a complex variable and represents the accumulated error or amplification factor at each time step of the RK method. The stability polynomial of an explicit RK method can be determined directly from the Butcher tableau [126, 127]

$$P_{e,p}(z) = 1 + z\boldsymbol{b}^T(\boldsymbol{I} - z\boldsymbol{A})^{-1}\boldsymbol{e}, \tag{2.11}$$

or via Cramer's rule [126, 127]

$$P_{e,p}(z) = \frac{\det\left(\boldsymbol{I} - z\boldsymbol{A} + z\boldsymbol{e}\boldsymbol{b}^T\right)}{\det\left(\boldsymbol{I} - z\boldsymbol{A}\right)}, \tag{2.12}$$

where $\boldsymbol{I}$ is the identity matrix, $z$ is a point in the complex plane, and $\boldsymbol{e}$ is a vector of ones [54]. The details of determining P-ERK schemes are given by Vermeire [54, 55, 128].

### 2.2.4 Explicit Singly Diagonally Implicit Runge-Kutta

Explicit Singly Diagonally Implicit Runge-Kutta (ESDIRK) methods are attractive because they can provide high-order accurate solutions and can be used to obtain results with a lower level of numerical error, making them suitable for stiff differential equations [129]. The ESDIRK method is a special case of implicit RK methods in which the first stage is explicitly defined, and the remaining stages are implicitly defined. The advantage of this approach is that it allows for higher-order accuracy while maintaining stability and efficiency [130]. The general form of the Butcher tableau for ESDIRK schemes is

$$\begin{array}{c|cccccc} 0 & 0 & & & & & \\ c_2 & a_{2,1} & a_{2,2} & 0 & & & \\ c_3 & a_{3,1} & a_{3,2} & a_{3,3} & 0 & & \\ c_4 & a_{4,1} & a_{4,2} & a_{4,3} & a_{4,4} & 0 & \\ \vdots & \vdots & \vdots & \vdots & \vdots & \ddots & \\ c_s & a_{s,1} & a_{s,2} & a_{s,3} & a_{s,4} & \cdots & a_{s,s} \\ \hline & b_1 & b_2 & b_3 & b_4 & \cdots & b_s \end{array} \tag{2.13}$$

## 2.3 Flux Reconstruction

In this section, the FR formulation is explained for both one and multi-dimensional flows.

### 2.3.1 One Dimensional Formulation

The FR framework is explained here, following Huynh's formulation [64]. For simplicity consider the one-dimensional conservation law

$$\frac{\partial u}{\partial t} + \frac{\partial f}{\partial x} = 0, \quad x \in \Omega, \tag{2.14}$$

In the FR approach, the computational domain, $\Omega$, is partitioned into a mesh of $N_e$ non-overlapping elements such that

$$\Omega = \bigcup_{k=1}^{N_e} \Omega_k, \quad \bigcap_{k=1}^{N_e} \Omega_k = \emptyset. \tag{2.15}$$

Each element, $\Omega_k$, contains a number of solution points based on the desired solution polynomial degree, $\mathcal{P}$. For the sake of simplicity, these elements are transformed from the physical space $x$ to a standard reference space $\xi$. The transformation of these elements is done via an invertible mapping function, $M$, such that

$$x = M(\xi) \quad \Longleftrightarrow \quad \xi = M^{-1}(x). \tag{2.16}$$

The Jacobian of this mapping can be found at any point from

$$J = \frac{\partial x}{\partial \xi}, \tag{2.17}$$

which enables all element operations to be performed on the same reference element and, upon completion, mapped back to the physical system.

The exact solution, $u$, is approximated numerically, and within each element, via a solution polynomial of degree $\mathcal{P} = N_p - 1$, that is interpolated using these $N_p$ discrete values of the approximate solution. Similarly, the exact flux, $f$, within each element, $\Omega_k$, is approximated by a flux polynomial of degree $\mathcal{P} + 1$, which is usually discontinuous across cell interfaces. Hence, the total numerical solution, $u^\delta$, and flux, $f^\delta$, can be represented as the direct sum of their element-wise

approximations $u_k^\delta$ and $f_k^\delta$,

$$u^\delta = \bigoplus_{k=1}^{N_e} u_k^\delta \approx u, \qquad f^\delta = \bigoplus_{k=1}^{N_e} f_k^\delta \approx f. \tag{2.18}$$

The solution polynomials collectively form a global solution approximation, which is discontinuous across each cell interface. The solution polynomial within each element can be interpolated using the solution values at each solution point, in the reference space, using the nodal basis function at each solution point via

$$u_k^\delta(\xi, t) = \sum_{i=1}^{N_p} u_{k,i}^\delta(t)\psi_i(\xi), \tag{2.19}$$

where $u_k^\delta(\xi, t)$ is the interpolated solution polynomial within a reference element, $u_{k,i}^\delta(t)$ is the approximated value of the solution at the $i^{th}$ solution point, $\xi_i$, and $\psi_i(\xi)$ is the corresponding nodal basis function of the $i^{th}$ solution point, $\xi_i$, in the reference space. The nodal basis functions in the one-dimensional spatial coordinates are the well-known Lagrange polynomials,

$$\psi_i(\xi) = \prod_{j=1, j\neq i}^{N_p} \frac{\xi - \xi_j}{\xi_i - \xi_j}. \tag{2.20}$$

The general conservation law in the reference space can then be written approximately as

$$\frac{\partial u_k^\delta}{\partial t} + \frac{\partial f_k^\delta}{\partial \xi} = 0, \tag{2.21}$$

where $f_k^\delta$ is an interpolated continuous flux function in the reference space. The flux values at each solution point are computed using the solution values, then the flux function is interpolated to the cell boundaries and is usually discontinuous across cell interfaces. The discontinuous flux function is constructed similar to the solution polynomial,

$$f_k^{\delta D}(\xi, t) = \sum_{i=1}^{N_p} f_{k,i}^\delta(t)\psi_i(\xi), \tag{2.22}$$

where $f_k^{\delta D}(\xi, t)$ is the discontinuous flux function within a reference element, $f_{k,i}^\delta(t)$ is the approxi-

mated value of the flux at the $i^{th}$ solution point, $\xi_i$. The superscript $D$ denotes the discontinuity of the current flux approximation.

Since the spatial derivative of the flux function must be computed using a general conservation law, this function must be continuous to take the neighbouring elements data into account, and approximate the derivative of true flux function properly. In other words, to maintain global conservation, the flux between two elements must be continuous [131]. To address this discontinuity issue of the flux function, Huynh [64] proposed that a flux correction polynomial of degree $\mathcal{P}+1$ must be added to the discontinuous flux function,

$$f_k^{\delta} = f_k^{\delta D} + f_k^{\delta C}. \tag{2.23}$$

The computation of these corrections are given by Huynh [64] as follows, which approximates the zero function within the interior of the reference space

$$f_k^{\delta C} = \left(f_k^{CL} - f_{k,L}^{\delta D}\right) g_L + \left(f_k^{CR} - f_{k,R}^{\delta D}\right) g_R, \tag{2.24}$$

where $f_{k,L}^{\delta D} = f_k^{\delta D}(-1,t)$, and $f_{k,R}^{\delta D} = f_k^{\delta D}(1,t)$. Also, $f_k^{CL} = f_k^{CL}(u_{k,L}^-, u_{k,L}^+)$ and $f_k^{CR} = f_k^{CR}(u_{k,R}^-, u_{k,R}^+)$ are common interface fluxes, a function of extrapolated values of the solution at each edge of neighbouring elements. $f_k^{CL}$ and $f_k^{CR}$ are computed by a Riemann solver at the flux points between elements. The correction functions, $g_L = g_L(\xi)$ and $g_R = g_R(\xi)$, of degree $\mathcal{P}+1$ have the following constraints

$$g_L(-1) = 1, \qquad g_L(1) = 0, \tag{2.25}$$

$$g_R(-1) = 0, \qquad g_R(1) = 1. \tag{2.26}$$

The spatial derivative of the approximated continuous flux function of the general conservation law in reference space is now

$$\frac{\partial f_k^{\delta}}{\partial \xi} = \frac{\partial f_k^{\delta D}}{\partial \xi} + \frac{\partial f_k^{\delta C}}{\partial \xi} = \sum_{i=0}^{N_p} f_{k,i}^{\delta} \frac{\partial \psi_i}{\partial \xi} + \left(f_k^{CL} - f_{k,L}^{\delta D}\right) \frac{\partial g_L}{\partial \xi} + \left(f_k^{CR} - f_{k,R}^{\delta D}\right) \frac{\partial g_R}{\partial \xi}, \tag{2.27}$$

which is in the same polynomial space as $\partial u_k^\delta / \partial t$, and so both terms of the general conservation law are of a degree $\mathcal{P}$. The FR approach can be extended to higher-dimensions as explained in the next section.

### 2.3.2 Multi-Dimensional Formulation

The FR approach discretizes the divergence operator for general advection-diffusion equations of the form shown in Equation 1.9, and is extended to multi-dimensions for mixed element types by Wang and Gao [132]. FR is appealing due to its accuracy, generality, robustness, and suitability for modern hardware architectures [65]. Compared to commonly-used low-order numerical methods, FR provides more accurate solutions using fewer degrees of freedom and at reduced computational cost [45]. The FR framework is outlined in multiple dimensions, following Wang's formulation [132].

In this study, the solution points are located at the tensor product of Gauss-Legendre points for quadrilateral and hexagonal elements, Williams-Shunn points [133] for triangular elements, and Shunn-Ham points [134] for tetrahedral elements. The solution, flux, and mapping points for quadrilateral and triangular element types are depicted in Figure 2.1. The solution is approximated at each solution point, and then, the solution polynomial within each element is interpolated using nodal basis functions, ensuring element-wise continuity of the solution,

$$u_k^\delta(\boldsymbol{\xi}, t) = \sum_{i=1}^{N_p} u_{k,i}^\delta \psi_{k,i}(\boldsymbol{\xi}), \tag{2.28}$$

where $u_{k,i}^\delta$ is the numerical solution at point $i$ within element $k$. Furthermore, the flux polynomial is interpolated using nodal basis functions

$$\boldsymbol{f}_k^{\delta D}(\boldsymbol{\xi}, t) = \sum_{i=1}^{N_p} f_{k,i}^\delta \psi_{k,i}(\boldsymbol{\xi}), \tag{2.29}$$

where $f_{k,i}^\delta = f\left(u_{k,i}^\delta\right)$ is the numerical flux value at point $i$ within element $k$. The constructed

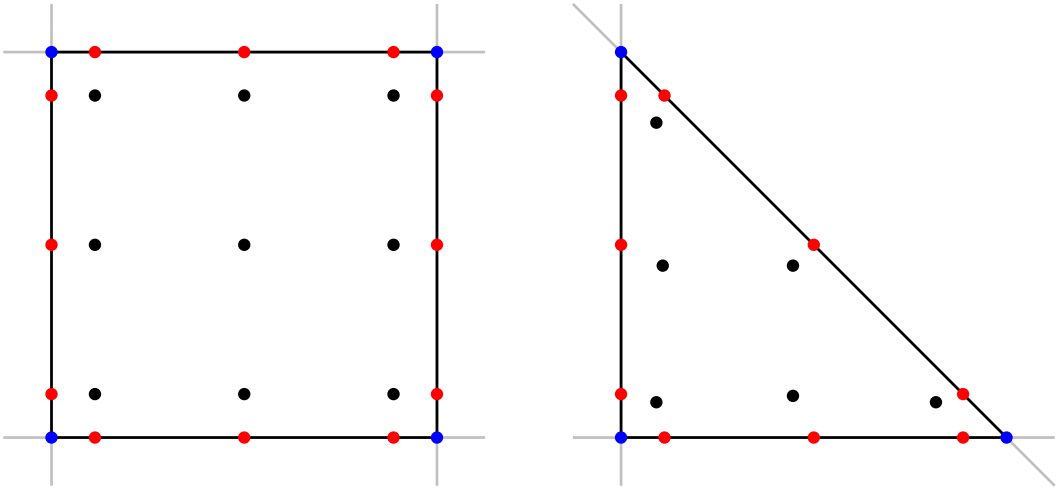

(a) Quadrilateral element types. (b) Triangular element types.

Figure 2.1. The computational element $\Omega_k$ with solution points in black, flux points in red, and mapping points in blue, for a $\mathcal{P}2$ discretization.

numerical flux function, $\boldsymbol{f}_k^{\delta D}(\boldsymbol{\xi}, t)$, is allowed to be discontinuous across cell interfaces, and the superscript $D$ denotes this discontinuity. Thus, a common Riemann flux must be defined to replace the normal flux. In this study, a Rusanov/Lax-Friedrichs flux is used at the interface between elements. To account for the jumps across cells, we follow Wang's formulation [132] for simplex elements. By defining a correction field, $\vartheta_k \in \mathbb{P}^{\mathcal{P}}$, Equation 1.9 is re-written within each element and must be satisfied at each solution point, i.e.,

$$\frac{du_{k,i}^{\delta}}{dt} + \left(\boldsymbol{\nabla} \cdot \boldsymbol{f}_k^{\delta}\right)_{\boldsymbol{\xi}_{k,i}} + \vartheta_{k,i} = 0. \tag{2.30}$$

The correction field ensures a globally continuous flux polynomial and can be determined for each solution point, $i$, within element $k$, by

$$\vartheta_{k,i} = \frac{1}{|\Omega_k|} \sum_{f_k \in \partial\Omega_k} \sum_j \alpha_{i,f_k,j} \left[\tilde{\boldsymbol{f}}\right]_{f_k,j} S_{f_k}, \tag{2.31}$$

where $f_k$ denotes the faces of the element $\Omega_k$, $j$ is the index for flux points, $\alpha_{i,f_k,j}$ are constant lifting coefficients, $\left[\tilde{\boldsymbol{f}}\right]_{f_k,j}$ is the difference between a common Riemann flux at point $j$ and the value of

the internal flux, and $S_{f_k}$ is the area of the face $f_k$. The lifting coefficients are computed using a weighting function, $W$, and are independent of both geometry and the solution [132]. In this study, the DG method is recovered via the FR formulation by choosing nodal basis functions as the weighting function [132], and the Rusanov and second method of Bassi and Rebay (BR2) are used for the common inviscid and viscous flux.

# Chapter 3

# Near-Field Optimization at Low Reynolds Numbers

## 3.1 Introduction

Aerodynamic shape optimization has been extensively researched, employing both gradient-free and gradient-based optimization techniques [121, 135, 136, 137]. Unsteady problems, typically associated with aeroacoustic and noise phenomena, pose challenges for adjoint methods due to their inherent instability. Consequently, for aeroacoustic shape optimization in this study, we adopt the gradient-free MADS optimization method [113], which has demonstrated favorable outcomes for aerodynamic shape optimization [121, 138].

In this chapter, our attention is directed toward near-field aeroacoustic shape optimization in two-dimensional flows. The term "near-field" pertains to the close vicinity of a sound source, usually within one wavelength of the emitted sound waves. Within this region, the sound field is complex, with varying pressure and velocity patterns. Given the observer's proximity to the source, sound pressure level computations exclusively rely on CFD data. Consequently, this chapter employs the direct CAA approach. The problems under investigation in this chapter are in two dimensions, which has limitations for acoustic prediction as it exaggerates the vortical structures

and turbulence is not present in two dimensions. While 2D models can provide useful insights and serve as preliminary tools for understanding aeroacoustic phenomena, they are inherently limited and may not accurately represent the full complexity of 3D flow-induced sound. The interaction between flow and acoustics is critical in generating noise, and these interactions may not be fully represented in 2D models. Therefore, for highly accurate predictions, 3D models are typically required, though practical constraints might necessitate the use of 2D models under certain circumstances. The efficiency of the proposed aeroacoustic shape optimization framework is evaluated for two-dimensional flows at low Reynolds numbers in this chapter.

The aeroacoustic shape optimization framework, illustrated in Figure 3.1, starts with the evaluation of the objective function for the baseline design. Subsequently, the MADS algorithm takes input comprising the baseline design, its objective function, constraints, and the initial mesh size parameter to identify candidate designs. Following candidate identification, the computational grid is generated for each design, and flow simulation is performed using HORUS, followed by post-processing scripts to evaluate the objective function. The minimum objective function value among the design candidates is compared to the incumbent design and the mesh size parameter is updated. The proposed aeroacoustic shape optimization framework employs a two-layer parallelism approach: HORUS operates in parallel using multiple CPUs, while objective function evaluations for candidate designs occur simultaneously. This iterative process continues until the problem converges. Gradient-free optimization techniques have previously used to reduce trailing-edge noise [118, 139, 140] and propeller noise [141, 142, 143]. However, to the author's knowledge, there is no previous work on coupling the high-order FR approach to the MADS optimization technique for aeroacoustic problems. Thus, the objective of this study is to investigate the feasibility of high-order numerical techniques coupled with gradient-free optimizers for aeroacoustic problems.

## 3.2 Flow Over an Open Deep Cavity

Flow over a two-dimensional deep cavity is a classical problem in fluid mechanics and aeroacoustics, and has been the subject of extensive research due to its relevance for a range of engi-

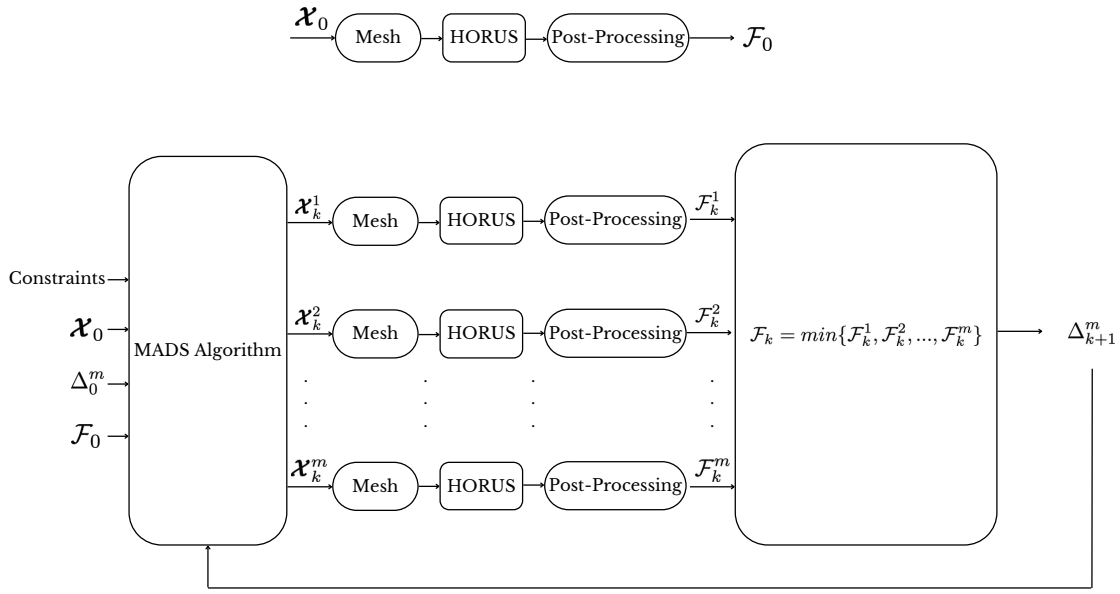


Figure 3.1. The aeroacoustic shape optimization framework for near-field.

neering applications. The flow over a cavity is characterized by a complex interplay between the boundary layer, the recirculation zone inside the cavity, and the external flow. The presence of the cavity can lead to a variety of aerodynamic and aeroacoustic phenomena, such as flow separation, unsteady vortex shedding, and acoustic resonance. Understanding the aerodynamic and aeroacoustic characteristics of flow over a cavity is crucial for optimizing the design and performance of many engineering systems. This topic has been studied using various techniques, including experiments [144], CFD simulations [145, 146], and aeroacoustic analysis [147, 148, 149]. The geometry of a cavity is typically given in terms of the length-to-depth ratio, $L/D$, depicted in Figure 3.2. The Reynolds number is usually based on the depth of the cavity, $Re_D = U_\infty D/\nu$, where $U_\infty$ is the free-stream velocity and $\nu$ is the kinematic viscosity. The numerical simulation is first validated using the numerical reference study [147], and then the optimization procedure is explained.

### 3.2.1 Validation

In this section, the flow simulation over an open deep cavity is validated by comparing the time history of drag coefficient, pressure perturbation coefficient, and the sound pressure level at observer locations with the reference data [147].

#### 3.2.1.1 Computational Details

To be consistent with the Larsson et al. [147], the entrance length of the domain is set to $5D$, which affects the oscillation regime significantly and results in a shear layer mode with the boundary layer thickness of $\delta \approx 0.2D$ at the cavity entrance. The outflow boundary is $80D$ away from the downstream cavity wall, where the last $50D$ of the downstream domain acts as a buffer region to eliminate the reflections of the acoustic waves from the computational boundaries. The resolved domain in the $y$-direction extends between $0 < y/D < 20$, and the buffer region extends between $20 < y/D < 40$. Stretching ratios of 1.05 and 1.075 are used in the resolved and buffer regions, respectively, with the smallest element size of $0.05D$ inside the cavity. A total of $13,076$ quadrangular elements are used to validate the open cavity with $\mathcal{P}2$, resulting in $117,684$ solution points. The boundary conditions of the domain, along with the cavity's geometry and mesh, are shown in Figure 3.2. The length-to-depth ratio of the cavity is $L/D = 4$, the Reynolds number based on the cavity depth is $Re_D = 1500$, and the inflow Mach number is $M_\infty = 0.15$.

#### 3.2.1.2 Results and Discussion

The simulation is run for $100t_c$, where $t_c = D/U_\infty$ and $U_\infty$ is the free-stream velocity, to allow initial transients to disappear and the simulation to reach a fully developed behavior. The drag coefficient of the open cavity is defined as

$$C_D = \frac{F_x}{\frac{1}{2}\rho_\infty U_\infty^2 D}, \tag{3.1}$$

where $\rho_\infty$ is the free-stream density, and $F_x$ is force per unit width in the $x$-direction and is computed on the three cavity walls. The drag coefficient of the open cavity is plotted against the

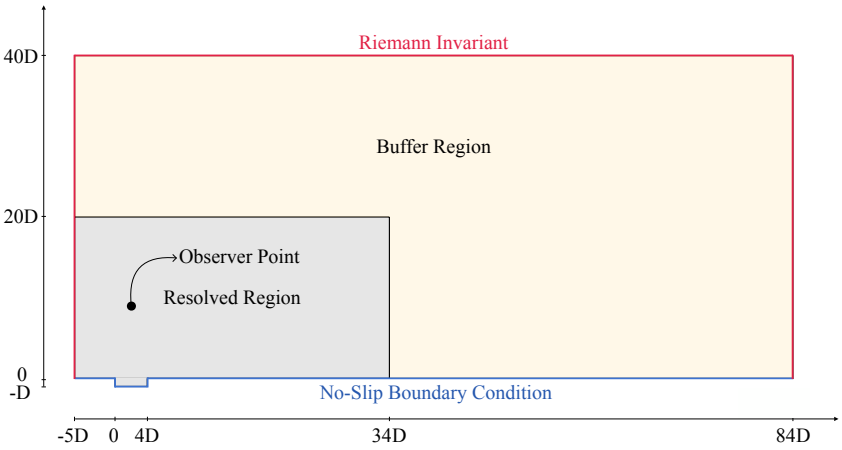


(a) The geometry.

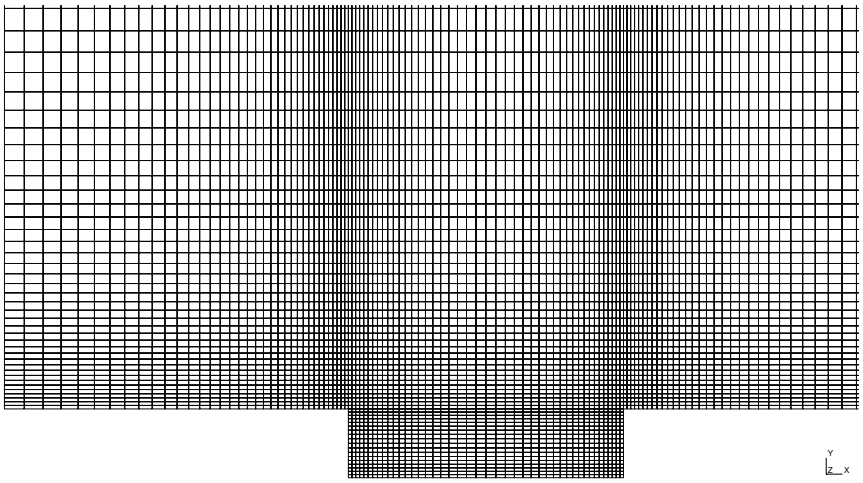

(b) The mesh around the cavity.

Figure 3.2. The computational domain of the open cavity.

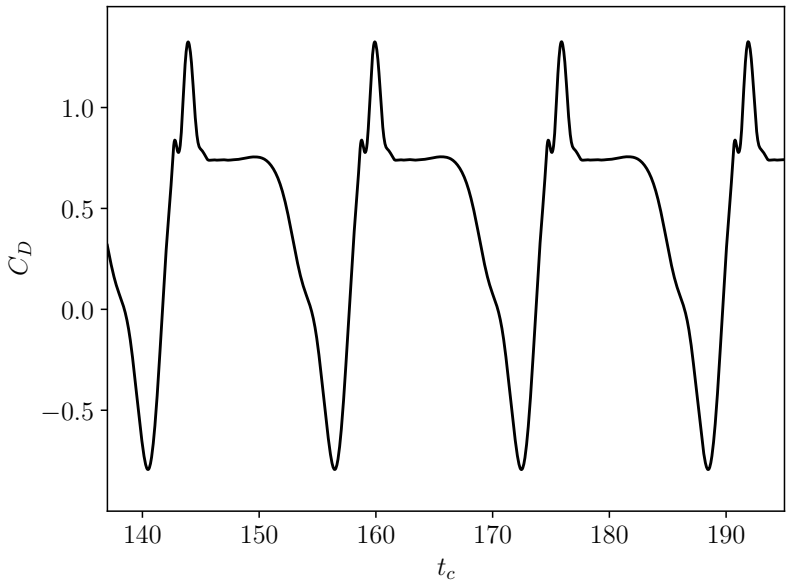


Figure 3.3. The time history of drag coefficient of the open cavity.

convective time in Figure 3.3. The pressure perturbation coefficient is defined as

$$C'_p = C_p - \overline{C_p}, \tag{3.2}$$

where $\overline{C_p}$ is the time-averaged pressure coefficient, and $C_p$ is the instantaneous pressure coefficient defined as

$$C_p = \frac{p - p_\infty}{\frac{1}{2}\rho_\infty U_\infty^2}, \tag{3.3}$$

where $p$ is the static pressure, and $p_\infty$ is the free-stream pressure. The $C'_p$ is plotted against $t_c$ for one convective time at an observer point located at $[x/D = 2, y/D = 7.16]$ in Figure 3.4. And, finally, the sound pressure level at a set of observer points is computed and shown in Figure 3.5. The $y$-location of all of the observer points is 7.16.

The drag coefficient, shown in Figure 3.3, is in good agreement with the reference [147]. However, there is a small deviation in both the perturbation pressure coefficient and sound pressure levels, shown in Figures 3.4 and 3.5, respectively, with reference [147]. The periodicity of the flow can be described by the fundamental or Strouhal frequency, where $St = 2.444$ based on the length

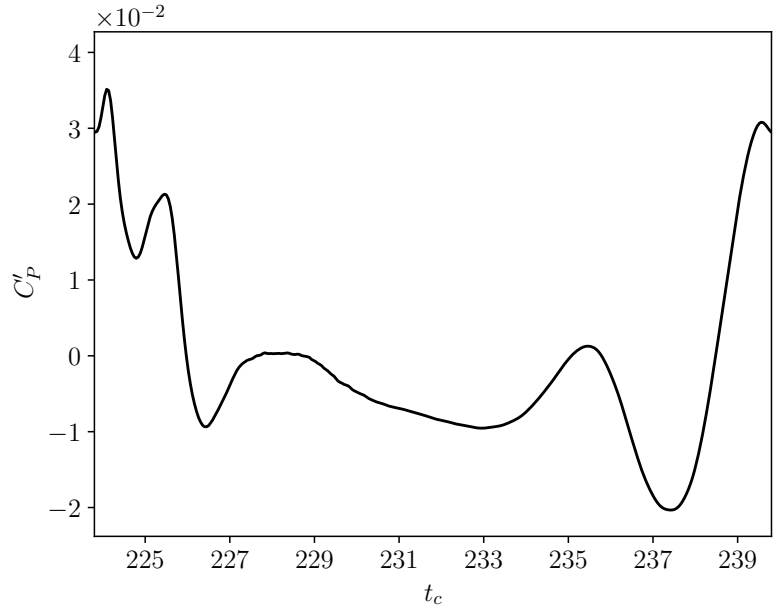


Figure 3.4. The pressure perturbation coefficient of the open cavity at $[x/D, y/D] = [2, 7.16]$.

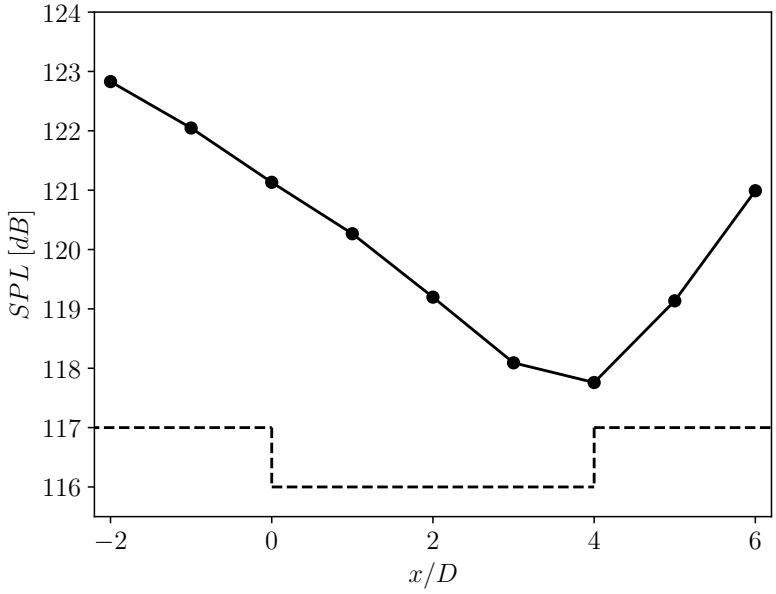


Figure 3.5. The SPL of the open cavity.

of the cavity, is in excellent agreement with the reported value of 2.45 [148].

Vortex structures and flow patterns are shown in Figure 3.6 at different times. The first and dominant vortex is shed from the upstream cavity inlet and evolves from the recirculation bubble at the cavity inlet, shown in Figure 3.6a. This vortex grows rapidly within the cavity while connected to the cavity's leading edge. Growth ceases when the vortex leaves the leading edge, and the free stream is injected into the cavity and upstream of the vortex (Figure 3.6b). As the primary clockwise-rotating vortex hits the trailing edge, a new counter-clockwise-rotating vortex is shed into the cavity at the trailing edge (Figure 3.6c), producing a high amplitude acoustic wave. The new counter-clockwise-rotating vortex then moves downstream (Figure 3.6d), cutting the primary vortex (Figure 3.6e). The primary vortex dictates the cavity flow's fundamental frequency and plays a crucial role in the sound generation of such flows [147].

In the next section, the height of the cavity trailing edge wall, shown in Figure 3.7, is optimized to reduce the sound perceived by an observer located at $[x/D, y/D] = [2, 7.16]$.

### 3.2.2 Optimization

In this section, the noise at the observer point located at $\boldsymbol{x}_{obs}/D = [2, 7.16]$ is minimized by changing the height of the cavity trailing edge wall, $h_{TE}$, using the MADS technique. Thus, $\boldsymbol{X} = [h_{TE}]$ is the design variable and $X_0 = 0$, while the objective function is the root-mean-squared of the pressure perturbation, $\mathcal{F} = p'_{rms}$.

#### 3.2.2.1 Results and Discussion

Upper and lower bounds of 0 and 4, respectively, are chosen for the design variable, $h_{TE}$, with the objective function being the root-mean-squared of the pressure perturbation at $\boldsymbol{x}_{obs}$. The design variable converged to $h_{TE} = 1.0156$ after 12 MADS iterations with a total of 23 objective function evaluations. The baseline and optimum designs are shown in Figure 3.8. The design space and the objective function convergence are shown in Figure 3.9. It can be seen from Figure 3.9a that a wide design space is investigated by the MADS optimization technique, and only two incumbent

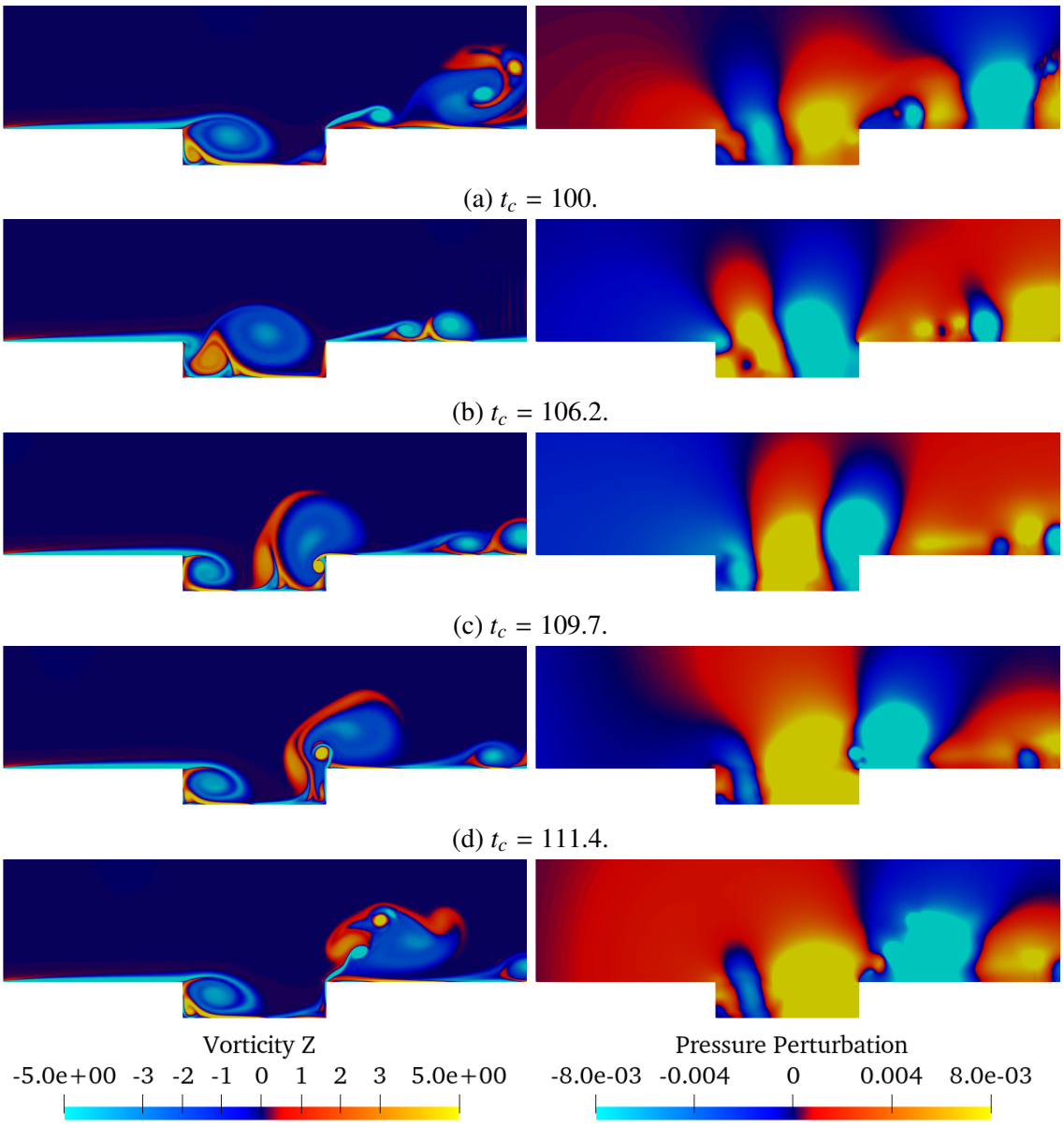


(a) $t_c$ = 100.

(b) $t_c$ = 106.2.

(c) $t_c$ = 109.7.

(d) $t_c$ = 111.4.

(e) $t_c$ = 113.2.

Figure 3.6. Z-component of the vorticity and pressure perturbation snapshots of the open cavity.

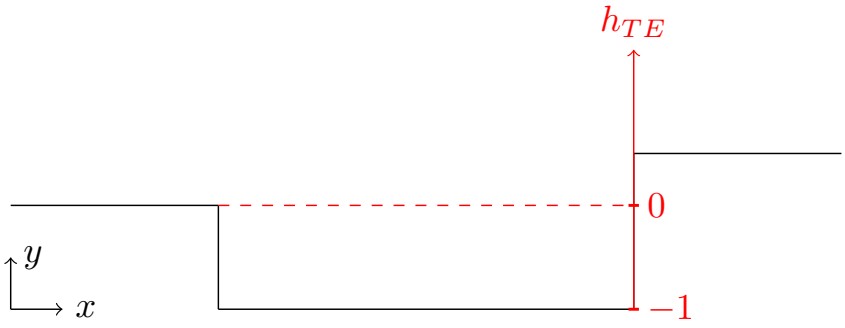


Figure 3.7. The height of the two-dimensional cavity's trailing edge used as a design variable.

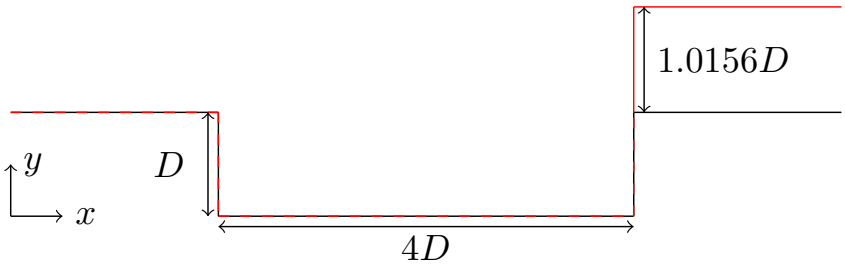


Figure 3.8. The baseline, in black, and optimum, in red, designs of the open cavity.

values are found, as shown in Figure 3.9b. The sound pressure level is decreased to 111.4 *dB* for the optimum design, down from 119.3 *dB* of the baseline design. Thus, a 7.9 *dB* decrease in the SPL at the observer is achieved. It can be seen from Figure 3.10 that the sound at all other observer points is also reduced, as expected. The z-component of the vorticity and pressure perturbation are plotted in Figure 3.11 at different times. For the optimized shape of the open cavity, the primary clockwise vortex trapped inside the cavity reduces the emitted noise. However, there are vortices shedding off the trailing edge of the cavity; but their acoustic waves are much smaller in amplitude compared to those of the baseline design.

## 3.3 Tandem Cylinders

The flow around two tandem cylinders consists of multiple flow features including flow separation, reattachment, recirculation, and quasi-periodic vortex shedding, amongst others. The physics

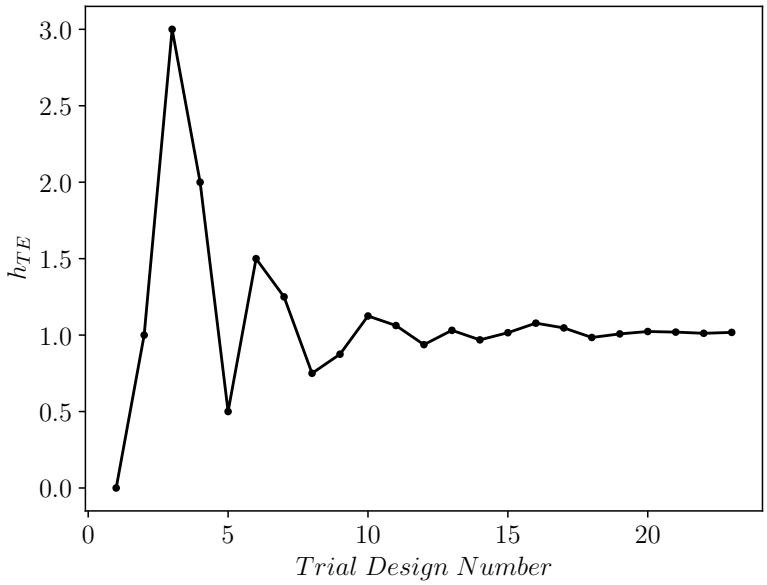


(a) The design space.

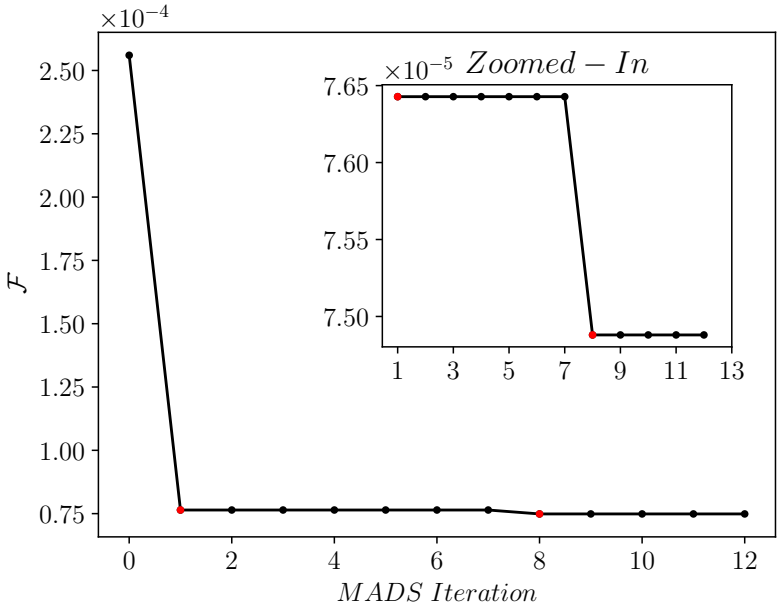


(b) The objective function convergence with the new incumbent designs highlighted in red.

Figure 3.9. The design space and objective function convergence for the open deep cavity.

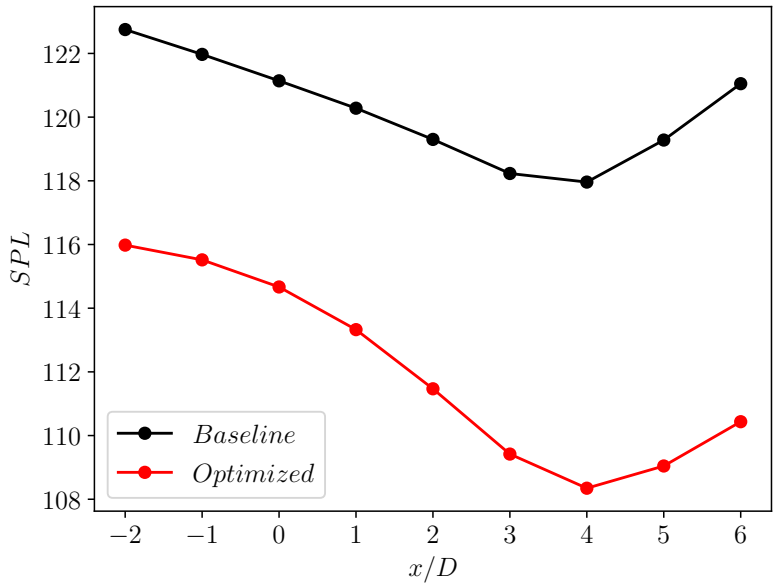


Figure 3.10. The SPL at different observer points for the optimum design of the open deep cavity.

of such flows is highly dependent on the diameter ratio of the cylinders, the spacing between them, and the Reynolds number. The diameter ratio of the cylinders is defined as $r = D_d/D_u$, where $D_d$ and $D_u$ are the downstream and upstream diameter of the cylinders, respectively. The spacing of the cylinders, $s$, is defined as the distance between the rear of the upstream cylinder to the front of the downstream cylinder. These definitions are depicted in Figure 3.12.

There is growing literature on flow over tandem cylinders [150, 151, 152] and the resulting acoustic field [153, 154, 155]. In the next section, the flow features of two cylinders in a tandem configuration are investigated, along with the sound radiated by them, and compared with reference data [151]. Finally, the diameter ratio between the cylinders and their distance are optimized to reduce the noise at the observer located $2D$ above the upstream cylinder.

### 3.3.1 Validation

In this section, the simulation of flow over tandem cylinders is validated by comparing the time history of lift and drag coefficients with the reference data [151]. The relationship between the mean time-averaged drag coefficient of the cylinders with the space between them is investigated

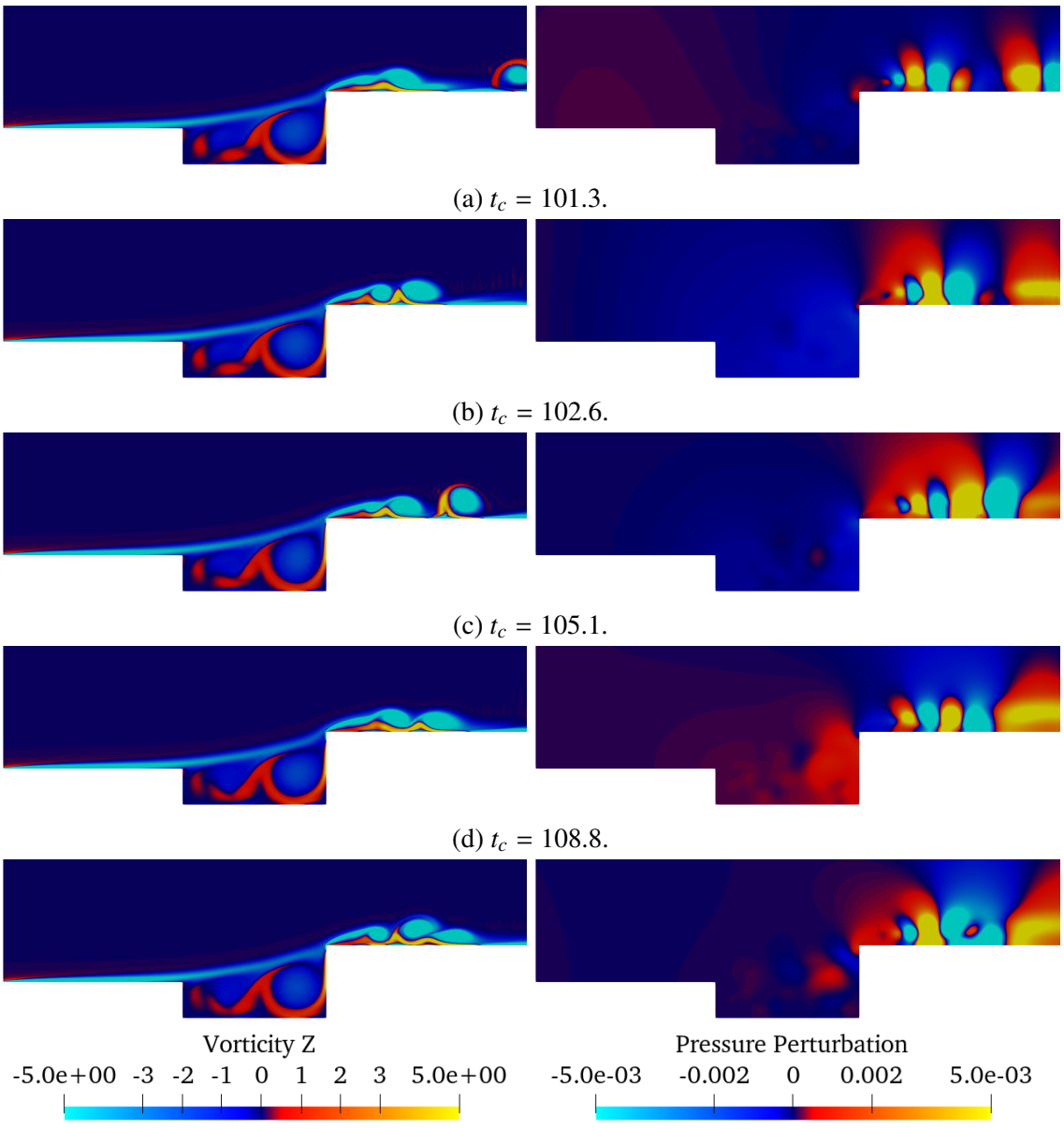


(a) $t_c$ = 101.3.

(b) $t_c$ = 102.6.

(c) $t_c$ = 105.1.

(d) $t_c$ = 108.8.

(e) $t_c$ = 110.3.

Figure 3.11. Z-component of the vorticity and pressure perturbation snapshots of the optimized open cavity.

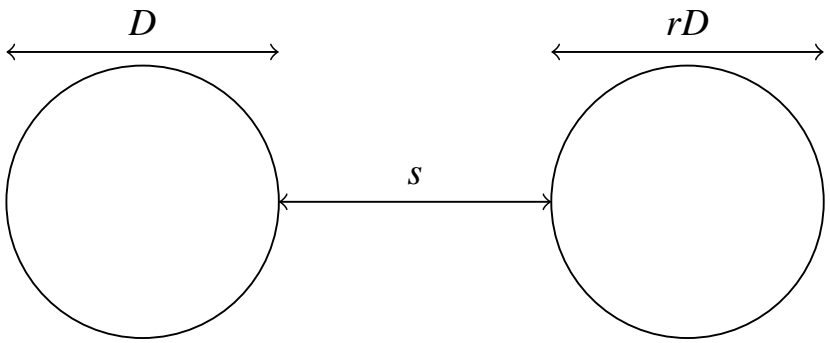


Figure 3.12. The arrangement of the tandem cylinders.

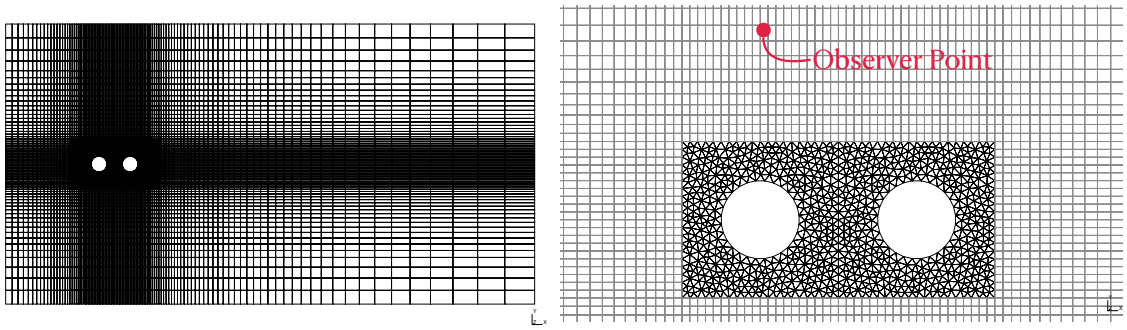


(a) The computational domain.

(b) The vicinity of the cylinders.

Figure 3.13. The computational grid for tandem cylinders.

and compared to the available literature [156].

#### 3.3.1.1 Computational Details

The tandem cylinders configuration is first run for $r = 1$ and $s = 4.5$. A total of $8,718$ triangular and quadrilateral elements are used, and the computational grid is shown in Figure 3.13. The simulation is started with a $\mathcal{P}1$ simulation, switched to $\mathcal{P}2$ after $1500t_c$, and then, is run for $500t_c$ to compute the statistical characteristics of the flow. $t_c = D/U_\infty$ is the time needed for flow to pass the upstream cylinder or the convective time, and $U_\infty$ is the free-stream velocity. The Reynolds number for this study is $Re = 200$, and the inflow Mach number is $M_\infty = 0.2$. The 6-stage $5^{th}$-order accurate ESDIRK temporal scheme [157] is used to advance the simulation in time.

#### 3.3.1.2 Results and Discussion

The lift and drag coefficients for both the upstream and downstream cylinders are obtained for $s = 4.5$ and are shown in Figure 3.14, where good agreement is observed comparing with reference data [151]. The drag coefficients of the two cylinders are obtained by integrating the pressure and shear stress distributions on the surface and then are averaged for 500 convective times. The time-averaged drag coefficient, $\overline{C_D}$, is plotted for different values of $s$ in Figure 3.15, and shows a similar trend to Igarashi [156]. The time-averaged drag coefficient of the upstream cylinder, $\overline{C_{D1}}$, decreases gradually by increasing the cylinder spacing, $s$, and increases stepwise for $s/D > 3$. On the other hand, the time-averaged drag coefficient of the downstream cylinder, $\overline{C_{D2}}$, is negative for $s/D < 3$ acting as a thrust force. $\overline{C_{D2}}$ increases as the downstream cylinder is placed further away from the upstream cylinder, and a sudden increase occurs for $s/D > 3$.

### 3.3.2 Optimization

In this study, the distance between the two cylinders, $s$, and the ratio between the diameters of the cylinders, $r$, are the design variables, $\boldsymbol{X} = [s, r]$. The objective function is $\mathcal{F} = p'_{rms}$ at $2D$ above the upstream cylinder, depicted in Figure 3.13b. Considering that the main objective of this study is to demonstrate the optimization capabilities of MADS, a loud initial design has been selected to evaluate the feasibility of optimizing towards a quieter configuration.

#### 3.3.2.1 Results and Discussion

The optimization problem converges after 27 MADS iterations, including 70 objective function evaluations. The design space and objective function convergence are shown in Figure 3.17, where the optimum design is found as $(s, r) = (1.6301D, 1.1594D)$. The baseline and optimum design are demonstrated in Figure 3.16. The optimization procedure has covered a wide range of design variables, as shown in Figure 3.17a. Instantaneous vorticity contours and acoustic fields are shown for the initial design and the optimum design, in Figure 3.18, at $t_c = 2000$. Comparing these two figures, the vortical structures have been significantly reduced, especially in the wake region of the

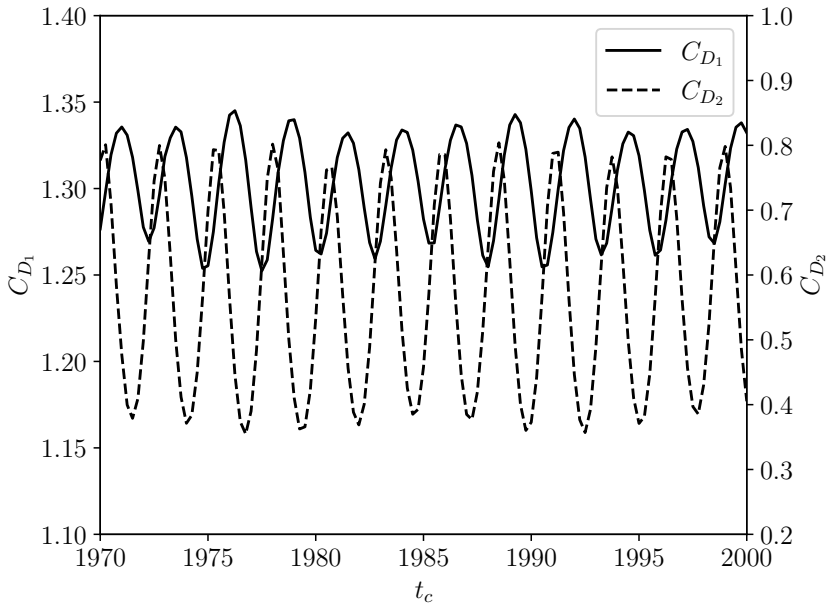


(a) The drag coefficient.

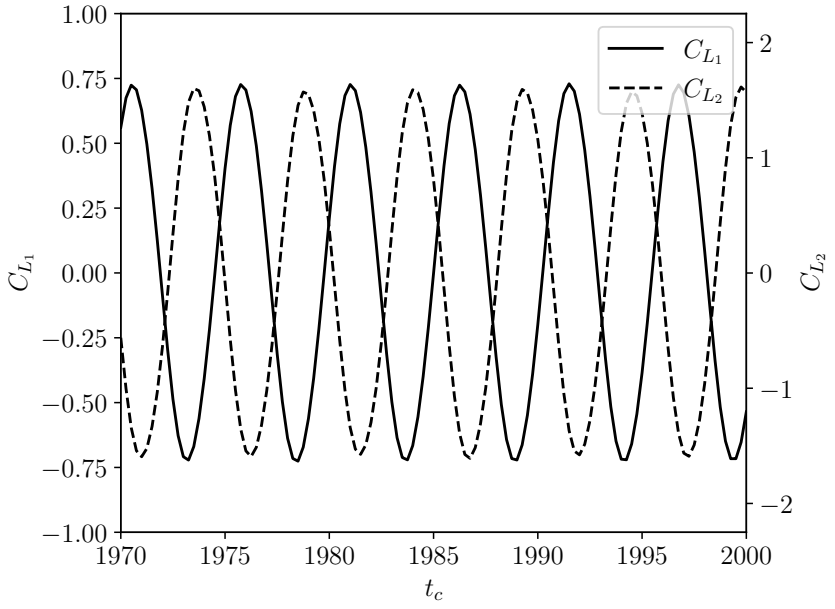


(b) The lift coefficient.

Figure 3.14. The lift and drag coefficients of flow past a pair of tandem cylinders ($s = 4.5$) at $Re = 200$.

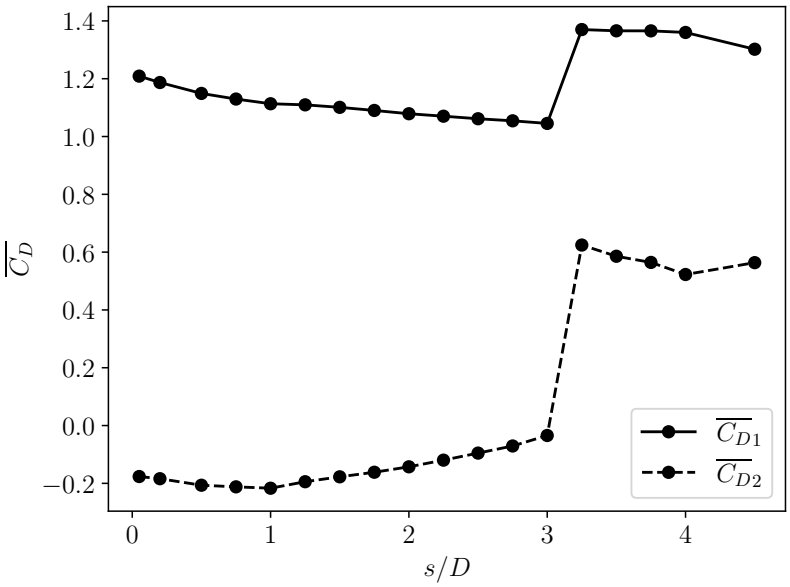


Figure 3.15. Drag coefficient for the tandem cylinders versus separation ratio.

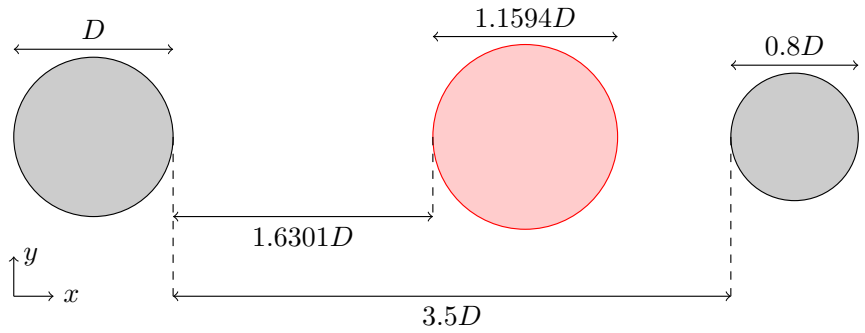


Figure 3.16. The baseline, in black, and optimum, in red, designs of the tandem cylinders.

upstream cylinder which drastically reduces noise. The sound pressure level of the initial design at the observer, $2D$ above the upstream cylinder, is 136.3 $dB$, which reduces to 119.8 $dB$ for the optimized configuration. Thus, a 16.5 $dB$ decrease in overall SPL is achieved.

## 3.4 NACA 4-Digit Airfoil

The aerodynamic characteristics of the NACA0012 airfoil have been extensively studied through experiments [158, 159, 160, 161] and CFD simulations [162, 163]. This airfoil has a relatively high

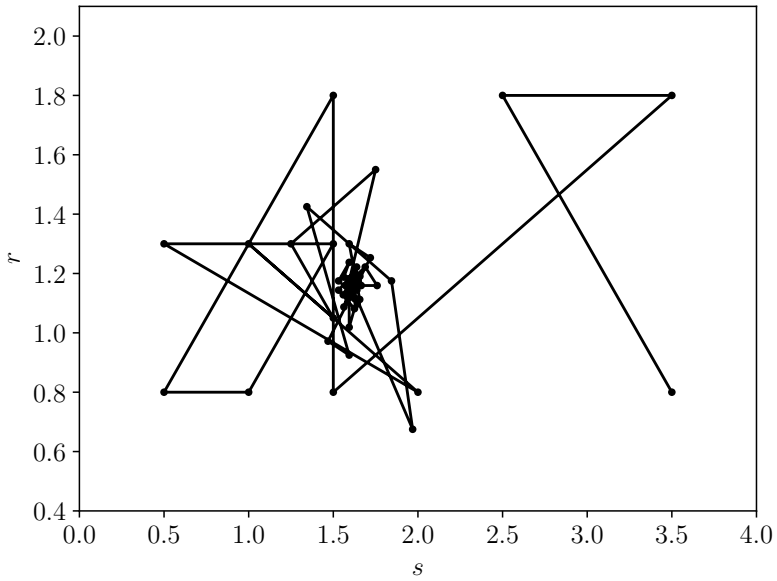


(a) The design space.

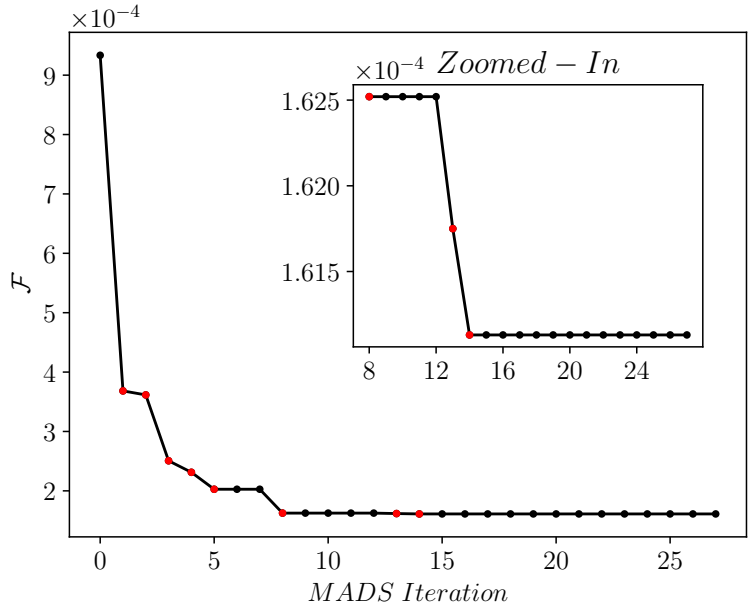


(b) The objective function convergence with the new incumbent designs highlighted in red.

Figure 3.17. The design space and objective function convergence for the tandem cylinders.

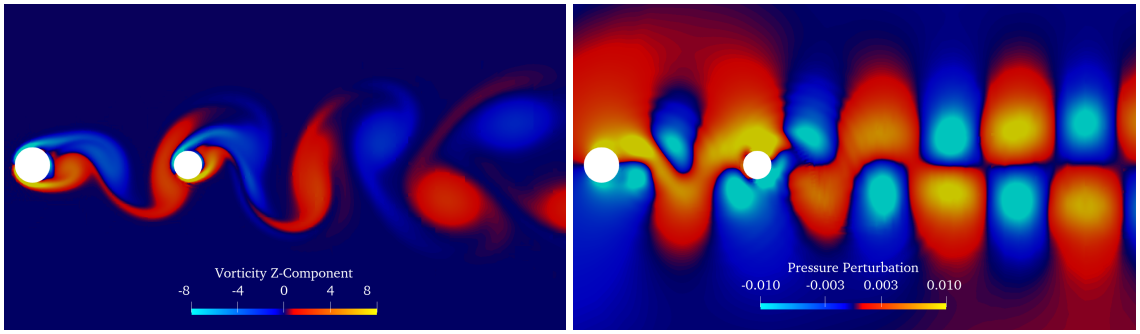


(a) The initial tandem cylinder design.

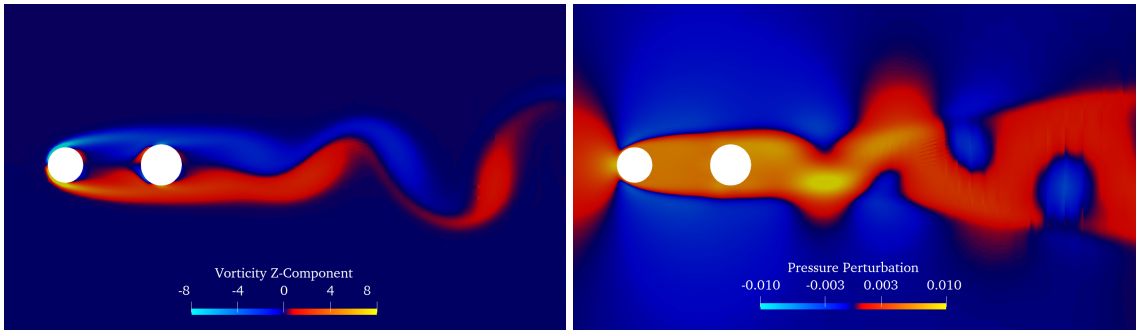


(b) The optimum tandem cylinder design.

Figure 3.18. The z-component of the vorticity and pressure perturbation snapshots at $t_c = 2000$.

maximum lift coefficient, which makes it suitable for use in low-speed applications such as general aviation, Unmanned Aerial Vehicles (UAVs), and Micro Aerial Vehicles (MAVs). At low Reynolds numbers, less than $Re = 10^5$, the boundary layer is laminar. In general, two different types of acoustic spectra are observed in flow past a laminar airfoil, depending on the Reynolds number and angle of attack. First, a typical tone noise phenomenon, i.e., a broadband contribution with a dominant frequency along with equidistant frequency tones, and second, a simple broadband spectrum [164]. In the first type, the sequence of regularly-spaced discrete frequency tones is due to the emergence of a separation bubble on the pressure surface close to the trailing edge [164]. On the pressure side, the hydrodynamics fluctuations are coherent in the spanwise direction [158]. Thus, it can be assumed that the governing mechanism of tonal noise is essentially two-dimensional [164].

The study of airfoil noise dates back to the 1970s when several experimental studies showed that discrete tones are emitted from isolated airfoils [165, 166], and other studies focused on un-

derstanding this phenomenon [158, 160, 167]. The shape of the airfoil is optimized for noise reduction of the high-lift devices [168], laminar flow trailing edge [169, 170], and turbulent flow trailing edge [118, 171]. This study examines the laminar flow trailing edge and the aeroacoustic shape optimization of the NACA0012 airfoil at a low Reynolds number, $Re = 10,000$, which is the operating regime for MAVs.

### 3.4.1 Validation

In this section, flow over a two-dimensional NACA0012 airfoil is validated. A grid-resolution-independence study is performed for the time-averaged lift and drag coefficients, and the sound pressure level at an observer located a unit chord length above the trailing edge. The time-averaged lift coefficient is compared with reference DNS data [172] to validate the simulation.

#### 3.4.1.1 Computational Details

The computational grid consists of 19,596 quadrangular elements, depicted in Figure 3.19. The domain is extended to $5c$ in the $y$-direction and to $10c$ in the $x$-direction, where $c = 1$ is the chord length of the airfoil. The stretching ratio is kept below 5% everywhere in the domain. The elements in the wake region are inclined at the angle of attack to capture the vortices behind the trailing edge. The computational domain is shown in Figure 3.19. The Reynolds number for this study is $Re = 10,000$, the inflow Mach number is $M_\infty = 0.2$, the angle of attack is 3 degrees, and the Prandtl number is $Pr = 0.71$. The simulation is run for 60 convective times, and flow statistics are averaged for the last 20 convective times. The second-order Paired Explicit Runge-Kutta (P-ERK) temporal scheme [54, 55] is used to advance the solution in time.

Vortices leaving the computational domain can generate non-physical acoustic wave reflections off the boundaries, contaminating the solution. Thus, the strength of such vortices must be decreased to eliminate the acoustic wave reflections off the boundaries. The addition of artificial diffusion and variable solution polynomial degrees are used in this study, shown in Figure 3.20. Artificial diffusion is applied beyond a circle with a radius of $2c$ centered at the trailing edge. Its

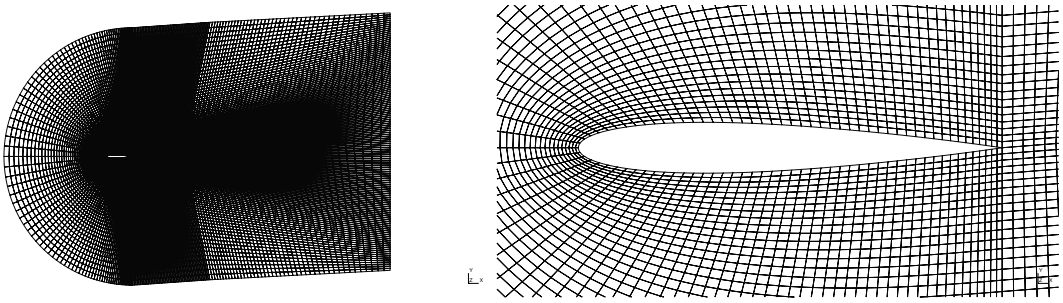

(a) The computational domain. (b) The vicinity of the airfoil.

Figure 3.19. The computational grid for NACA0012 airfoil at $\alpha = 3°$.

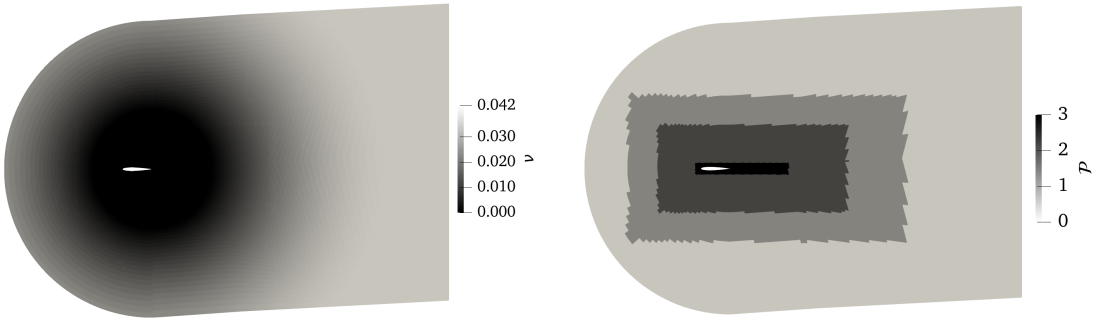


(a) The artificial diffusion. (b) The polynomial distribution.

Figure 3.20. The boundary treatments.

magnitude increases to a maximum of 0.01 and a radius of $8c$ using a sinusoidal function. The solution polynomial distribution is shown in Figure 3.20b, where in the vicinity of the airfoil $\mathcal{P} = 3$ and it decreases to zero close to the boundaries.

#### 3.4.1.2 Results and Discussion

A different set of variable polynomial degrees are used to study the independence of the results to the grid resolution. Three different mesh resolutions are used with a maximum polynomial degree of $\mathcal{P}2$, $\mathcal{P}3$, and $\mathcal{P}4$, shown in Figure 3.21.

The time-averaged lift and drag coefficients are computed along with the sound pressure level at the observer located a unit chord length above the trailing edge and compared using three different grid resolutions, shown in Table 3.1. The time-averaged lift coefficient differs by less than 0.4% when the highest polynomial degree in the domain is $\mathcal{P}4$ compared to that of $\mathcal{P}3$, while the time-averaged drag coefficient remains the same by three significant digits. The time-averaged lift

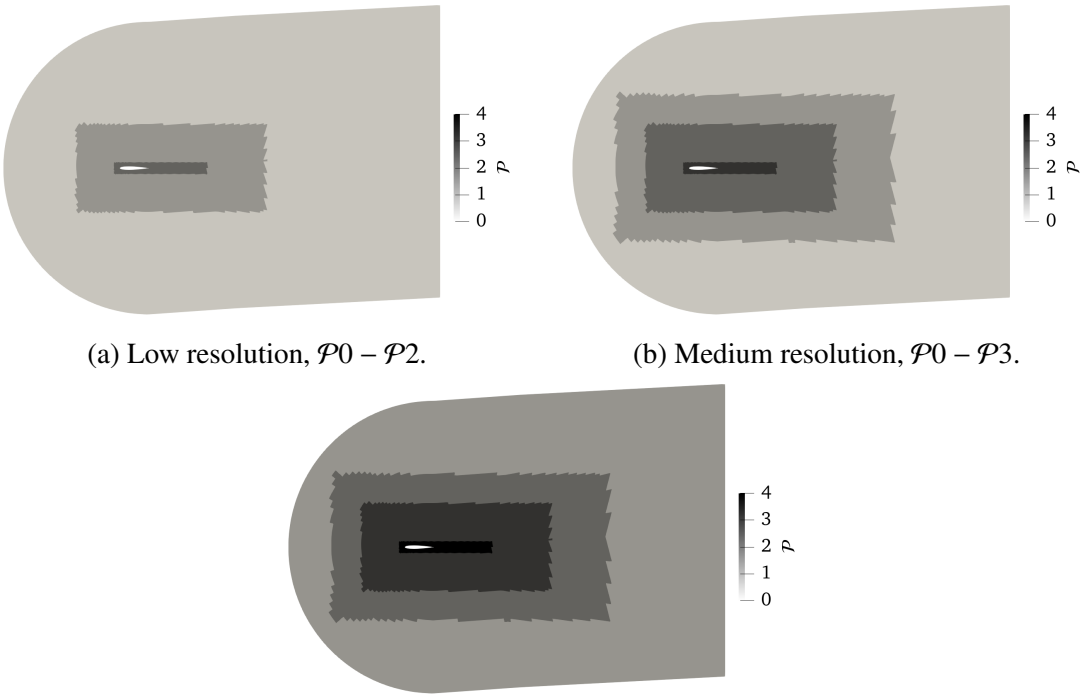


(a) Low resolution, $\mathcal{P}0 - \mathcal{P}2$.

(b) Medium resolution, $\mathcal{P}0 - \mathcal{P}3$.

(c) High resolution, $\mathcal{P}1 - \mathcal{P}4$.

Figure 3.21. The three different resolutions to study the grid resolution independency of the results.

Table 3.1. Averaged lift and drag coefficients and the sound pressure level measured at a unit chord distance above the trailing edge of the baseline NACA0012.

| | $\mathcal{P}0 - \mathcal{P}2$ | $\mathcal{P}0 - \mathcal{P}3$ | $\mathcal{P}1 - \mathcal{P}4$ |
|---|---|---|---|
| $\overline{C_L}$ | 0.0877 | 0.0886 | 0.0889 |
| $\overline{C_D}$ | 0.0448 | 0.0447 | 0.0447 |
| $SPL$ | 109.6 $dB$ | 110.0 $dB$ | 110.5 $dB$ |

coefficient obtained via the $\mathcal{P}0-\mathcal{P}3$ simulation agrees well with the DNS data [172]. Furthermore, the sound pressure level difference between $\mathcal{P}0 - \mathcal{P}3$ and $\mathcal{P}1 - 4$ simulations is 0.5 $dB$ or 0.48%. Thus, it is concluded that the grid resolution for $\mathcal{P}0 - \mathcal{P}3$ simulation is sufficient for this problem.

The sensitivity of the time-averaged quantities to the averaging window is investigated by choosing two different averaging windows. The lift and drag coefficients are averaged over 20 and 40 convective time windows, shown in Table 3.2. The difference between the time-averaged lift and drag coefficients for both averaging window lengths is negligible. Thus, the quantities are averaged over a 20 convective time window.

The time history of lift and drag coefficients are shown in Figure 3.22 for the last two convective

Table 3.2. Averaging window sensitivity of the time-averaged quantities.

| | 20 $t_c$ | 40 $t_c$ |
|---|---|---|
| $\overline{C_L}$ | 0.08857 | 0.08863 |
| $\overline{C_D}$ | 0.04472 | 0.04473 |

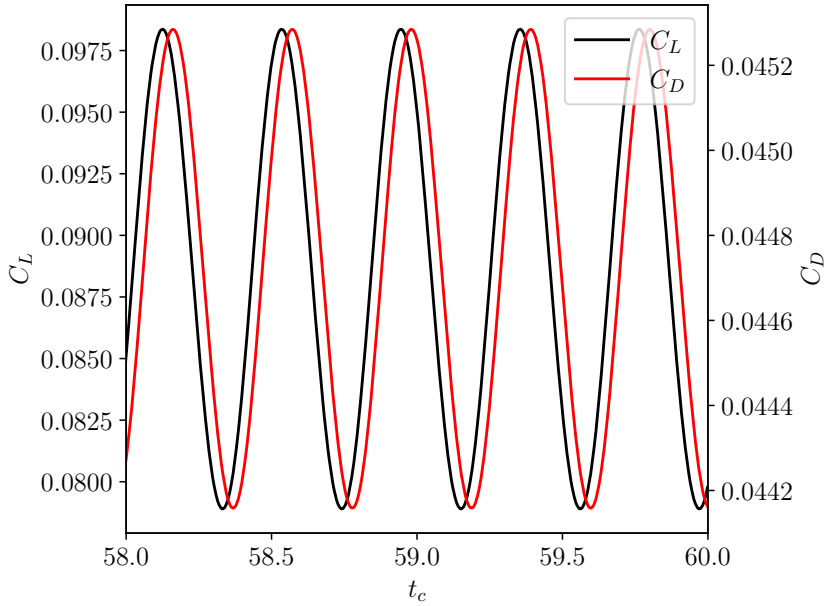


Figure 3.22. Time-histories of lift and drag coefficients.

times. The periodic behaviour of $C_L$ and $C_D$ is associated to the periodic vortex shedding at the trailing edge.

The pressure perturbation at $t_c = 60$ is shown in Figure 3.26a. Acoustic waves are generated close to the trailing edge and propagate everywhere in the domain. There are no visible acoustic wave reflections off the boundaries, showing the effectiveness of boundary treatments used in this study. The amplitude of the pressure perturbations is higher in the wake region and behind the trailing edge where the vortices are shed and travel downstream. The addition of artificial viscosity, as shown in Figure 3.20a, dampens these vortices and consequently reduces the amplitude of acoustic waves far from the trailing edge.

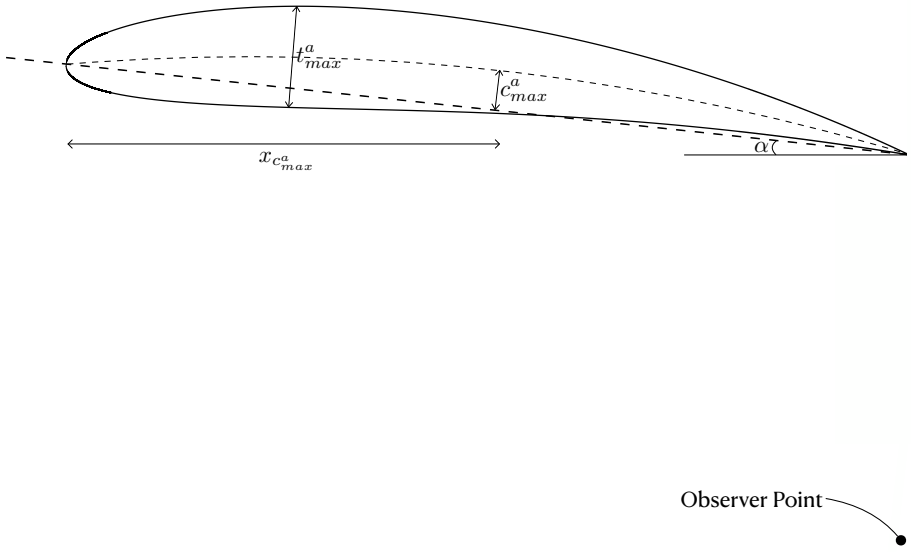


Figure 3.23. The design variables and the observer point located at a unit chord length below the trailing edge for the two-dimensional NACA 4-digit airfoil.

### 3.4.2 Optimization

In this section, the noise at an observer located at a unit chord length below the trailing edge is reduced. A total of four design parameters are chosen based on the NACA 4-digit airfoil series. The maximum camber, $c^a_{max}$, the distance of maximum camber from the airfoil leading edge, $x_{c^a_{max}}$, maximum thickness of the airfoil $t^a_{max}$, and the angle of attack, $\alpha$, are the four design parameters, i.e. $\boldsymbol{X} = [c^a_{max}, x_{c^a_{max}}, t^a_{max}, \alpha]$, depicted in Figure 3.23. The simulation is first run for 60 convective times for each objective function evaluation. Then the time-averaged pressure is computed from $20t_c$ to $40t_c$, $\overline{p}_{20-40}$, and then from $40t_c$ to $60t_c$, $\overline{p}_{40-60}$. If the difference between $\overline{p}_{20-40}$ and $\overline{p}_{40-60}$ is above one percent, the simulation is run for 20 more convective times. The simulation is run long enough so that the difference between two consecutive time-averaged pressure signal, over $20t_c$, is below one percent.

#### 3.4.2.1 Results and Discussion

The optimization procedure is run using a maximum polynomial degree of $\mathcal{P}3$, shown in Figure 3.21b. The maximum camber range is set to $c^a_{max} \in [-10, 10]$ as a percentage of the chord, with the distance from the airfoil leading edge in the range of $x_{c^a_{max}} \in [2, 9]$ as a tenth of the chord. The

maximum thickness of the airfoil is within the range of $t^a_{max} \in [8, 16]$ as a percentage of the chord. Finally, the angle of attack varies from $-5°$ to $5°$. The objective function is defined as the sound pressure level at the observer with constraints on both the mean lift and mean drag coefficients. A quadratic penalty term is added to the objective function when the lift coefficient deviates from the baseline design, and an additional quadratic penalty term is added when the mean drag coefficient is above the baseline design. The objective function is defined as

$$\mathcal{F} = \begin{cases} SPL + \epsilon\left(\overline{C_L} - \overline{C_{L,baseline}}\right)^2 + \epsilon\left(\overline{C_D} - \overline{C_{D,baseline}}\right)^2 & \overline{C_D} > \overline{C_{D,baseline}} \\ SPL + \epsilon\left(\overline{C_L} - \overline{C_{L,baseline}}\right)^2 & \overline{C_D} \leq \overline{C_{D,baseline}} \end{cases}, \tag{3.4}$$

where the constant $\epsilon$ is set to $400,000$ to compensate for the order of magnitude difference in $SPL$ and $\overline{C_L}$ and $\overline{C_D}$. The defined objective function minimizes the sound pressure level while keeping the mean lift coefficient intact, and ensures the optimized airfoil has a similar or lower mean drag coefficient.

This optimization procedure converges after 39 MADS iterations, consisting of 149 objective function evaluations. The design space and the convergence of the objective function are shown in Figure 3.25. The optimal airfoil design has a maximum camber of $c^a_{max} = -0.8944$ percent of the chord, at a 2.1428 tenth of the chord distance from the leading edge, with a thickness of $t^a_{max} = 9.1309$ percent of the chord, at an angle of attack of $\alpha = 1.9350$ degrees. The baseline and optimum design are demonstrated in Figure 3.24. The optimized airfoil is silent with $SPL = 0\ dB$, maintains and unchanged mean lift coefficient of $\overline{C_L} = 0.0886$, and achieves a reduced mean drag coefficient by 24.95% to $\overline{C_D} = 0.0348$. And, finally, the pressure perturbation and z-component of vorticity are shown in Figure 3.26 for the baseline and optimum designs. In the baseline design, the flow is attached to the airfoil on the pressure side, and flow instability occurs on the suction side. A periodic vortex shedding takes place as the flow passes over the trailing edge, resulting in acoustic wave generation. However, in the optimum design, the flow instability is eliminated resulting in a silent airfoil.

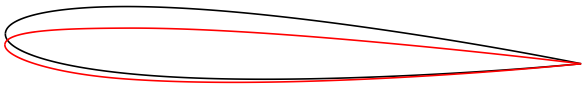

Figure 3.24. The baseline, in black, and optimum, in red, designs of the NACA 4-digit airfoil.

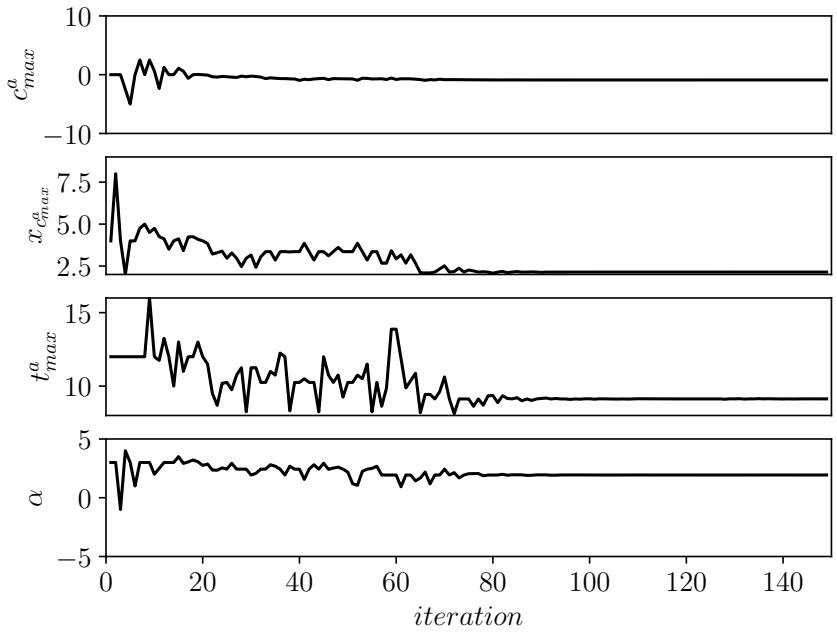


(a) The design space.

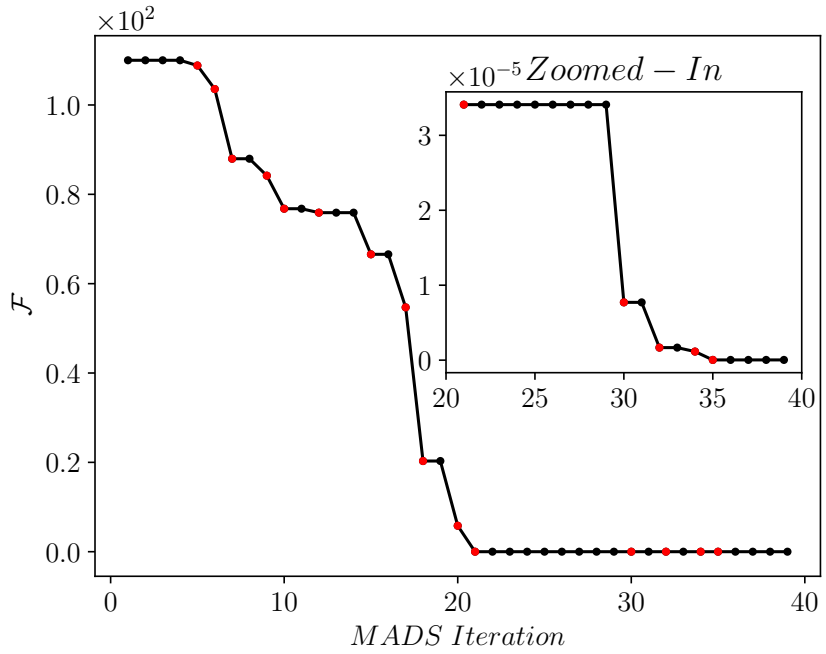


(b) The objective function convergence with the new incumbent design highlighted in red.

Figure 3.25. The design space and objective function convergence for $\mathcal{P}3$ optimization of the NACA 4-digit airfoil.

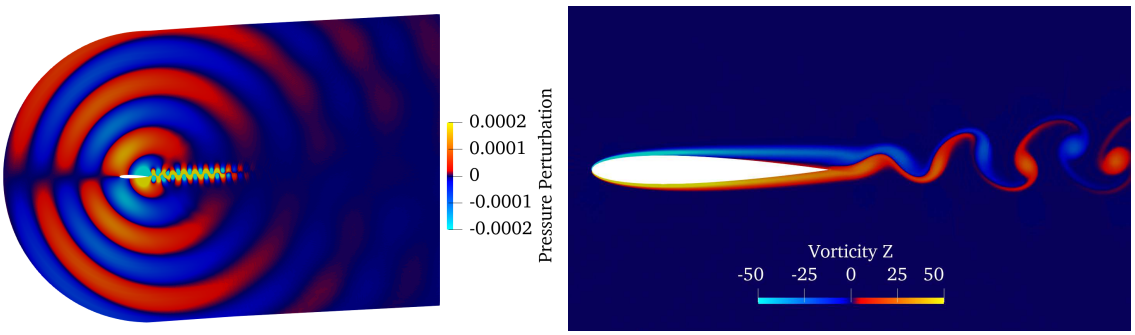


(a) The baseline design.

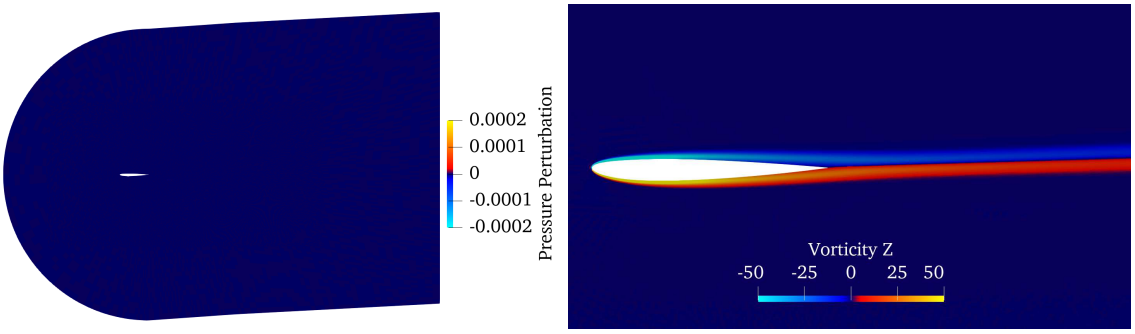


(b) The optimum design.

Figure 3.26. The pressure perturbation and vorticity in the z-direction for the baseline and $\mathcal{P}3$ optimization designs of NACA 4-digit airfoil at $t_c = 60$.

# Chapter 4

# Near-Field Optimization Using Large Eddy Simulation

## 4.1 Introduction

This chapter expands upon the research conducted in Chapter 3 by addressing three-dimensional problems. The benchmark problems from Chapter 3 are extruded in the z-direction. Then, the shape optimization technique is performed to minimize the emitted noise perceived by a near-field observer. The MADS algorithm employs minimal positive bases construction for the cavity and tandem cylinder flow and maximal positive bases construction for airfoil flow. The optimization problem converges when the mesh size parameter is less than $10^{-6}$, and the change in design variables between consecutive iterations is under one percent.

## 4.2 Flow Over an Open Deep Cavity

Airframe noise can originate from various sources, including panel gaps located on the aircraft's body, which may exist between doors or windows and the fuselage, as well as between control surfaces on a wing. This section focuses on examining the flow over an open deep cavity, providing a simplified model for studying these panel gaps. Extensive research has been con-

ducted on two-dimensional cavity flows, leading to favorable agreement between experimental data and numerical two-dimensional simulations. While three-dimensionality is observed in cavity flow experiments, it underscores the significance of conducting three-dimensional cavity flow simulations [173, 174]. Lawson [175] reviewed the experimental and numerical studies of open cavities. Furthermore, the radiated noise from cavity is studied via LES by several researchers [90, 176, 177, 178]. The geometry of a three-dimensional cavity is usually given in terms of length-to-depth, $L/D$, and width-to-depth, $W/D$, ratios, as depicted in Figure 4.1. In this section, flow over an open cavity is validated and then the noise at a near-field observer is minimized via gradient-free shape optimization.

### 4.2.1 Validation

In this section, we extend our previous computational domain in Section 3.2 by extruding it in the z-direction. The grid convergence study is performed using the time-averaged drag coefficient, and sound pressure level measured at an observer located $7.16D$ above the cavity center.

#### 4.2.1.1 Computational Details

To be consistent with Section 3.2, the open cavity with a length-to-depth ratio of $L/D = 4$ is extruded in the z-direction with a width-to-depth ratio of $W/D = 3$. The Reynolds number, based on the depth of the cavity, is $Re_D = 1500$, and the Mach number is 0.15. To ensure wake mode oscillations, the inlet boundary is placed $5D$ upstream of the cavity inlet, resulting in a boundary layer thickness of $\delta/D \approx 0.2$ at the entrance of the cavity. The outflow boundary is placed $60D$ downstream of the cavity's trailing edge wall, with the last $50D$ acting as a buffer region to eliminate acoustic wave reflections. The computational domain extends to $15D$ in the $y$-direction with the last $5D$ as a buffer region. The grid stretching ratio is 1.05 and 1.075 for the resolved and buffer regions, respectively, with a minimum element size of $0.2D$ inside the cavity. A total of $14,652$ hexagonal elements are used. The geometry and mesh of the three-dimensional cavity are shown in Figures 4.1 and 4.2, respectively. A periodic boundary condition is used in the

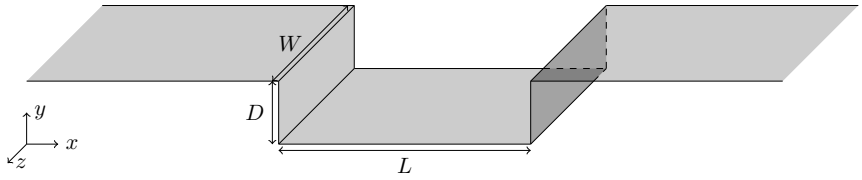


Figure 4.1. The geometry of the three-dimensional open deep cavity.

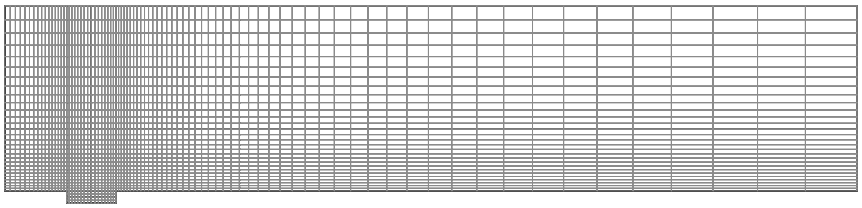

Figure 4.2. The mesh of the three-dimensional open deep cavity.

spanwise direction, no-slip boundary conditions are applied at the walls, and Riemann invariant boundary conditions are applied at the inlet and outlet of the computational domain. The second-order Nasab-Pereira-Vermeire [56] temporal scheme is used to advance the solution in time. The simulation is run for $100t_c$, where $t_c = D/U_\infty$, to allow initial transients to disappear and then run for another $400t_c$ to average statistical quantities. To ensure uncorrelated turbulent fluctuations at a separation of half the domain size, the correlation coefficient of the $x$-component of the velocity perturbation along with that of the pressure perturbation are computed along the spanwise direction and depicted in Figure 4.3. The results of the grid independency study are given in the next section.

#### 4.2.1.2 Results and Discussion

The grid independence study is performed by increasing the solution polynomial degree, which increases the resolution of the simulation. The time-averaged drag coefficient and the sound pressure level at an observer located $7.16D$ above the center of the cavity are computed using solution polynomial degrees of $\mathcal{P}2$, $\mathcal{P}3$, and $\mathcal{P}4$ to assess the grid independency.

The drag coefficient is defined as

$$C_D = \frac{F_x}{\frac{1}{2}\rho_\infty U_\infty^2 DW}, \tag{4.1}$$

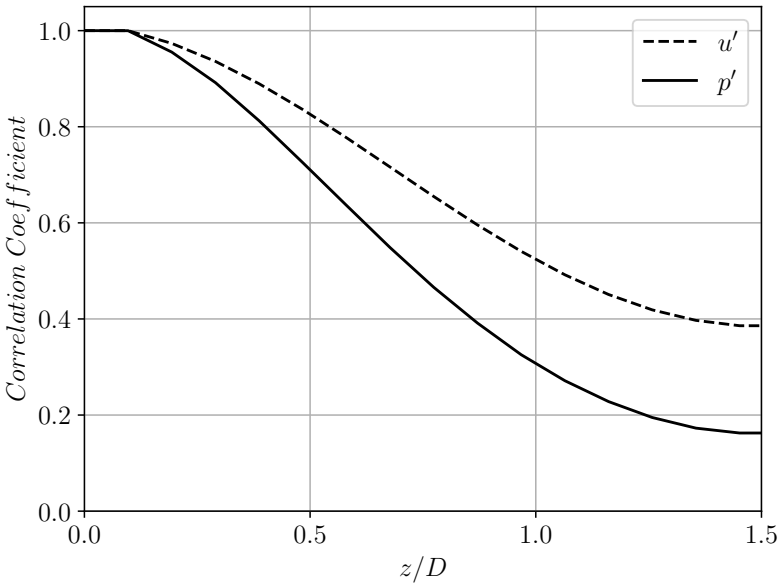


Figure 4.3. The correlation coefficient in the spanwise direction for the three-dimensional open deep cavity.

Table 4.1. A summary of grid independence study of the open deep cavity.

| Simulation | $\overline{C_D}$ | SPL |
|---|---|---|
| $\mathcal{P}2$ | 0.1314 | 112.12 |
| $\mathcal{P}3$ | 0.1098 | 113.13 |
| $\mathcal{P}4$ | 0.1115 | 113.34 |

where $F_x$ is the force in the $x$-direction computed on the three cavity walls, $\rho_\infty$ is the free-stream density, and $U_\infty$ is the free-stream velocity. The time-averaged drag coefficient along with the SPL at the observer, for different simulations, are given in Table 4.1, where 31 observer points along the span of the cavity are used. The time-averaged pressure and root-mean-squared of the pressure perturbation are computed for each observer point and then spatially averaged to find the SPL at the observer location. These results show that the $\mathcal{P}3$ simulation provides sufficient resolution for this study.


Figure 4.4. The design variable, $h_{TE}$, for the open deep cavity.

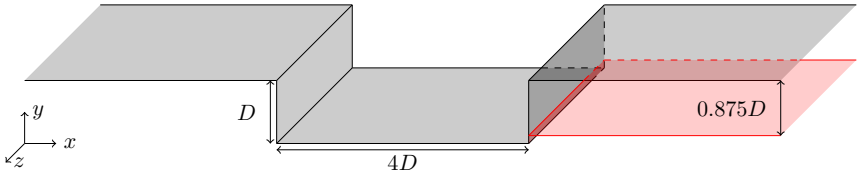


Figure 4.5. The baseline, in black, and optimum, in red, designs of the open cavity.

### 4.2.2 Optimization

In this section, the noise at the observer point located at $\boldsymbol{x}_{obs}/D = [2, 7.16]$ is minimized by changing the height of the cavity trailing edge wall, $h_{TE}$, depicted in Figure 4.4. Thus, $\boldsymbol{X} = h_{TE}$ is the design variable and $\boldsymbol{X}_0 = 0$, while the objective function is $\mathcal{F} = p'_{rms}$. Upper and lower bounds of $-1$ and 4, respectively, are chosen for the design variable, $h_{TE}$.

#### 4.2.2.1 Results and Discussion

The optimization procedure converged after 19 MADS iterations with a total of 36 objective function evaluations. The optimal design parameter is identified as $h_{TE} = -0.875$, resulting in an SPL of 100.3 $dB$, a 12.9 $dB$ reduction in noise. The baseline and optimum designs are depicted in Figure 4.5. Moreover, Figure 4.6 illustrates the explored design parameter space and convergence of the objective function.

The Q-criterion contours coloured by velocity magnitude and the pressure perturbation of both the baseline and optimum designs are shown in Figures 4.7 and 4.8, respectively. Comparing these figures, turbulent structures over the cavity are reduced significantly in the optimum design, and

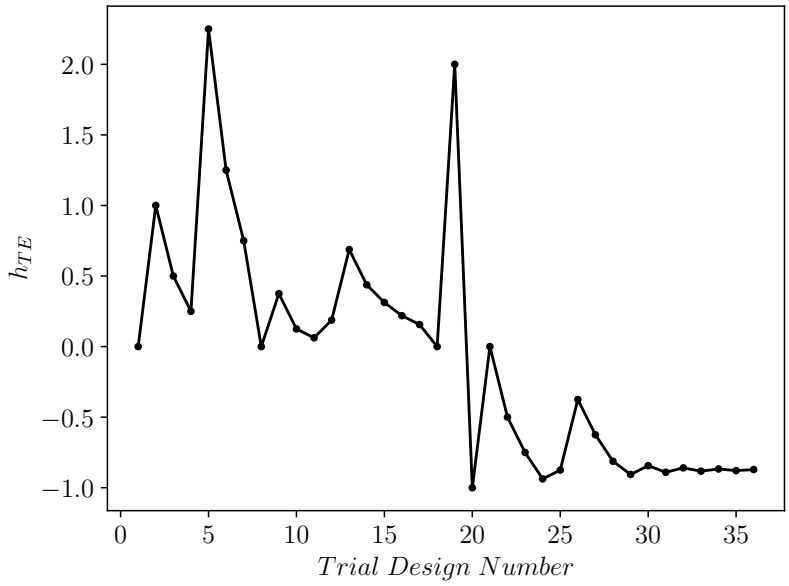


(a) The design space.

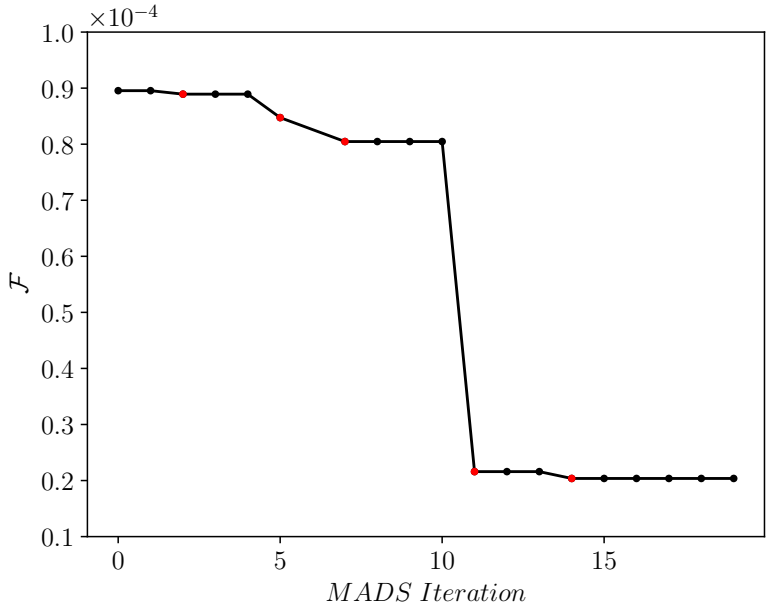


(b) The objective function convergence with the new incumbent designs highlighted in red.

Figure 4.6. The design space and objective function convergence for the three-dimensional open deep cavity.

the shear layer expands over the cavity, resulting in much lower noise emission. Furthermore, the Power Spectral Density (PSD) of the sound pressure level is plotted against the Strouhal number for both the baseline and optimum designs in Figure 4.9, which follows the Welch's method of periodiograms [179] and involves dividing the time period into 6 windows with a 50% overlap. This figure illustrates the SPL reduction across all frequency ranges.

## 4.3 Tandem Cylinders

In this section, a tandem arrangement of two cylinders is considered, as shown in Figure 4.10, which is a simplified model of flow over landing gears. The three-dimensional wake development of a single cylinder was studied by Williamson [180]. Additionally, Papaioannou et al. [181] investigated the three-dimensionality effects of flow over two tandem cylinders, varying Reynolds number and the spacing distance between the cylinders. They found that as Reynolds number increased, two-dimensional results diverged from three-dimensional ones, especially beyond a critical Reynolds number where wake three-dimensionality initiated. The Reynolds number of our study, based on the upstream cylinder's diameter, is $Re_D = 1000$ since the wake will develop considerable three-dimensionality and this Reynolds number is associated with the early turbulent regime [181].

### 4.3.1 Validation

In this section, the simulation of flow over two tandem cylinders is validated using reference DNS data [181], along with a grid independence study of the time-averaged lift and drag coefficients and SPL at a near-field observer located $2D$ above the upstream cylinder. Then, the optimization is performed similar to Section 3.3, where sound at the near-field observer is minimized. The design variables are the ratio of the cylinders' diameters, $r$, and the distance between the two, $s$.

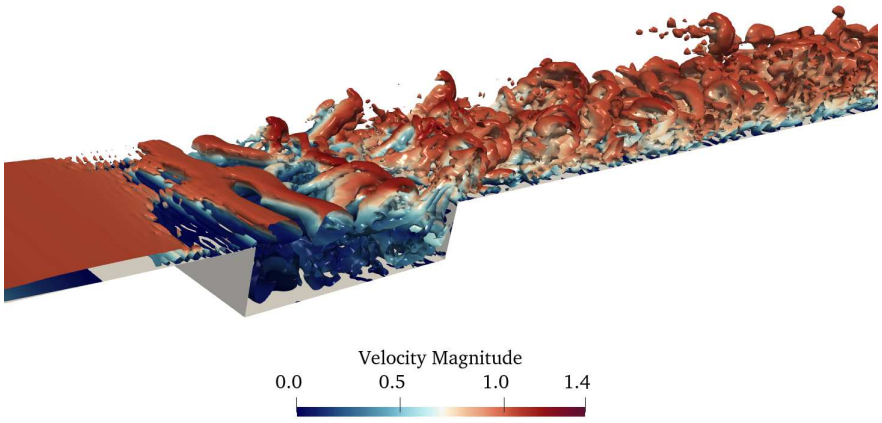


(a) Q-criterion contours coloured by velocity magnitude.

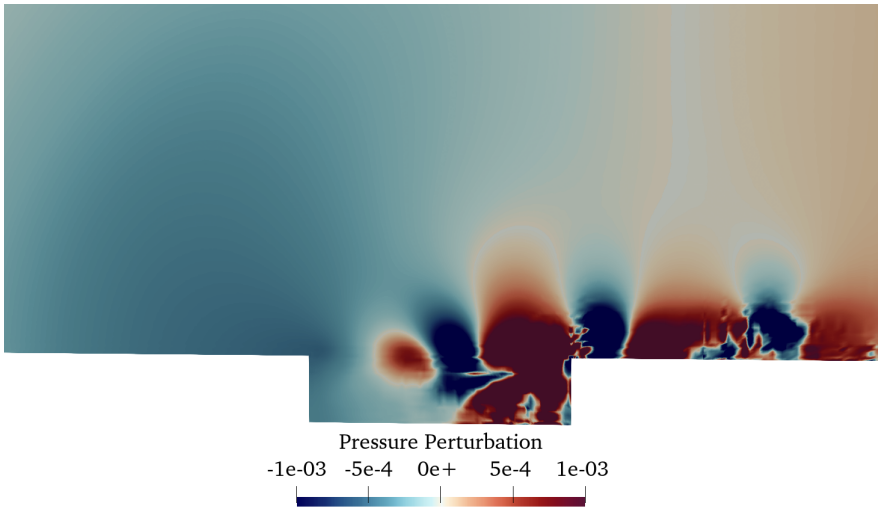


(b) Pressure perturbation.

Figure 4.7. The Q-criterion contours and pressure perturbation for the baseline design of the open deep cavity.

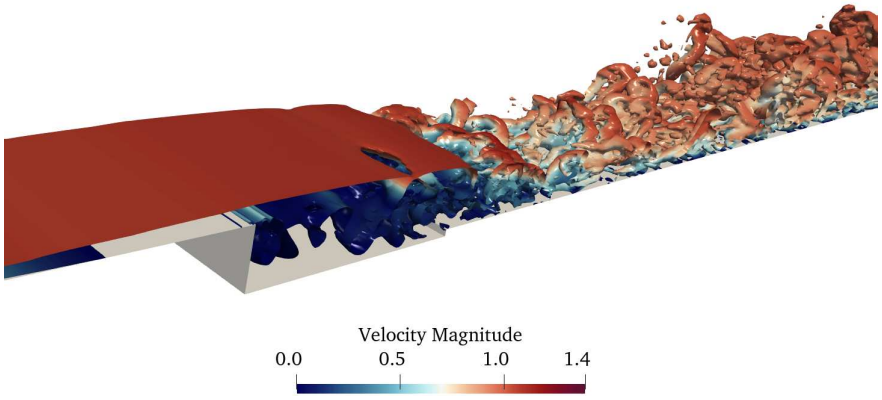


(a) Q-criterion contours coloured by velocity magnitude.

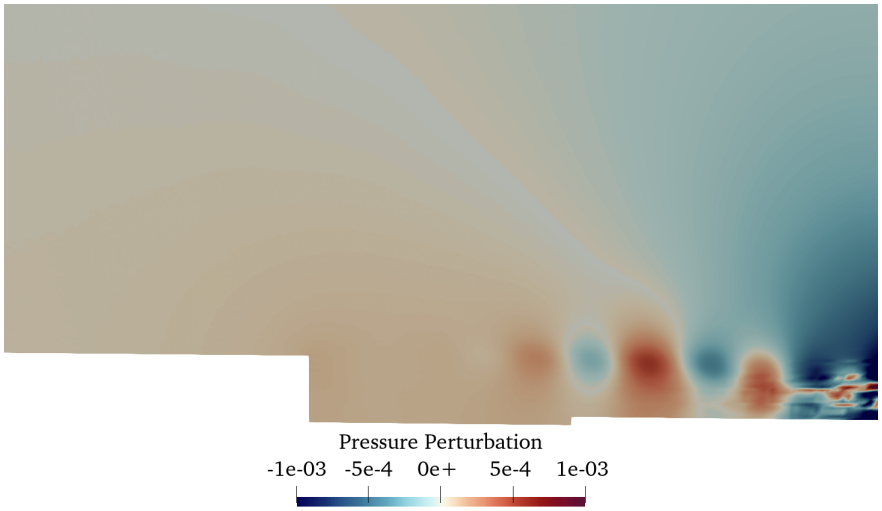


(b) Pressure perturbation.

Figure 4.8. The Q-criterion contours and pressure perturbation for the optimum design of the open deep cavity.

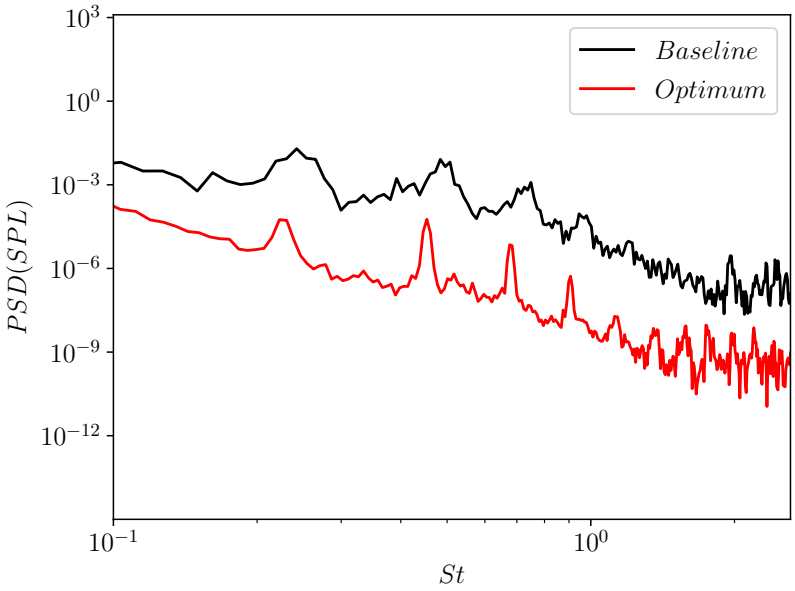


Figure 4.9. The sound spectra for the open deep cavity.

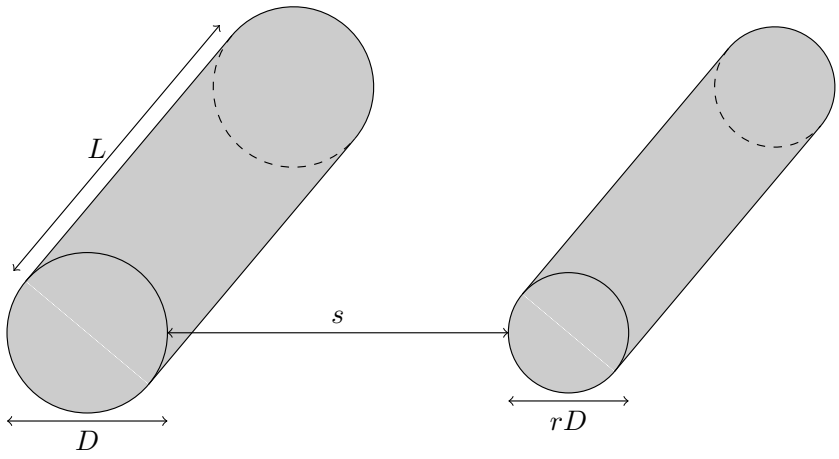


Figure 4.10. The geometry of two cylinders in a tandem configuration.

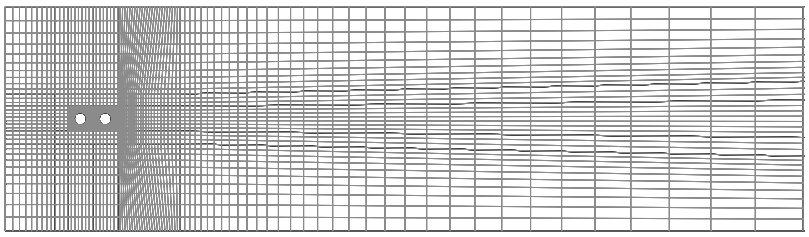

Figure 4.11. The mesh of the two cylinders in a tandem configuration.

#### 4.3.1.1 Computational Details

The cylinders are located at a distance of $s/D = 1$ with a ratio of $r = 1$ and have a spanwise length of $L/D = 10$, following previous studies [181]. The Reynolds number, based on the upstream cylinder's diameter, is $Re_D = 1000$, corresponding to the early turbulent regimes [181], and the Mach number is 0.2. The boundary layer region extends to $0.5D$ around the cylinders, with the inlet boundary placed $5D$ away from the upstream cylinder and the outlet boundary $55D$ away from the downstream cylinder. The computational domain is extended to $10D$ in the $y$ direction. The stretching ratio for the first $5D$ and $1D$ elements in the $x$ and $y$-directions, respectively, is 1.05, and that of the remaining elements is 1.075. The smallest element size in the domain is $0.1D$, which is in the boundary layer region. A total number of $31,780$ hexagonal elements are used. The mesh of the tandem cylinders is shown in Figure 4.11. Periodic boundary conditions are applied in the spanwise direction, while a no-slip boundary condition is imposed on the surface of the cylinders, along with Riemann invariant boundary conditions at the inlet and outlet of the computational domain. The Nasab-Pereira-Vermeire temporal scheme of second-order [56] is employed to advance the simulation in time. The simulation is run for $100t_c$, where $t_c = D/U_\infty$, to allow initial transients to disappear, followed by a subsequent period of 500 $t_c$ to obtain an average of the statistical quantities.

#### 4.3.1.2 Results and Discussion

The sufficiency of the spanwise length is investigated by computing the correlation coefficient of the velocity fluctuation and the pressure perturbation along the $z$-direction. The correlation plot,

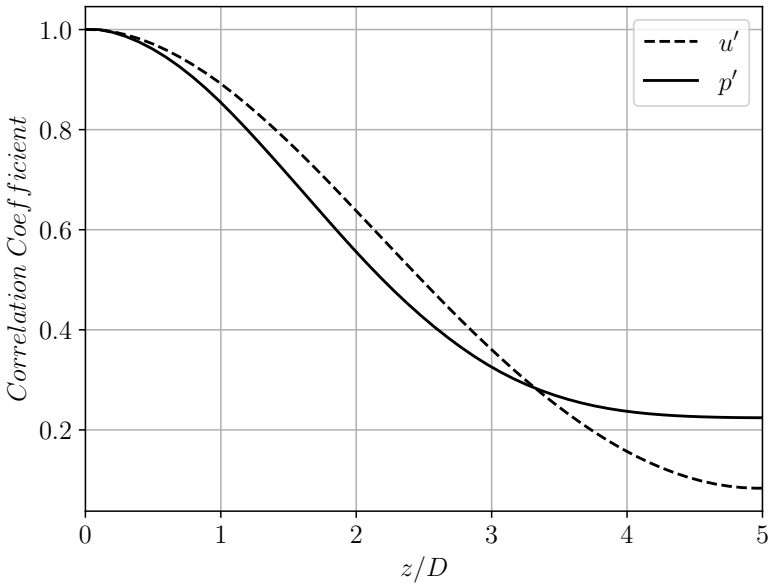


Figure 4.12. The correlation coefficient in the spanwise direction for the tandem cylinders.

Table 4.2. The $\overline{C_{D1}}$ and $SPL$ at the observer, for the tandem cylinders configuration using different lengths of the averaging window.

| Averaging Window Size | $\overline{C_{D1}}$ | | $SPL$ | |
|---|---|---|---|---|
| | $\mathcal{P}2$ | $\mathcal{P}3$ | $\mathcal{P}2$ | $\mathcal{P}3$ |
| $200t_c$ | 0.962374 | 0.994465 | 126.49 | 125.14 |
| $300t_c$ | 0.963871 | 0.994915 | 126.87 | 125.23 |
| $400t_c$ | 0.965569 | 0.996092 | 127.34 | 125.25 |
| $500t_c$ | 0.966651 | 0.996752 | 127.56 | 125.25 |
| $600t_c$ | 0.967519 | 0.997042 | 127.73 | 125.31 |
| $700t_c$ | 0.968142 | 0.996965 | 127.84 | 125.31 |

demonstrated in Figure 4.12, ensures the uncorrelated fluctuations in the $z$-direction at a separation of half of the domain size. Furthermore, the time-averaged drag coefficient and the sound pressure level at the observer are computed using different averaging window lengths, summarized in Table 4.2. The time-averaged drag coefficient of the upstream cylinder is computed using $\mathcal{P}2$ and $\mathcal{P}3$ simulations. The $\overline{C_{D1}}$ obtained using the $\mathcal{P}3$ simulation is 0.997, which is in good agreement with the reference value of 0.988 [181]. Table 4.2 shows that the difference in the statistical time-averaged quantities is negligible beyond $500t_c$. Thus, in this study, the statistical quantities are averaged for $500t_c$.

### 4.3.2 Optimization

The distance between the two cylinders, $s$, and the ratio between the diameters of the cylinders, $r$, are the design variables, $\boldsymbol{X} = [s, r]$. The objective function is $\mathcal{F} = p'_{rms}$ at $2D$ above the upstream cylinder.

#### 4.3.2.1 Results and Discussion

The optimization problems converges after 18 MADS iterations, including 48 objective function evaluations. The baseline and optimum designs are shown in Figure 4.13. The design space and objective function convergence are shown in Figure 4.14, where the optimum design is found as $(s, r) = (2.0291D, 1.7563D)$. The optimization procedure has covered a wide range of design variables, as shown in Figure 4.14a. Q-criterion contours coloured by velocity magnitude and acoustic field at the mid-plane are shown for the baseline design and the optimum design, in Figures 4.15 and 4.16, respectively. The optimized design exhibits a smoother flow field qualitatively, with the elimination of the wake region behind the upstream cylinder. The distance between the cylinders and their diameter ratios facilitate a smooth transition of flow from the upstream to the downstream cylinder. This reduction in turbulent structures between the cylinders and the smooth flow transition yields a noise reduction exceeding 11 $dB$. The sound pressure level of the initial design at the observer, $2D$ above the upstream cylinder, is 125.3 $dB$, which reduces to 114.1 $dB$ for the optimized configuration. Lastly, Figure 4.17 presents the PSD of SPL versus Strouhal number, computed using Welch's method of periodograms [179] with 3 windows and a 50% overlap. It is evident that the optimum design displays higher intensity PSD of SPL over a broad frequency range, while achieving a lower SPL value. This behavior can be attributed to the baseline design producing high-intensity sound at specific frequencies ($St = 0.63, 0.77$, and $0.90$), contributing to its elevated peak SPL, whereas the optimum design distributes its energy across a wider frequency spectrum.

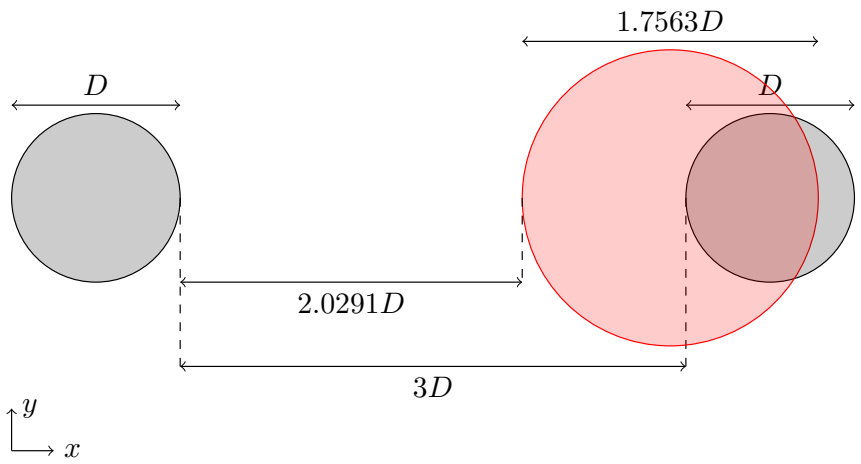


Figure 4.13. The baseline, in black, and optimum, in red, designs of the tandem cylinders.

## 4.4 NACA 4-Digit Airfoil

The flow over NACA 4-digit airfoils is investigated in this section. The procedure is similar to that of Section 3.4, with the computational domain extruded in the $z$-direction. The validation of the flow simulation is conducted using an ILES reference [182] and a grid independence study for a NACA0012 airfoil. Subsequently, four design parameters, akin to those in Section 3.4, are selected, and the gradient-free MADS optimization technique is employed. We implemented a parallel optimization framework, where all objective function evaluations at each iteration is performed concurrently. Consequently, within this parallel optimization framework, the computational cost of each optimization iteration remains unaffected by the number of design variables, provided adequate resources are available. Therefore, the maximal positive basis construction is employed for the MADS algorithm in this context, as the number of objective function evaluations needed at each MADS iteration is immaterial due to the ample availability of resources.

### 4.4.1 Validation

In this section, we conduct validation for the flow over a NACA0012 airfoil at an angle of attack of 6°. The validation process involves comparing the time-averaged lift and drag coefficients obtained from two distinct grid resolutions with those from an ILES reference [182]. Moreover, the

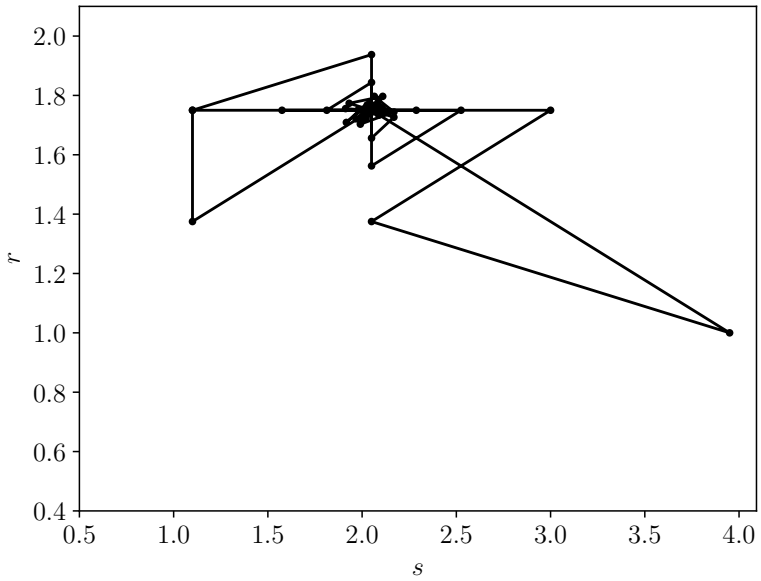


(a) The design space.

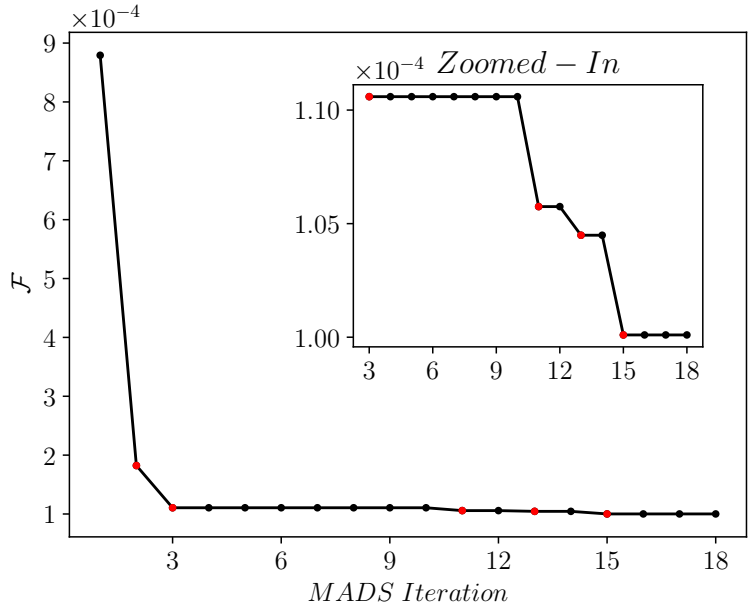


(b) The objective function convergence with the new incumbent designs highlighted in red.

Figure 4.14. The design space and objective function convergence for the tandem cylinders.

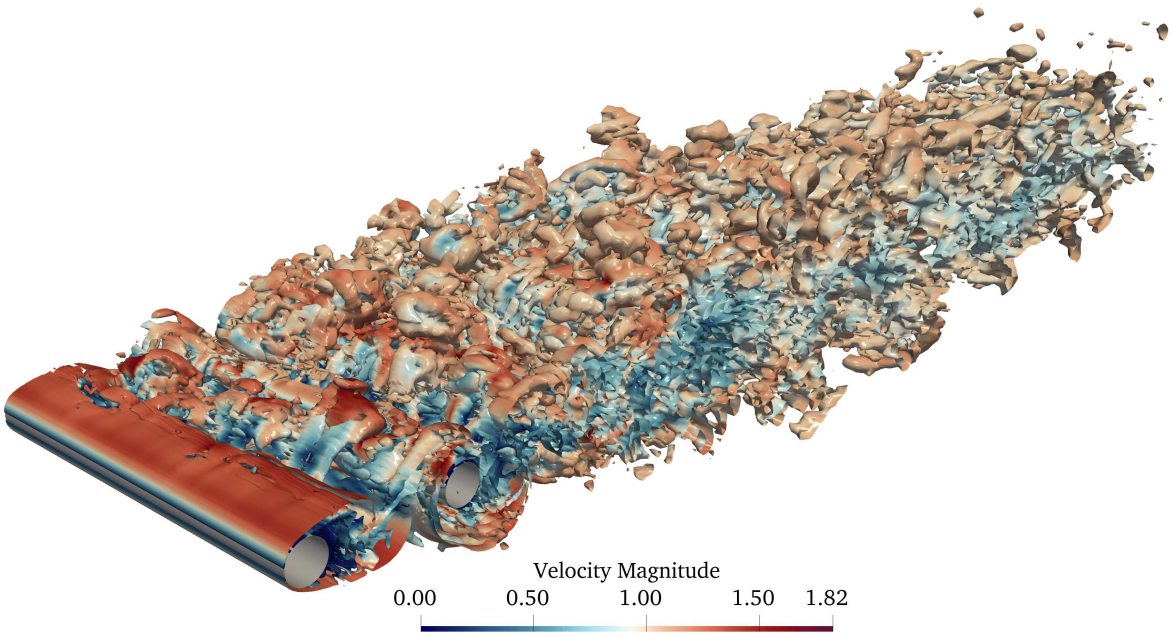


(a) Q-criterion coloured by velocity magnitude.

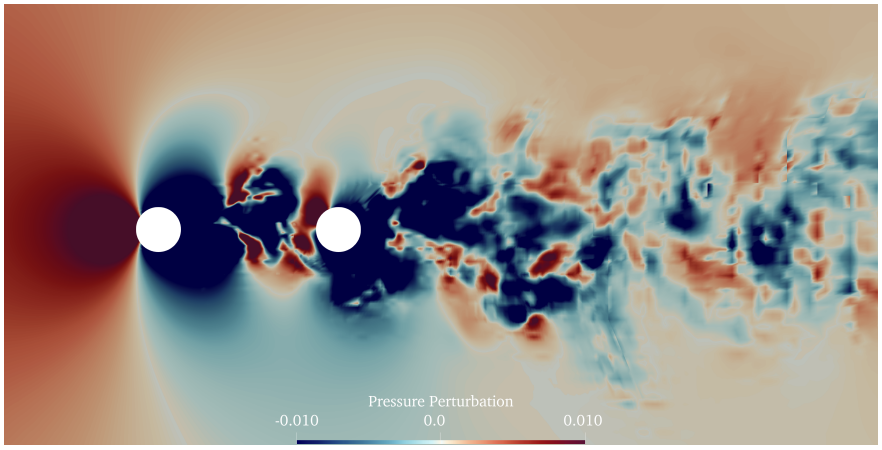


(b) Acoustic pressure field at mid-plane.

Figure 4.15. The baseline tandem cylinder design at $t_c = 600$.

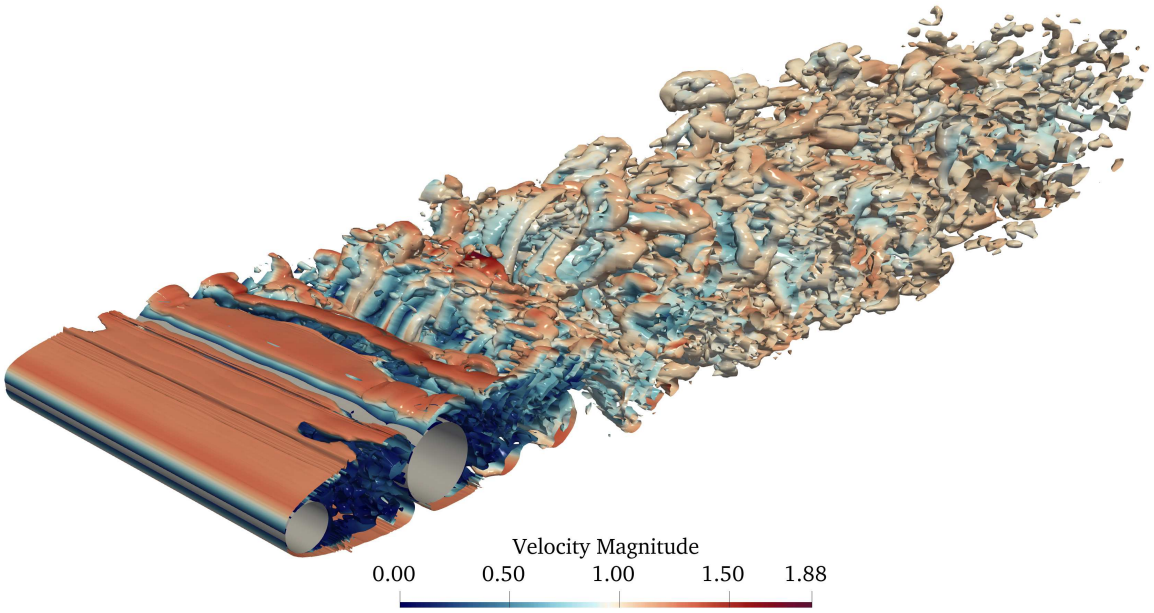


(a) Q-criterion coloured by velocity magnitude.

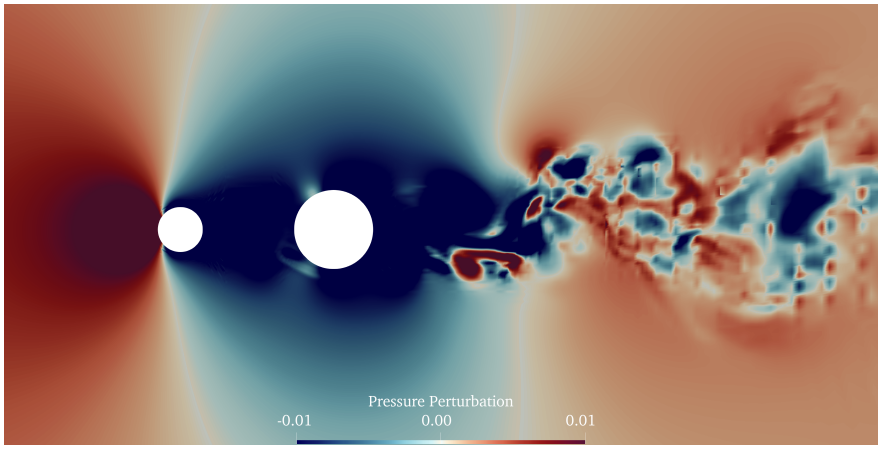


(b) Acoustic pressure field at mid-plane.

Figure 4.16. The optimum tandem cylinder design at $t_c$ = 600.

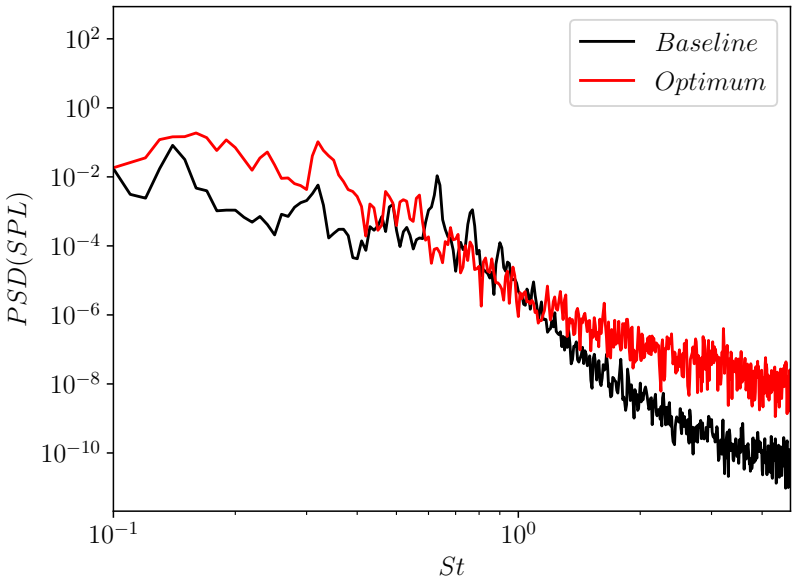


Figure 4.17. The sound spectra for the tandem cylinders.

SPL at a near-field observer is computed using both grid resolutions and various time averaging window lengths. This analysis ensures the independence of the results to both grid resolution and time averaging window length. Detailed computational procedures and validation results are presented in the subsequent sections.

#### 4.4.1.1 Computational Details

The computational grid consists of 121, 520 hexagonal elements, illustrated in Figure 4.18. The domain extends to $20c$ in the $x$-direction, $10c$ in the $y$-direction, and $0.2c$ in the $z$-direction, with $c = 1$ representing the airfoil chord. Notably, elements in the wake region are inclined at the angle of attack to accurately capture trailing-edge vortices. The flow conditions are characterized by a Reynolds number of 23, 000, a free-stream Mach number of $M = 0.2$, and a Prandtl number of $Pr = 0.71$. The simulation is run for 10 convective times to allow the initial transition disappears and then run for another 90 convective times for flow statistics averaging. The second-order Nasab-Pereira-Vermeire [56] temporal scheme is used to advance the solution in time. Additionally, a variable solution polynomial degree is implemented to eliminate acoustic wave reflections from

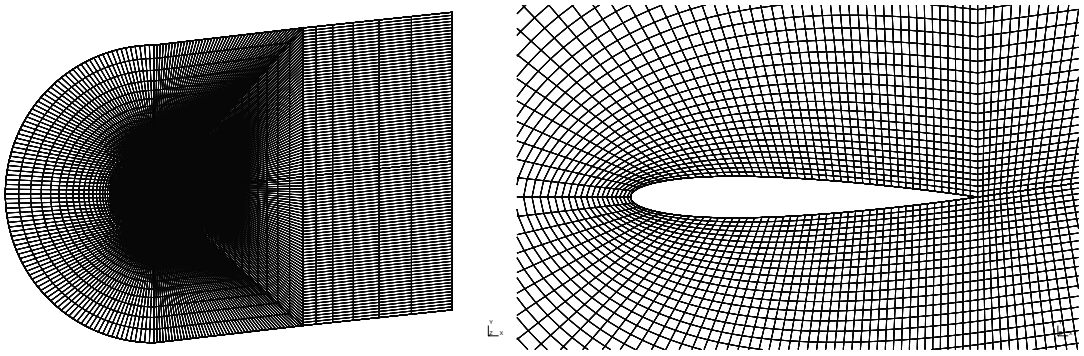

(a) The computational domain. (b) The vicinity of the airfoil.

Figure 4.18. The computational grid for NACA0012 airfoil at $\alpha = 6°$.

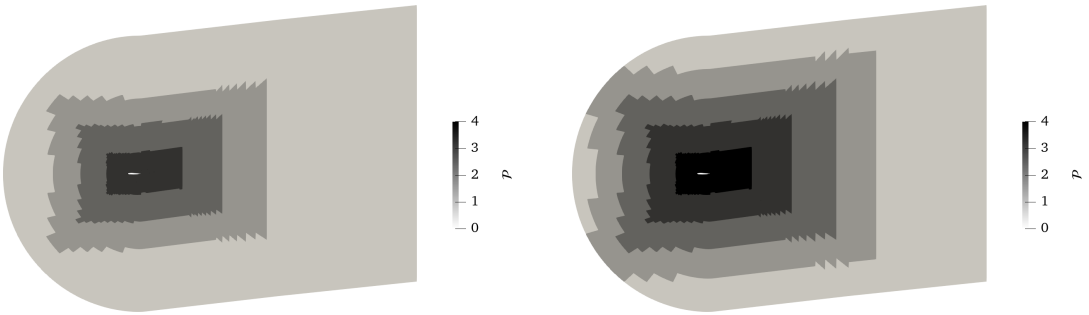


(a) Low resolution, $\mathcal{P}0 - \mathcal{P}3$. (b) High resolution, $\mathcal{P}0 - \mathcal{P}4$.

Figure 4.19. Different solution polynomial distributions for grid independence study of NACA0012 airfoil at $\alpha = 6°$.

boundaries, as demonstrated in Figure 4.19.

#### 4.4.1.2 Results and Discussions

Two grid resolutions are employed with maximum solution polynomial degrees of $\mathcal{P}3$ and $\mathcal{P}4$. The time-averaged lift and drag coefficients are compared to the ILES reference data [182], presented in Table 4.3. The difference between the time-averaged lift coefficient obtained from the $\mathcal{P}4$ simulation and the reference data is negligible, affirming adequacy of the $\mathcal{P}4$ simulation's grid resolution. Furthermore, the time-averaged drag coefficient differs by less than 1.3% from the reference data. The SPL at an observer located two unit chord lengths below the trailing edge is computed for both $\mathcal{P}3$ and $\mathcal{P}4$ simulations. Various averaging window lengths are applied, and the results are summarized in Table 4.4. Considering the findings presented in Tables 4.3 and 4.4,

Table 4.3. The time-averaged lift and drag coefficients of the NACA0012 airfoil at $\alpha = 6°$.

| | $\mathcal{P}0 - \mathcal{P}3$ | $\mathcal{P}0 - \mathcal{P}4$ | reference [182] |
|---|---|---|---|
| $\overline{C_L}$ | 0.6534 | 0.6399 | 0.6402 |
| $\overline{C_D}$ | 0.0553 | 0.0548 | 0.0541 |

Table 4.4. The grid independence study of SPL using different averaging window lengths for NACA0012 airfoil at $\alpha = 6°$.

| Averaging Window Length | SPL in $dB$ | |
|---|---|---|
| | $\mathcal{P}0 - \mathcal{P}3$ | $\mathcal{P}0 - \mathcal{P}4$ |
| $20t_c$ | 114.9 | 116.3 |
| $40t_c$ | 115.7 | 116.3 |
| $60t_c$ | 115.7 | 116.2 |
| $80t_c$ | 115.7 | 116.2 |

we opt to conduct $\mathcal{P}4$ simulations for a total duration of 70 convective times for the optimization study.

### 4.4.2 Optimization

There are four design parameters similar to Section 3.4.2, i.e. $\boldsymbol{\chi} = [c^a_{max}, x_{c^a_{max}}, t^a_{max}, \alpha]$. The maximum camber range is set to $c^a_{max} \in [-10, 10]$ as a percentage of the chord, with the distance from the airfoil leading edge in the range of $x_{c^a_{max}} \in [4, 9]$ as a tenth of the chord. The maximum thickness of the airfoil is within the range of $t^a_{max} \in [6, 18]$ as a percentage of the chord. Finally, the angle of attack varies from 0° to 12°. The objective function is defined as the sound pressure level at the observer with constraints on both the mean lift and mean drag coefficients. A quadratic penalty term is added to the objective function when the lift coefficient deviates from the baseline design, and an additional quadratic penalty term is added when the mean drag coefficient is above the baseline design. The objective function is defined as

$$\mathcal{F} = \begin{cases} SPL + \epsilon_1 \left(\overline{C_L} - \overline{C_{L,baseline}}\right)^2 + \epsilon_2 \left(\overline{C_D} - \overline{C_{D,baseline}}\right)^2 & \overline{C_D} > \overline{C_{D,baseline}} \\ SPL + \epsilon_1 \left(\overline{C_L} - \overline{C_{L,baseline}}\right)^2 & \overline{C_D} \leq \overline{C_{D,baseline}} \end{cases}, \tag{4.2}$$

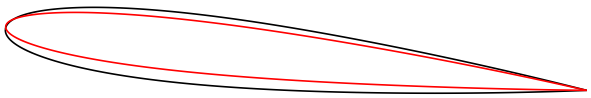

Figure 4.20. The baseline, in black, and optimum, in red, designs of the NACA 4-digits airfoil.

where the constants $\epsilon_1$ and $\epsilon_2$ are set to $8,000$ and $400,000$, respectively, to compensate for the order of magnitude difference in $SPL$ and $\overline{C_L}$ and $\overline{C_D}$. The defined objective function minimizes the sound pressure level while maintaining the mean lift coefficient, and ensures the optimized airfoil has a similar or lower mean drag coefficient.

#### 4.4.2.1 Results and Discussion

This optimization procedure converges after 22 MADS iterations, consisting of 172 objective function evaluations. The baseline and optimum designs are shown in Figure 4.20. The design space and the convergence of the objective function are shown in Figure 4.21. The optimal airfoil design has a maximum camber of $c^a_{max} = 0.1406$ at 6.5 tenths of the chord distance from the leading edge, with a thickness of $t^a_{max} = 8.86$ percent of the chord, at an angle of attack of $\alpha = 6.28$ degrees. The SPL of the optimized airfoil is decreased to 110.6 $dB$, the mean lift coefficient is $\overline{C_L} = 0.6556$, and finally, the mean drag coefficient is decreased by 7.4% to $\overline{C_D} = 0.0509$.

The Q-criterion coloured by velocity magnitude and the pressure perturbation at mid-planes are shown in Figures 4.22 and 4.23 for the baseline and optimum designs, respectively. The optimum design shifts the separation point closer to the leading edge, indicating reduced flow energy upon separation from the airfoil. This, in turn, yields smaller turbulence structures and reduced acoustic energy. Consequently, there is a notable decrease in the pressure perturbation field, translating to a noise reduction of approximately 5.7 $dB$. Figure 4.24 presents the PSD of SPL as a function of the Strouhal number, computed using Welch's method of periodograms [179] with 3 windows and a 50% overlap. It is evident that the optimum design displays lower-intensity SPL energy across various frequency ranges.

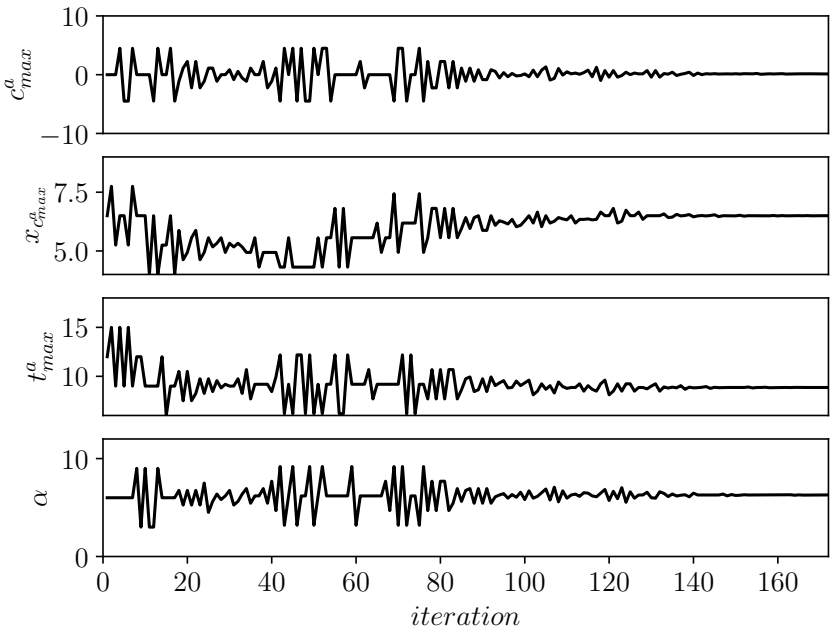


(a) The design space.

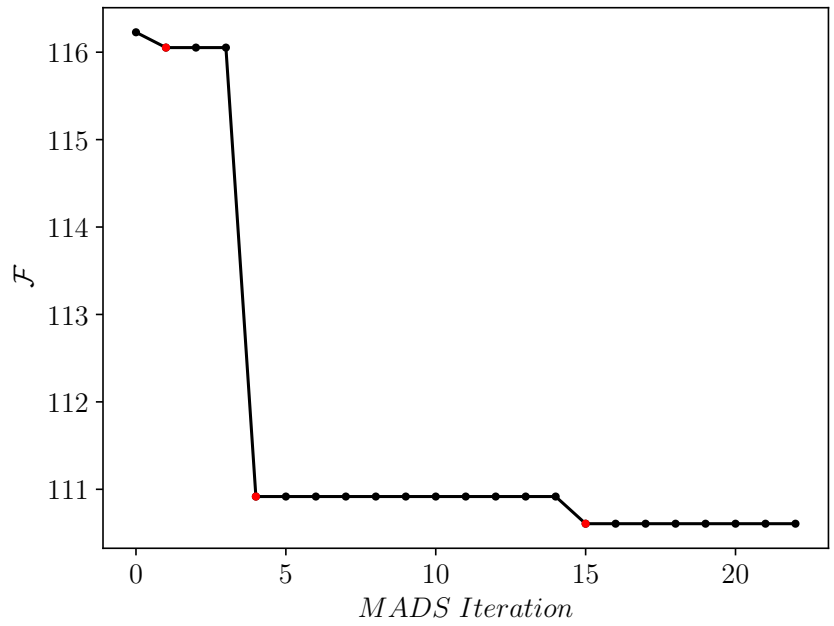


(b) The objective function convergence with the new incumbent design highlighted in red.

Figure 4.21. The design space and objective function convergence of the NACA 4-digit airfoil optimization.

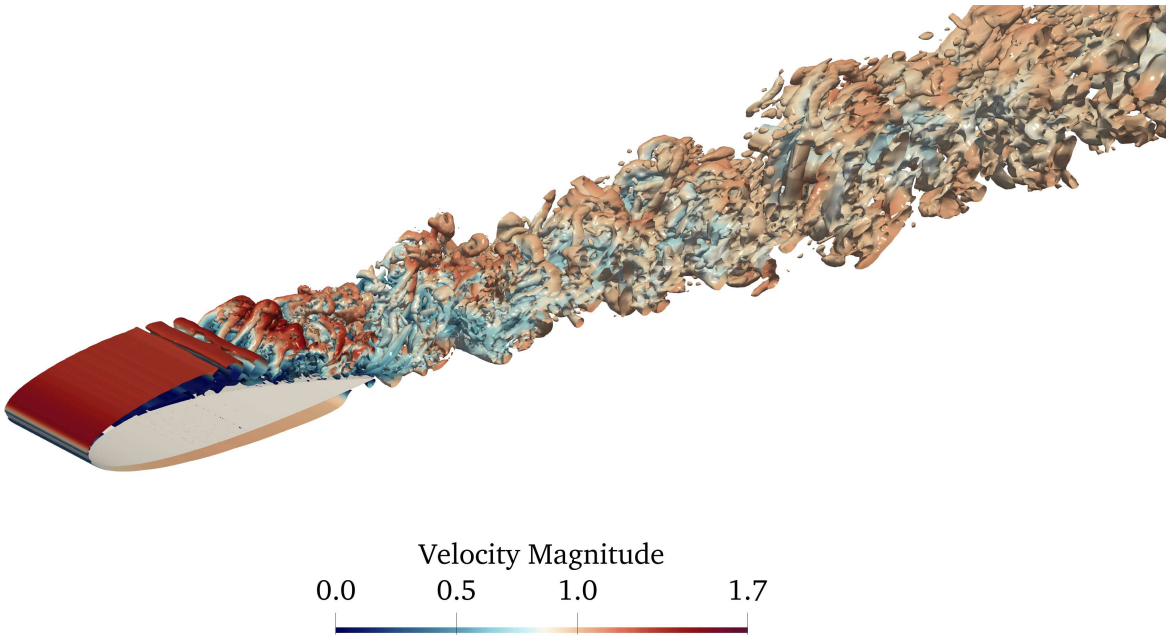


(a) Q-criterion coloured by velocity magnitude.

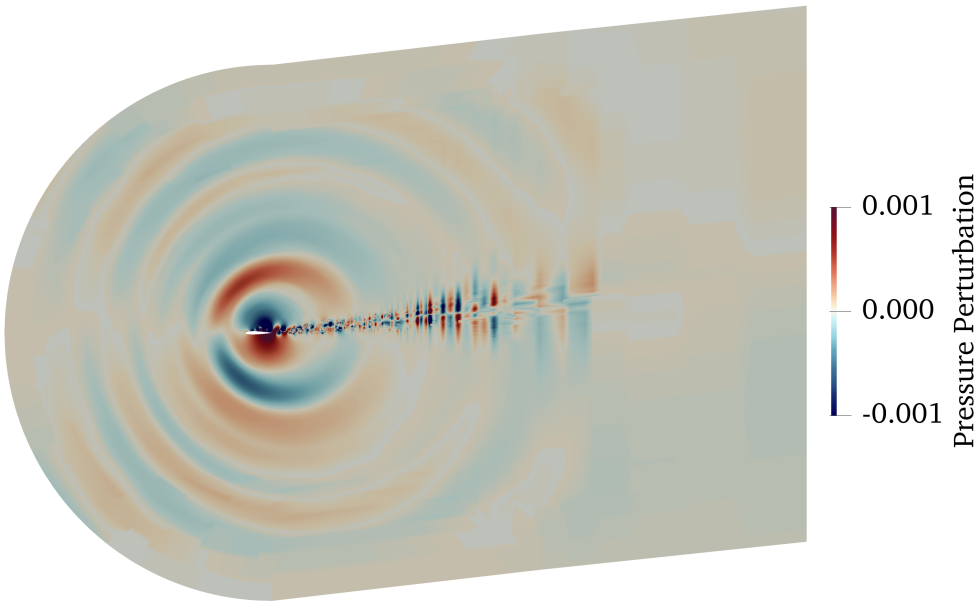


(b) Acoustic pressure field at mid-plane.

Figure 4.22. The baseline airfoil at $t_c = 70$.

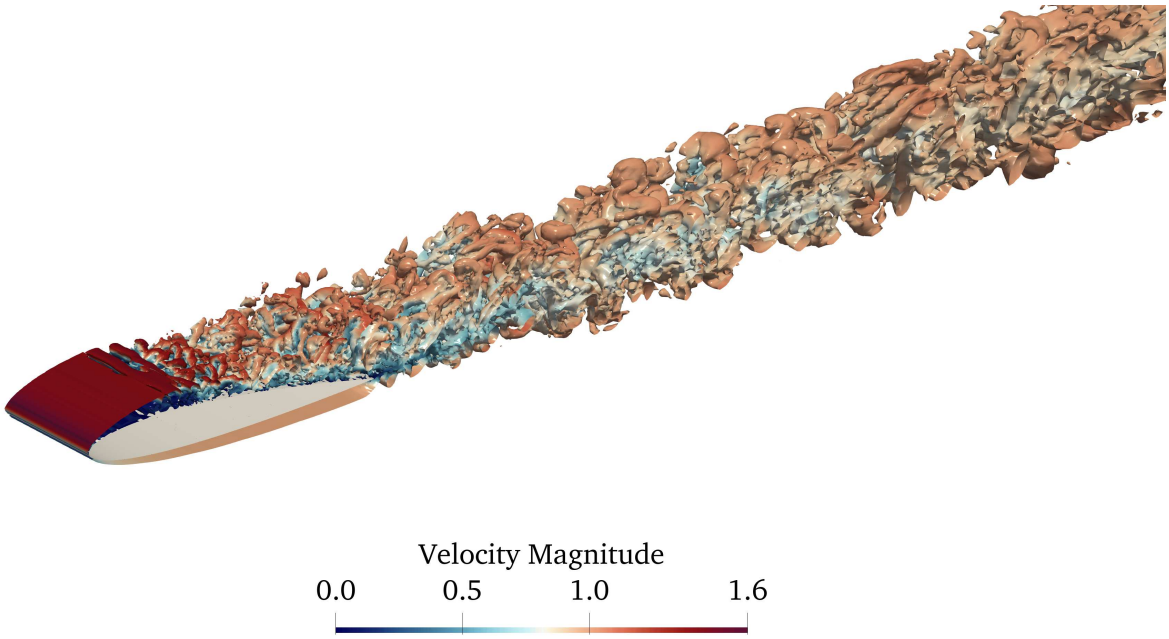


(a) Q-criterion coloured by velocity magnitude.

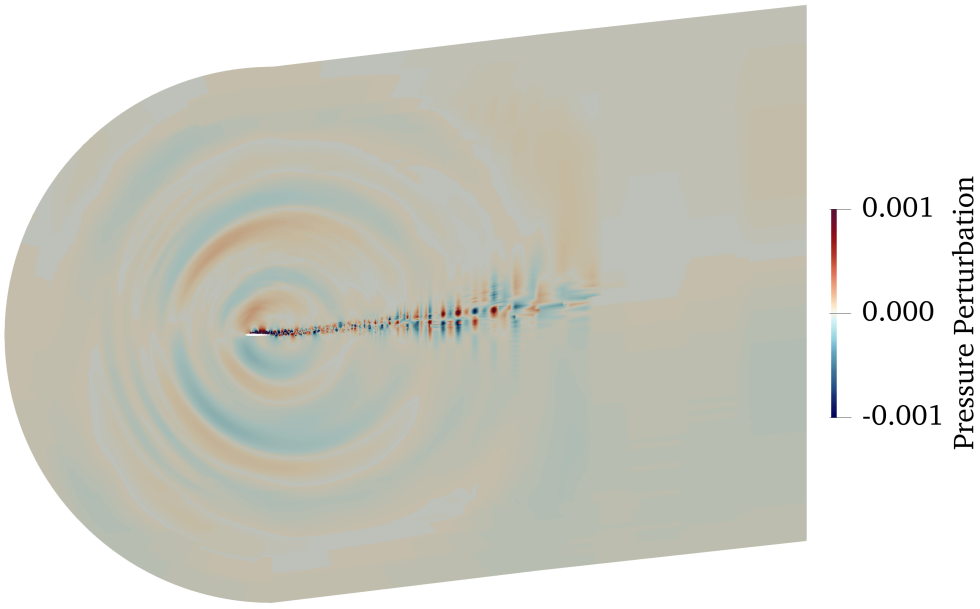


(b) Acoustic pressure field at mid-plane.

Figure 4.23. The optimum airfoil at $t_c$ = 70.

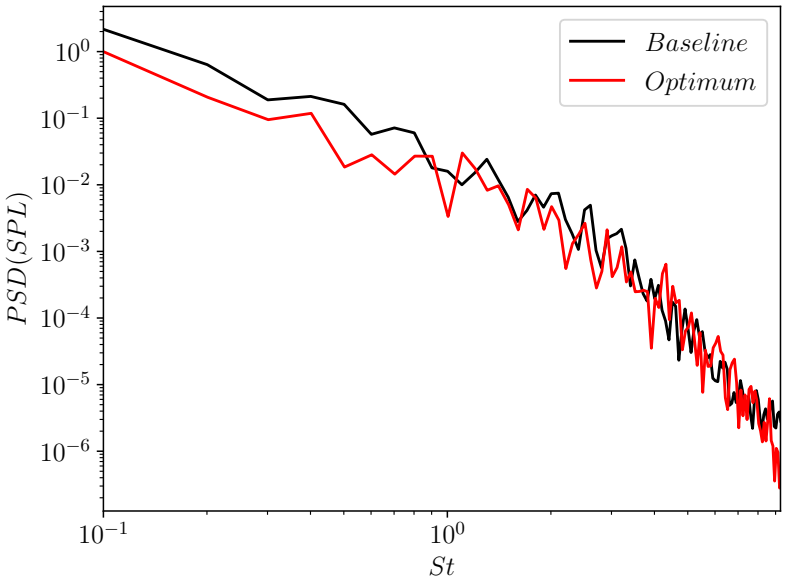


Figure 4.24. The sound spectra for the NACA 4-digit airfoils.

# Chapter 5

# Far-Field Aeroacoustics via Ffowcs-Williams and Hawkings Formulation

## 5.1 Formulation

The FW-H equation is an exact rearrangement of the continuity and Navier-Stokes equations, resulting in an inhomogeneous wave equation with source terms. These source terms consist of two surface source terms, monopole and dipole, and a volume source term, quadrupole. The computational resources required for the volume integration of the quadrupole source term are significantly higher than those for surface integration. However, the contribution of the quadrupole source term is negligible for many subsonic applications [183]. Three different categories exist of aeroacoustics problems:

1. *Fixed Observer*. A fixed observer in a stationary ambient medium and the source can be either in motion or rest,

2. *Moving Observer*. A moving observer in a stationary ambient medium and the source is in motion,

3. *Moving Medium*. A fixed observer in a moving medium, the source can be either in motion or rest.

There are several solutions to the FW-H equations. The well-known formulations 1 and 1A of Farassat [184, 185] assume the propagation of sound waves in a medium at rest. Najafi-Yazdi et al. [186] and Ghorbaniasl et al. [187] introduced a new formulation based on the convective wave equation. These formulations are well-suited for CFD simulations, accounting for the presence of a moving medium. In this thesis, the time-domain moving medium formulation is implemented, following the Ghorbaniasl formulation [187].

First, a data surface is defined in space to contain all the noise sources around the body by a function $f(\boldsymbol{x}, t)$, as

$$f(\boldsymbol{x},t)\begin{cases} < 0 & \text{inside the boundary,} \\ = 0 & \text{on the boundary,} \\ > 0 & \text{outside the boundary,} \end{cases} \tag{5.1}$$

and it is assumed that

$$|\boldsymbol{\nabla} f| = 1, \tag{5.2}$$

and $f$ is smooth, without discontinuities, so that

$$\frac{\partial f}{\partial x_i} = \hat{\mathbf{n}}_i \tag{5.3}$$

is the local outer normal of the data surface.

The initial step in the derivation of the FW-H equation involves multiplying the Heaviside function by the conservation of mass and momentum equations. This operation confines the application of these equations exclusively to regions outside the data surface. Subsequently, employing the principles of generalized function theory, these equations are transformed into non-homogeneous

wave equations, as detailed in [188]. Thus, the conservation of mass will be

$$\frac{D}{Dt}\left[(\rho-\rho_0)\,H(f)\right]+\frac{\partial}{\partial x_i}\left[\rho u_i H(f)\right]=Q\delta(f), \tag{5.4}$$

$$Q=\rho\left(u_n+U_{\infty n}-v_n\right)+\rho_0\left(v_n-U_{\infty n}\right), \tag{5.5}$$

where $\rho$ is the density of the fluid, $\rho_0$ denotes the fluid density at rest, $H(f)$ is the Heaviside function, $u_i$ are the velocity components, $Q$ is the source term for the continuity equation known as the thickness term and accounts for the flux of mass across the surface, and $\delta(f)$ is the Dirac's delta function of $f(\boldsymbol{x},t)$. Finally, the subscript $n$ denotes the local normal term of the data surface. Thus, $u_n=u_i\hat{n}_i$, $U_{\infty n}=U_{\infty i}\hat{n}_i$, and $v_n=v_i\hat{n}_i$. $U_{\infty i}$ being the $i^{th}$ component of the mean flow velocity and $v_i$ being the $i^{th}$ component of the data surface velocity. Note that Equation 5.4 returns zero inside the data surface and the value of density fluctuation outside the data surface.

Applying the same methodology, the non-linear momentum equation yields the following

$$\frac{D}{Dt}\left[\rho u_i H(f)\right]+\frac{\partial}{\partial x_j}\left[\rho u_i u_j H(f)\right]+\frac{\partial}{\partial x_j}\left[\left(p\delta_{ij}-\sigma_{ij}\right)H(f)\right]=L_i\delta(f), \tag{5.6}$$

$$L_i=P_{ij}\hat{n}_j+\rho u_i\left(u_n+U_{\infty n}-v_n\right), \tag{5.7}$$

$$P_{ij}=\left(p-p_0\right)\delta_{ij}-\sigma_{ij}, \tag{5.8}$$

where $p$ is the static pressure, $\sigma_{ij}$ is the viscous stress tensor, $L_i$ is the source term for the non-linear momentum equation known as the loading term and accounts for the flux of momentum across the surface, and $P_{ij}$ is the compressive stress tensor.

The equation for propagation of noise is obtained via taking the time derivative of Equation 5.4 and subtracting the divergence of Equation 5.6, and is

$$\left(\frac{1}{c_0^2}\frac{D^2}{Dt^2}-\nabla^2\right)\left(p'\left(\boldsymbol{x},t\right)H(f)\right)=\frac{D}{Dt}\left(Q\delta(f)\right)-\frac{\partial}{\partial x_i}\left(L_i\delta(f)\right)+\frac{\partial^2}{\partial x_i\partial x_j}\left(T_{ij}H(f)\right), \tag{5.9}$$

where

$$Q = \rho\left[u_n - (v_n - U_{\infty n})\right] + \rho_0\left(v_n - U_{\infty n}\right). \tag{5.10}$$

$$L_i = \rho u_i\left[u_n - (v_n - U_{\infty n})\right] + P_{ij}\hat{n}_j, \tag{5.11}$$

$$T_{ij} = \rho u_i u_j + \Big[(p - p_0) - c_0^2\left(\rho - \rho_0\right)\Big]\delta_{ij} - \sigma_{ij}. \tag{5.12}$$

On the right-hand side of Equation 5.9, the first two terms are the monopole (thickness) and dipole (loading) sources, respectively, acting on the surface $f = 0$, as the Dirac delta function, $\delta(f)$, is presented in these terms. The third term is the quadrupole source acting on the volume exterior to the FW-H surface as indicated by the Heaviside function, $H(f)$. This convective wave equation, Equation 5.9, can be solved on a solid data surface [189, 190, 191] having the disadvantage of performing expensive volume integrals. To alleviate the computational cost, a porous data surface is used for the solution of FW-H equations [192, 193]. The solution to this equation can be performed either in the time-domain [191, 194] or frequency-domain [195, 196, 197]. Farassat's Formulations 1 and 1A [185, 194, 198] are commonly used due to their robustness and low computational cost; however, these solutions do not take into account the presence of the mean flow [186]. Najafi-Yazdi introduced an alternative approach, capable of solving wind tunnel problems, by solving a convective wave equation, firstly derived by Wells and Han [199], to take the presence of the mean flow into account [186]. In this work, we consider a time-domain formulation with a moving medium and a stationary data surface approach where $v_i = 0$, as introduced by Ghorbaniasl [187].

The acoustic pressure consists of three different sources, namely, thickness, loading, and quadrupole sources [187],

$$p'(\boldsymbol{x}, t, \boldsymbol{M}_\infty) = p'_T(\boldsymbol{x}, t, \boldsymbol{M}_\infty) + p'_L(\boldsymbol{x}, t, \boldsymbol{M}_\infty) + p'_Q(\boldsymbol{x}, t, \boldsymbol{M}_\infty), \tag{5.13}$$

where $\boldsymbol{M}_\infty$ is the medium flow Mach number, $p'_T$ is the thickness pressure, $p'_L$ is the loading pressure, and $p'_Q$ is the quadrupole pressure. The first two, thickness and loading pressures, are computed using a surface integration with a low computational cost. However, the evaluation of the

quadrupole source term necessitates a more computationally expensive volume integration. Under certain conditions where the data surface is sufficiently large to encompass all noise sources, the volume integration can be disregarded. Therefore, in many derivations, it is assumed that all noise sources are confined within the data surface, leading to the omission of the volume integration, specifically the quadrupole noise source [186]. The expressions for thickness and loading pressures are as follows [187],

$$4\pi p'_T(\boldsymbol{x}, t, \boldsymbol{M}_\infty) = \int_S \left[\frac{(1 - M_{\infty R})\,\dot{Q}}{R^\star}\right]_e dS - \int_S \left[Q\frac{c_0 M_{\infty R^\star}}{R^{\star 2}}\right]_e dS, \tag{5.14}$$

and

$$4\pi p'_L(\boldsymbol{x}, t, \boldsymbol{M}_\infty) = \frac{1}{c_0}\int_S \left[\frac{\dot{L}_R}{R^\star}\right]_e dS + \int_S \left[\frac{L_{R^\star}}{R^{\star 2}}\right]_e dS, \tag{5.15}$$

where the dot over quantities denotes the temporal derivative with respect to the source time $\tau$, and $c_0$ is the speed of sound. The integrands in Equations 5.14 and 5.15 are defined as

$$M_{\infty R} = M_{\infty i}\tilde{R}_i, \tag{5.16}$$

$$M_{\infty R^\star} = M_{\infty i}\tilde{R}^\star_i, \tag{5.17}$$

$$\dot{L}_R = \dot{L}_i\tilde{R}_i, \tag{5.18}$$

$$L_{R^\star} = L_i\tilde{R}^\star_i, \tag{5.19}$$

$$R^\star = \frac{1}{\gamma}\sqrt{|\boldsymbol{x} - \boldsymbol{y}|^2 + \gamma^2\left(\boldsymbol{M}_\infty \cdot (\boldsymbol{x} - \boldsymbol{y})\right)^2} = \frac{1}{\gamma}\sqrt{r^2 + \gamma^2\left(\boldsymbol{M}_\infty \cdot \boldsymbol{r}\right)^2}, \tag{5.20}$$

$$R = \gamma^2\left(R^\star - \boldsymbol{M}_\infty \cdot \boldsymbol{r}\right), \tag{5.21}$$

$$\gamma^2 = \frac{1}{1 - |\boldsymbol{M}_\infty|^2}, \tag{5.22}$$

$$\tilde{R}^\star_i = \frac{\partial R^\star}{\partial x_i} = \frac{r_i + \gamma^2\left(M_{\infty j} r_j\right) M_{\infty i}}{\gamma^2 R^\star}, \tag{5.23}$$

$$\tilde{R}_i = \frac{\partial R}{\partial x_i} = \gamma^2 \left( \tilde{R}_i^\star - M_{\infty i} \right), \tag{5.24}$$

where $R^\star$ and $R$ are called the amplitude and phase radii, respectively, $\boldsymbol{r} = \boldsymbol{x} - \boldsymbol{y}$ is the distance between the observer position, $\boldsymbol{x}$, and the source position, $\boldsymbol{y}$, and, finally, $\tau = t - \frac{R}{c_0}$ is the source time with $t$ being the observer time. Note that in Equations 5.14 and 5.15, the subscripts $e$ in the integration means that all the integrand quantities are computed in the source time, $\tau$. Thus, the right-hand side is in the source time frame, and the left-hand side is in the observer time frame. There are two main numerical approaches to solving Equations 5.14 and 5.15, namely, the retarded-time approach and the advanced-time approach [190]. This study uses the advanced-time approach known as the source-time-dominant approach. In the retarded-time approach, the observer time is selected in advance, and the source time is calculated as

$$\tau = t - \frac{R}{c_0}, \tag{5.25}$$

then, all the source data are interpolated to the calculated source time. However, in the advanced-time approach, the source time is used to determine when the signal will reach the observer, via

$$t = \tau + \frac{R}{c_0}. \tag{5.26}$$

A sequence of equally-spaced source times will lead to a sequence of unequally-spaced observer times. Then, the contribution of each point on the data surface to the observer noise will reach the observer at an observer time. The obtained observer time history is then interpolated to get the contribution of each source panel at the desired observer time, i.e.

$$4\pi p'(\boldsymbol{x}, t^\star, \boldsymbol{M}_\infty) \approx \sum_{i=1}^{n_p} \mathcal{I}\left(I_i(t), t^\star\right), \tag{5.27}$$

where $p'$ is either $p'_T$ or $p'_L$, $t^\star$ is the desired observer time, $n_p$ is number of points on the data surface, $\mathcal{I}$ is an interpolation operator, and $I_i(t)$ is the right-hand side of either Equation 5.14 or 5.15. Brentner et al. [200] showed that the advanced-time approach requires significantly less

operation than the retarded-time approach and, thus, is more computationally efficient.

## 5.2 Implementation

The time-domain formulation of FW-H for moving medium problems and permeable data surfaces is implemented in Python. Initially, the flow field is numerically computed using an in-house high-order flow solver, HORUS. Once the density, pressure, and velocity fields data is obtained on a pre-defined data surface, it is fed into the FW-H framework. Then, the pressure perturbation can be propagated to any observer location to compute resulting acoustic pressure and sound pressure level. The verification and validation processes for the acoustic solver are detailed in the following sections.

## 5.3 Verification

The verification of the acoustic solver is assessed through the examination of two analytical test cases. These involve wind tunnel cases of stationary sources, including a monopole source and a dipole source. The formulation of these analytical tests aligns with the methodology presented by Ghorbaniasl [187].

### 5.3.1 Stationary Monopole

A stationary single-frequency monopole source is located at the origin of a medium moving at a constant velocity. The complex velocity potential, $\varphi_m$, for the monopole in a uniform flow in $x_1$-direction [201] is extended to arbitrary orientation as follows [187],

$$\varphi_m(\boldsymbol{x}, t) = A \frac{1}{4\pi R^\star} \exp\left[i\omega\left(t - \frac{R}{c_0}\right)\right], \tag{5.28}$$

where $R^{\star}$ and $R$ are computed via Equations 5.20 and 5.21, respectively. Then, the acoustic particle velocity and the acoustic pressure are obtained via

$$u_i'(\boldsymbol{x}, t) = \frac{\partial \varphi_m(\boldsymbol{x}, t)}{\partial x_i}, \tag{5.29}$$

and

$$p'(\boldsymbol{x}, t) = -\rho_0 \left( \frac{\partial \varphi_m(\boldsymbol{x}, t)}{\partial t} + c_0 M_{\infty i} \frac{\partial \varphi_m(\boldsymbol{x}, t)}{\partial x_i} \right) = -\rho_0 \left( i\omega + c_0 M_{\infty i} \frac{\partial}{\partial x_i} \right) \varphi_m(\boldsymbol{x}, t), \tag{5.30}$$

respectively. And finally, the induced density is

$$\rho'(\boldsymbol{x}, t) = \frac{p'(\boldsymbol{x}, t)}{c_0^2}. \tag{5.31}$$

Here, the velocity potential amplitude is $A = 1 m^2/s$, the angular frequency of the source is $\omega = 10\pi \ rad/s$, the ambient speed of sound is $c_0 = 340.75 m/s$, the free-stream flow density is $\rho_0 = 1.234 kg/m^3$, and the specific heat ratio of air is $\gamma = 1.4$. Thus, the free-stream pressure is obtained via the ideal gas law as

$$p_0 = \rho_0 R_g T_0 \xrightarrow{c_0 = \sqrt{\gamma R_g T_0}} p_0 = \frac{\rho_0 c_0^2}{\gamma}, \tag{5.32}$$

where $R_g$ is a gas constant. A sphere of radius $r = 1$ is used as the permeable data surface. The sphere is discretized into 30 sections in the polar direction, ensuring that the spacing between data points along each polar section remains constant at $2\pi/45$. This uniform distribution of data points guarantees that each data panel possesses an identical area. To ensure an adequate temporal resolution, a value of $\Delta t/T = 0.02$ is selected, with $T$ representing the period of the source signal. At a distance of 20 $m$ from the source, the radiated sound pressure is recorded for various mean flow orientations. The root-mean-squared value of the monopole acoustic pressure is computed over a duration spanning 10 periods. Figure 5.1 presents these values for different mean flow orientations. Additionally, Figure 5.2 illustrates a comparison between the calculated monopole acoustic pressure time history and the exact solution. Both figures depict an exact match between

the predicted pressure perturbation, determined using the FW-H method, and the corresponding analytical values, showing the accuracy of the acoustic solver for monopole-like sources.

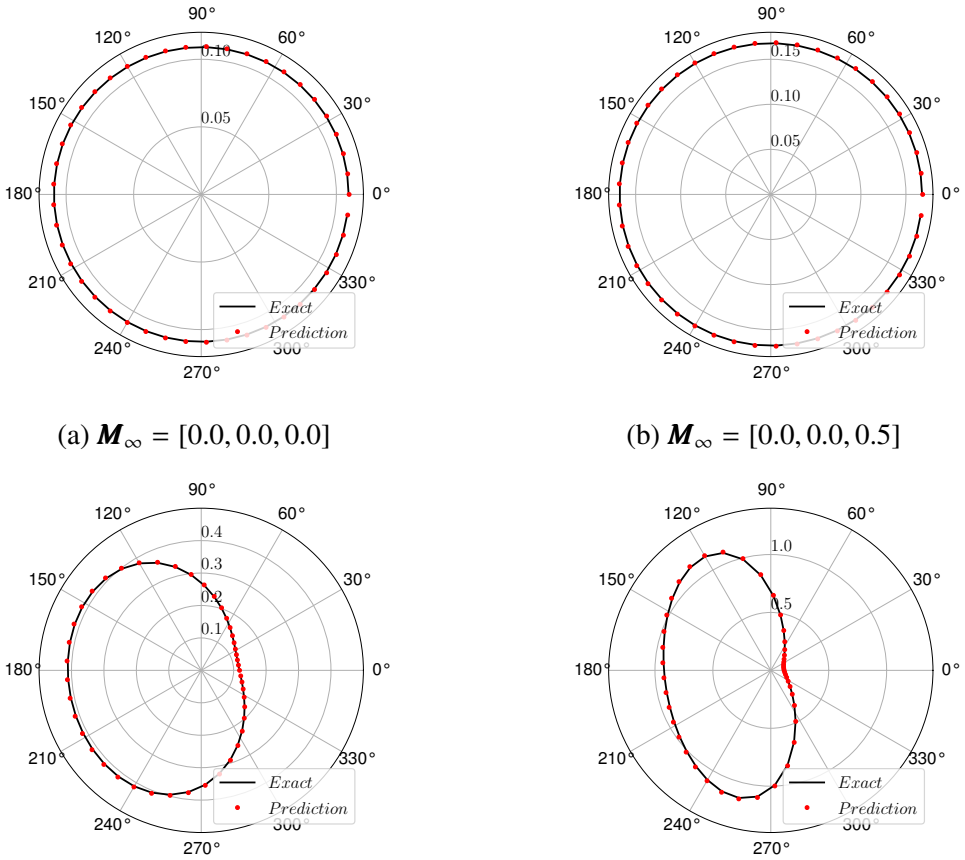


(a) $\boldsymbol{M}_\infty = [0.0, 0.0, 0.0]$

(b) $\boldsymbol{M}_\infty = [0.0, 0.0, 0.5]$

(c) $\boldsymbol{M}_\infty = [0.5, 0.1, 0.5]$

(d) $\boldsymbol{M}_\infty = [0.7, 0.1, 0.5]$

Figure 5.1. Comparison of the root-mean-squared of the predicted acoustic pressure with the exact solution for different Mach number flows.

### 5.3.2 Stationary Dipole

The second verification test case for the acoustic solver involves a stationary dipole positioned at the origin of a medium moving at a constant velocity with an arbitrary orientation. We assume that the dipole's axis is on the $x_2$-axis aligning with the methodology presented by Ghorbaniasl [187]. In this scenario, the complex velocity potential for the dipole can be expressed as the

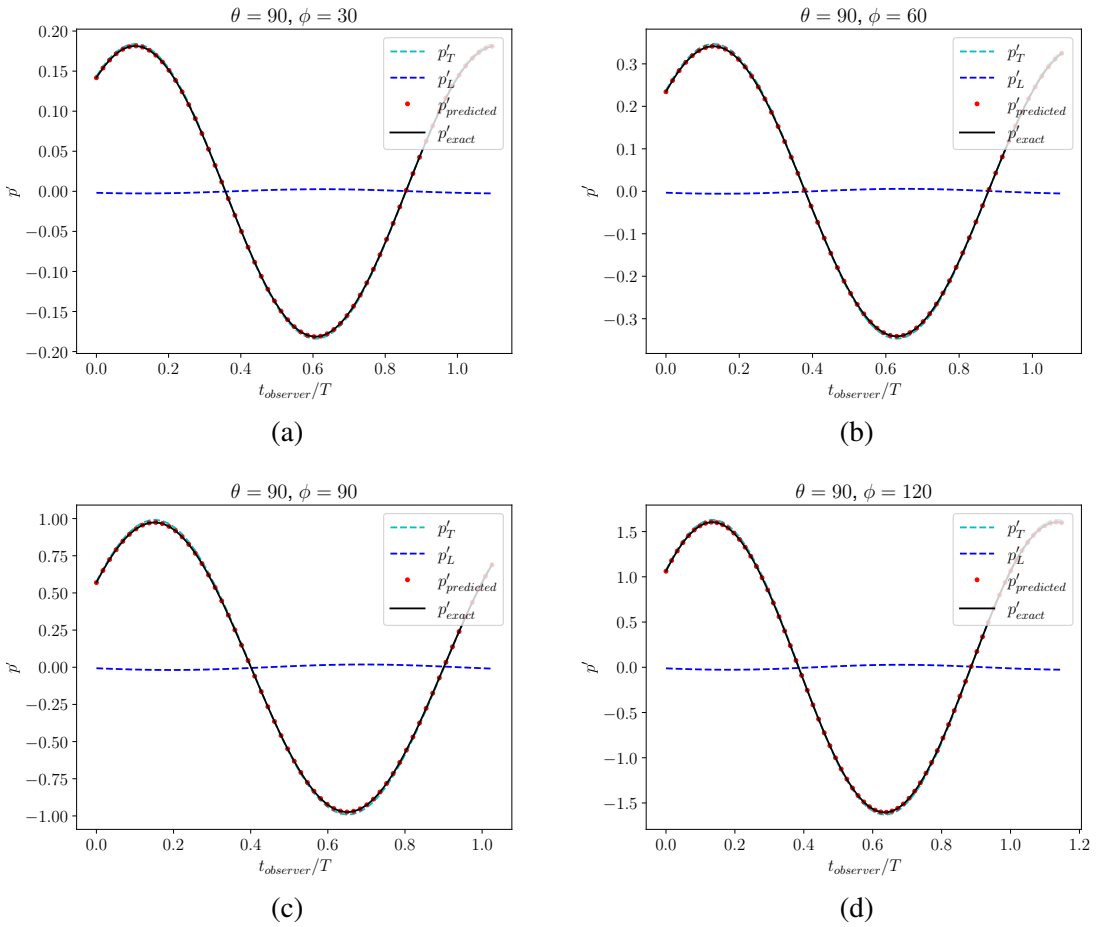


Figure 5.2. Comparison of the predicted and exact acoustic pressure time histories for inflow Mach number of $\boldsymbol{M}_\infty = [0.7, 0.1, 0.5]$.

derivative of the monopole's complex velocity potential with respect to $x_2$,

$$\varphi_d(\boldsymbol{x}, t) = \frac{\partial}{\partial x_2}\varphi_m(\boldsymbol{x}, t). \tag{5.33}$$

The calculation of acoustic particle velocity, pressure, and induced density is performed similarly to the monopole case. In this scenario, a spherical data surface with a radius of $r = 1$ is utilized, mirroring the approach in the monopole case. This spherical surface is discretized into 30 sections in the polar direction, and the azimuthal direction employs a grid size of $2\pi/45$. Temporal calculations maintain a resolution of $\Delta t/T = 0.02$. The radiated sound pressure is recorded at a distance of 100 $m$ from the dipole source. Subsequently, the root-mean-squared value of the acoustic pressure is computed over a span of 10 periods. These computations are conducted for various mean flow orientations, and the results are illustrated in Figure 5.3. Additionally, Figure 5.4 displays the time history of the acoustic pressure. Both figures exhibit an exact match between the FW-H prediction and the analytical data, affirming the accuracy of the FW-H solver for dipole-like sources.

## 5.4 Validation

The FW-H framework is validated using monopoles in an inviscid and quiescent flow. Thus, the Euler equations are solved at an inflow Mach number of zero, where a source term is added to the energy equation to act as a monopole.

### 5.4.1 Monopole in Quiescent Flow Using Euler Equations

The source term for the single monopole is defined as

$$s(\boldsymbol{x}, t) = Ae^{-k\left[(x-x_s)^2+(y-y_s)^2+(z-z_s)^2\right]}\sin(2\pi\omega t), \tag{5.34}$$

where $A = 0.05$ is the amplitude, $k = 100\ 1/m^2$ is the range factor, $[x_s, y_s, z_s] = [0, 0, 0]$ is the location of the source or monopole, and $\omega = 0.5\ 1/s$ is the frequency.

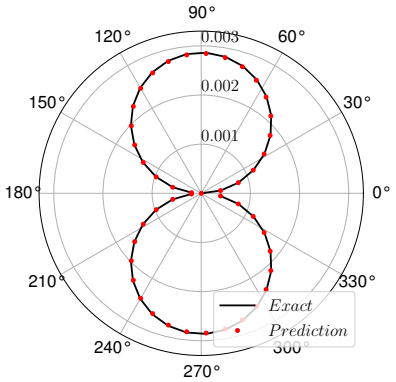


(a) $\boldsymbol{M}_\infty = [0.0, 0.0, 0.4]$

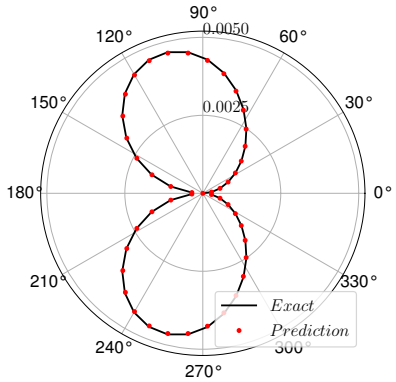


(b) $\boldsymbol{M}_\infty = [0.4, 0.0, 0.4]$

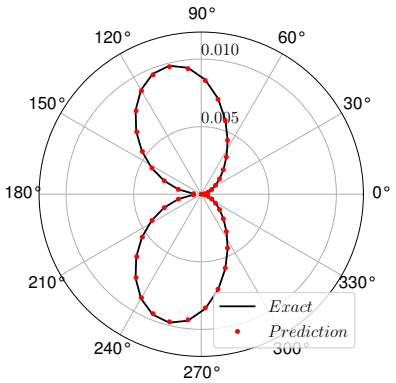


(c) $\boldsymbol{M}_\infty = [0.6, 0.0, 0.4]$

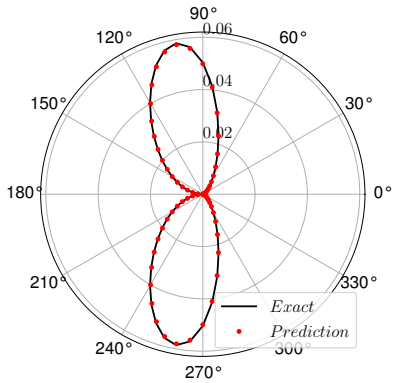


(d) $\boldsymbol{M}_\infty = [0.8, 0.0, 0.4]$

Figure 5.3. Comparison of the root-mean-squared of the predicted acoustic pressure with the exact solution for different Mach number flows.

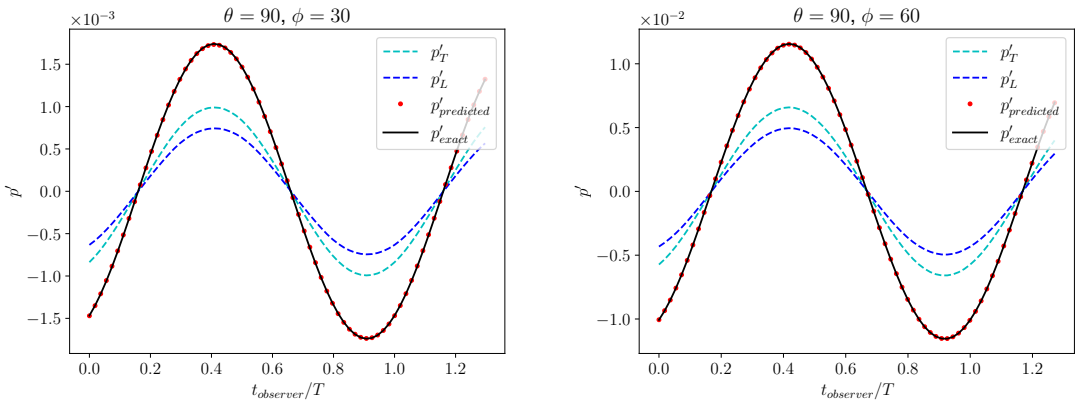


(a) (b) (c) (d)

Figure 5.4. Comparison of the predicted and exact acoustic pressure time histories for inflow Mach number of $\boldsymbol{M}_\infty = [0.8, 0.0, 0.4]$.

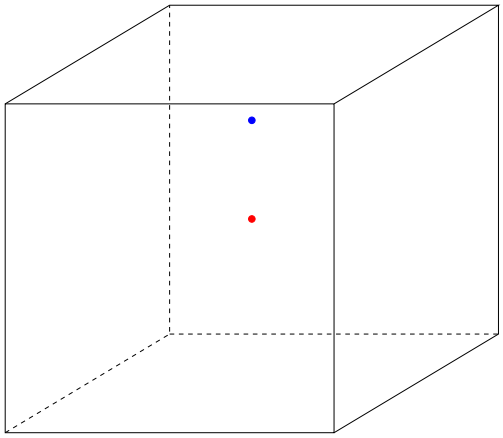

Figure 5.5. The computational domain with the monopole in red and the observer in blue.

In this problem, the source term exhibits characteristics similar to a Gaussian bump, and it undergoes oscillations in the domain. This oscillation introduces a fluctuating pressure field around the source point. The absence of vortices, due to a zero inflow Mach number and inviscid flow conditions, eliminates challenges related to boundary treatments. Consequently, this setup serves as a robust validation for the FW-H framework.

#### 5.4.1.1 Computational Details

A cube of size $[10 \times 10 \times 10]$ is discretized into a total of $125,000$ structured hexahedral elements, and Riemann invariant boundary conditions are applied. An observer is located at $[x_{obs}, y_{obs}, z_{obs}] = [0, 3, 0]$, positioned above the source. The Euler equations are solved using $\mathcal{P}3$ simulation, and the flow data is collected on a spherical data surface with a radius of $r = 1.5$. Figure 5.5 visualizes the computational domain, source location, and observer position. The acoustic pressure at the observer location is determined through two distinct approaches. First, it is directly computed from the flow solver at the observer's position, using a $\mathcal{P}3$ simulation. Second, the flow data are collected at the data surface using $\mathcal{P}1$, $\mathcal{P}2$, and $\mathcal{P}3$ simulations, and are fed into the acoustic solver. Then, the pressure perturbation is computed at the observer's location via the acoustic solver, using three distinct data sets. The resulting acoustic pressure field obtained via these two methods are then compared with each other.

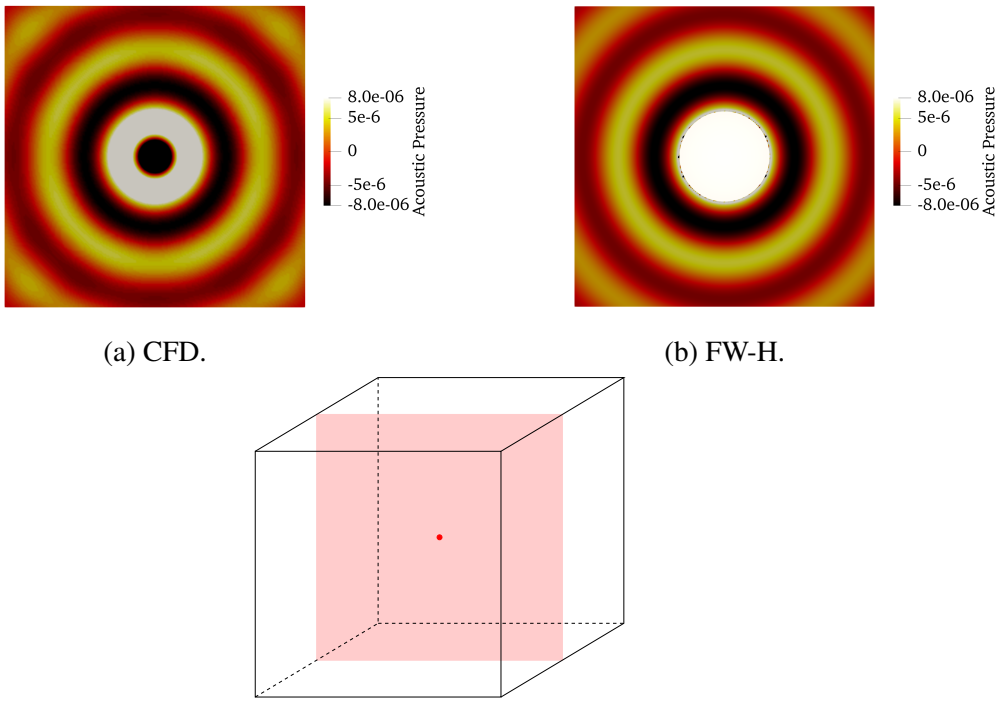


(a) CFD.

(b) FW-H.

(c) The slice through the domain.

Figure 5.6. The acoustic pressure field obtained via both CFD $\mathcal{P}3$ simulation and FW-H $\mathcal{P}3$.

#### 5.4.1.2 Results and Discussion

Figure 5.6 displays the acoustic pressure field, obtained via the $\mathcal{P}3$ CFD simulation, alongside the acoustic solver fed by $\mathcal{P}3$ CFD inputs. This depiction is presented on a slice through the domain. The time history of the acoustic pressure at the observer location is depicted in Figure 5.7, employing both approaches. Notably, when employing the results of $\mathcal{P}1$ CFD simulation for the acoustic solver, there is an over-prediction of the acoustic pressure. However, a favorable agreement with the direct CFD results is observed when $\mathcal{P}2$ and $\mathcal{P}3$ CFD simulations are used as inputs to the acoustic solver, i.e. more accurate inputs are provided for the acoustic solver. This outcome underscores the significant influence of flow solver accuracy on acoustic prediction accuracy, reaffirming the importance of providing precise data to the acoustic solver.

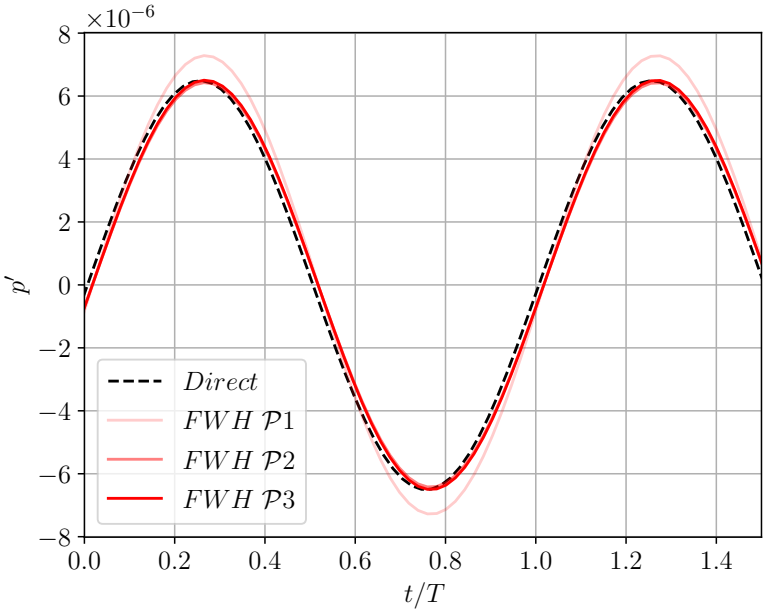


Figure 5.7. Time history of the acoustic pressure.

### 5.4.2 Multiple Monopoles in the Domain

To introduce complexity to the acoustic field, the previous problem is repeated by employing four monopoles, each characterized by distinct amplitudes and frequencies, and they are located in close proximity to the origin. The source term added to the energy equation is defined as follows, utilizing the same parameters and definitions as Equation 5.34,

$$s(\boldsymbol{x},t) = Ae^{-k\left[(x-x_{s_1})^2+(y-y_{s_1})^2+(z-z_{s_1})^2\right]}\sin(2\pi\omega t) + Ae^{-k\left[(x-x_{s_2})^2+(y-y_{s_2})^2+(z-z_{s_2})^2\right]}\sin(8\pi\omega t) + 2Ae^{-k\left[(x-x_{s_3})^2+(y-y_{s_3})^2+(z-z_{s_3})^2\right]}\sin(4\pi\omega t) + 4Ae^{-k\left[(x-x_{s_1})^2+(y-y_{s_1})^2+(z-z_{s_1})^2\right]}\sin(2\pi\omega t), \tag{5.35}$$

where the monopoles are located at $[x_{s_1}, y_{s_1}, z_{s_1}] = [0,0,0]$, $[x_{s_2}, y_{s_2}, z_{s_2}] = [0.1, 0.3, 0.2]$, $[x_{s_3}, y_{s_3}, z_{s_3}] = [-0.2, 0.4, -0.3]$, and $[x_{s_4}, y_{s_4}, z_{s_4}] = [-0.4, -0.2, 0.1]$. The snapshots of the acoustic pressure field are illustrated in Figure 5.8, demonstrating a qualitative agreement between flow solver and acoustic solver results. Furthermore, Figure 5.9 shows the temporal evolution of the acoustic pressure, exhibiting behavior similar to that of a single monopole source. Notably, as the polynomial degree in the CFD simulation is increased, the accuracy of the acoustic solver outcomes improves.

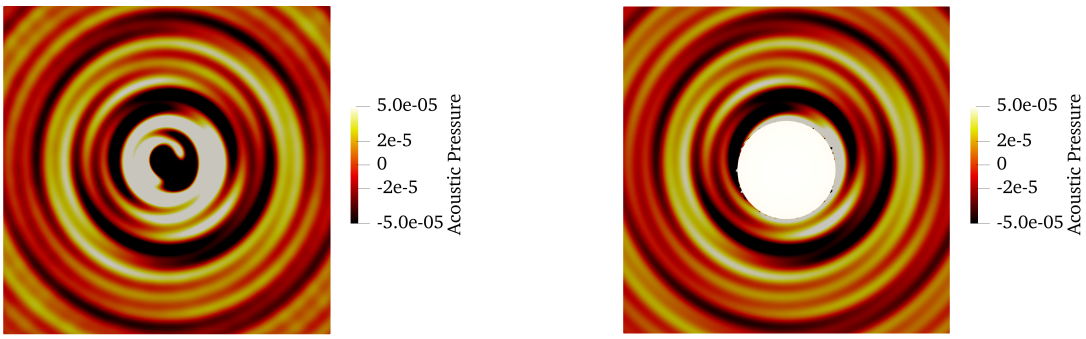


(a) CFD.

(b) FW-H.

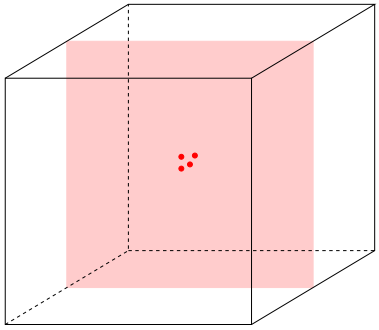

(c) The slice through the domain.

Figure 5.8. The acoustic pressure field obtained via both CFD $\mathcal{P}3$ simulation and FW-H $\mathcal{P}3$.

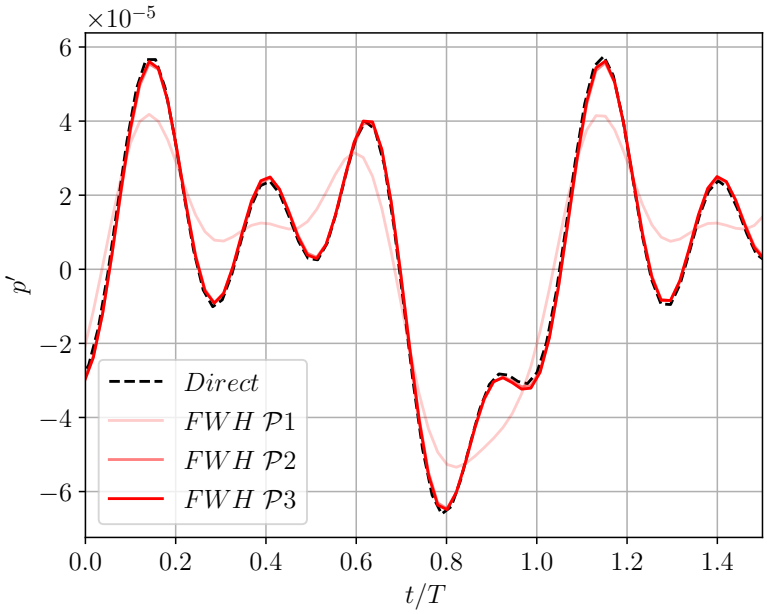


Figure 5.9. Time history of the acoustic pressure.

### 5.4.3 Flow over a NACA0012 Airfoil

In this section, we undertake the validation of the acoustic solver through the solution of the Navier-Stokes equations in the context of viscous flow over a three-dimensional airfoil. NACA0012 airfoil at 6° angle of attack is studied as previously used in Section 4.4. The acoustic solver validation consists of two steps. First, the flow data is computed on a data surface using $\mathcal{P}4$ simulation, along with the acoustic pressure at a near-field observer located at two chord lengths below the trailing edge. Then, the obtained density, velocity, and pressure fields on the data surface are utilized as inputs for the acoustic solver. The pressure perturbation and the Power Spectral Density (PSD) of SPL obtained from the acoustic solver are compared with those of the flow solver.

#### 5.4.3.1 Computational Details

The computational details are the same as Section 4.4. In this section, a data surface is added to the computational domain to collect required inputs for the acoustic solver. The data surface extends to two chord lengths in the $y$-direction, spans up to four chord lengths into the wake region, and covers the entire span of the airfoil. This porous data surface, as depicted in Figure 5.10, encloses pertinent turbulent structures in the near-field region. The data surface remains open-ended to mitigate erroneous acoustic wave generation associated with vortices crossing the data surface. Moreover, the spacing between the sample points on the data surface is set at $0.01c$, ensuring a uniform distribution. Notably, these sample points do not align with the periodic planes to prevent the introduction of spurious noise due to duplicated values on these planes. Thus, the first and last points in the spanwise direction are positioned $0.005c$ away from the periodic planes.

To validate the acoustic solver, the NACA0012 airfoil at a 6° angle of attack is studied. The second-order Nasab-Pereira-Vermeire scheme [56] is used with adaptive time-stepping. The averaged time-step size is approximately $\Delta t_{avg} = 0.001561$. Data collection is conducted every 50 time-steps, resulting in a sampler rate of $\Delta t = 0.018467 t_c$, providing 2166 flow snapshots. This data collection spans an averaging time period of $40 t_c$. The computation of PSD for SPL follows the Welch's method of periodiograms [179] and involves dividing the time period into 3 windows

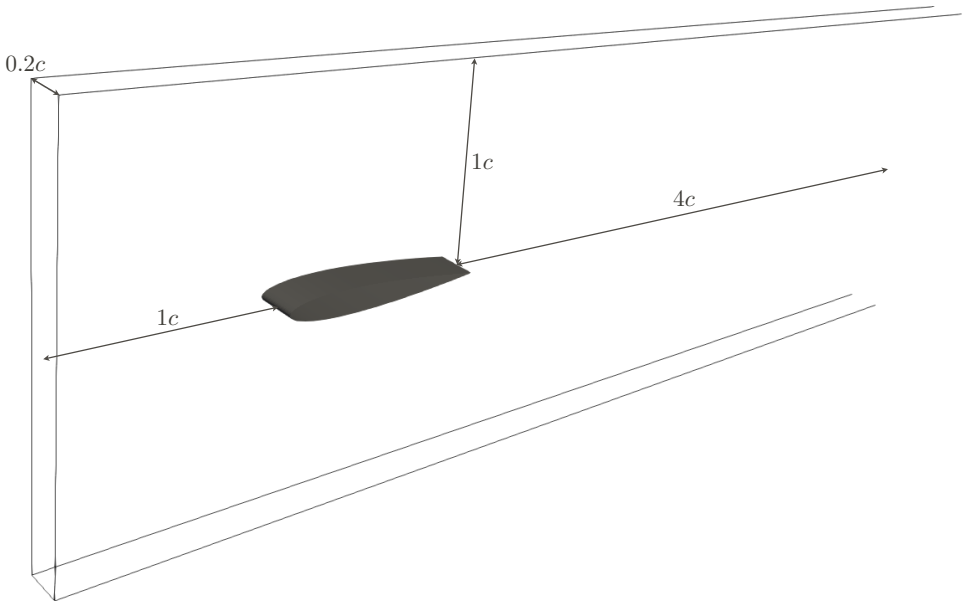


Figure 5.10. Schematic diagram of the data surface with $L_z = 0.2c$.

with a 50% overlap. The PSD of SPL at a near-field observer is computed along with the acoustic pressure time history, to validate the acoustic solver.

#### 5.4.3.2 Results and Discussions

The acoustic pressure time history along with the PSD of SPL for the near-field observer using different spanwise data surface extensions are illustrated in Figure 5.12. It is apparent that the acoustic solver fails to accurately predict pressure perturbations when the data surface is not duplicated in the spanwise direction. This observation underscores that relying solely on the computational domain is insufficient for capturing far-field noise. The primary issue stems from the periodicity in the spanwise direction, which neglects acoustic wave propagation in this dimension within the hybrid approach. To rectify this, an iterative integration of the data surface is necessary on domains shifted either sides of the airfoil over a sufficient distance. The data surface is subsequently duplicated in the spanwise direction, extending to various sets of $L_z$ values. It is evident that extending the data surface up to $L_z = 15c$ proves sufficient for accurate noise prediction. Table 5.1 summarizes the SPL for the near-field observer when using different data surface duplications.

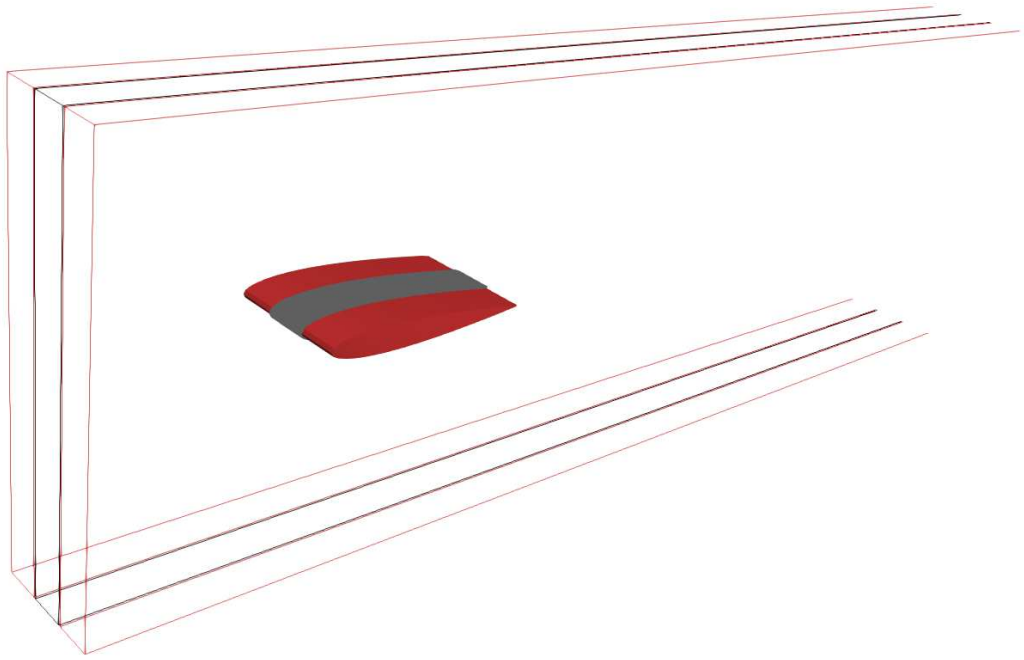

Figure 5.11. Schematic diagram of the repeated CFD data surface in the periodic spanwise direction with $L_z = 0.6c$ fed into the acoustic solver.

A comparison to the direct result, where $SPL = 115.8\ dB$, confirms the effectiveness of data surface duplication up to $L_z = 15c$. Note that according to the inverse square law of acoustic wave dissipation, as the observer is placed further away from the data surface, more duplication of the data surface in the periodic spanwise direction is required.

## 5.5 Shape Optimization of a 4-Digit NACA Airfoil

The shape of a NACA0012 airfoil is optimized to reduce the SPL at a far-field observer located 10 chord lengths below the trailing edge. The design parameters, constraints, and objective function are similar to those of Section 4.4. However, in this section, the acoustic solver is employed rather than computing the sound directly from the flow solver. The density, pressure, and velocity fields data are collected on the data surface and used as inputs to the acoustic solver. To ensure the accuracy of our acoustic analysis, we take into consideration the potential influence of vortices crossing the data surface, which can introduce undesired noise artifacts. To mitigate this, the data

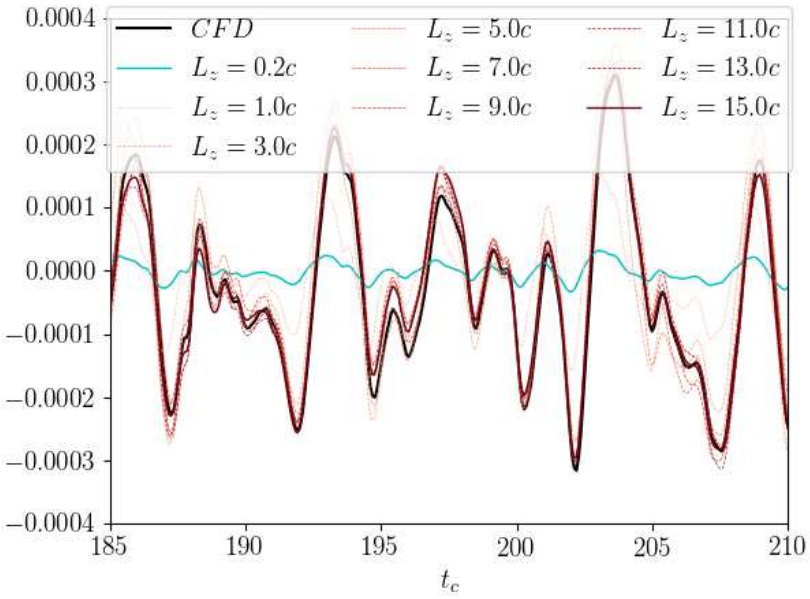


(a) The pressure perturbation time history.

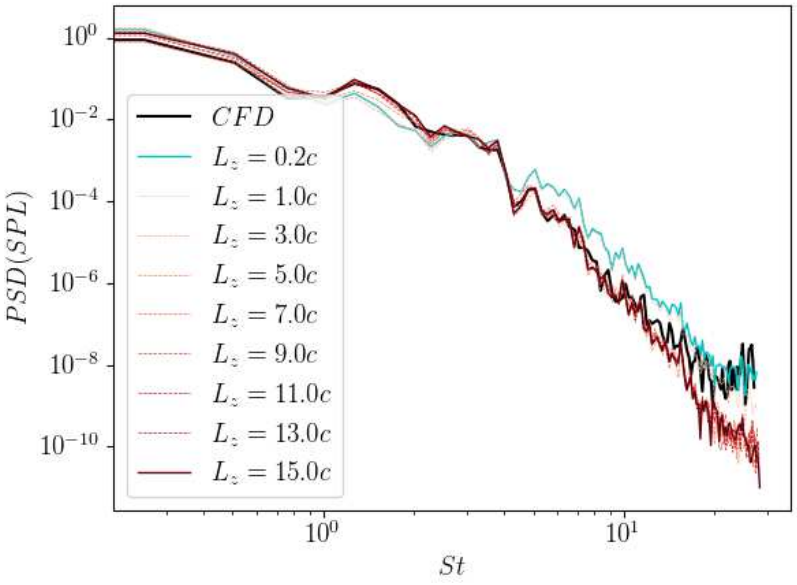


(b) The PSD of SPL.

Figure 5.12. The pressure perturbation time history and PSD of SPL at the near-field observer.

Table 5.1. The SPL of the near-field observer using different sets of data surface duplications.

| Duplication Length ($L_z$) | $SPL$ in $dB$ |
|---|---|
| $0.2c$ | 96.6 |
| $1.0c$ | 110.2 |
| $3.0c$ | 116.6 |
| $5.0c$ | 116.2 |
| $7.0c$ | 115.3 |
| $9.0c$ | 115.8 |
| $11.0c$ | 115.9 |
| $13.0c$ | 115.8 |
| $15.0c$ | 115.8 |

Table 5.2. The SPL of the far-field observer using different sets of data surface duplications.

| Duplication Length ($L_z$) | $SPL$ in $dB$ |
|---|---|
| $0.2c$ | 80.64 |
| $1.0c$ | 94.6 |
| $5.0c$ | 108.1 |
| $9.0c$ | 110.8 |
| $13.0c$ | 108.9 |
| $17.0c$ | 109.5 |
| $21.0c$ | 109.4 |
| $25.0c$ | 109.5 |

surface is tilted to match the angle of attack, mirroring the orientation of the computational domain itself. This precautionary measure effectively prevents vortices from crossing the data surface.

Given that our observer is located in the far-field, we employ multiple sets of data surface duplications to compute the time history of pressure perturbations. The results of this analysis are presented in Figure 5.13. Furthermore, the SPL values using different sets of data surface duplications are summarized in Table 5.2. These results affirm that duplicating the data surface up to $L_z = 25c$ is sufficient for capturing far-field noise.

The aeroacoustic shape optimization framework is illustrated in Figure 5.14 which is similar to the near-field aeroacoustic shape optimization framework, explained in Chapter 3. Initially, the flow field is resolved, and data from the data surface is collected using HORUS. Subsequently, the data from the data surface is duplicated in the spanwise direction to extend over a distance of $L_z = 25c$ and utilized as inputs for the acoustic solver to calculate pressure perturbations at the

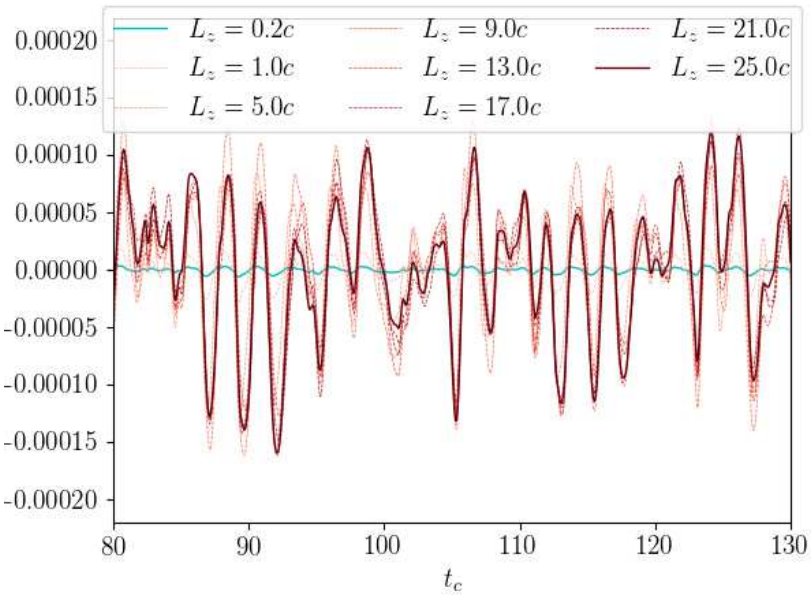


(a) The pressure perturbation time history.

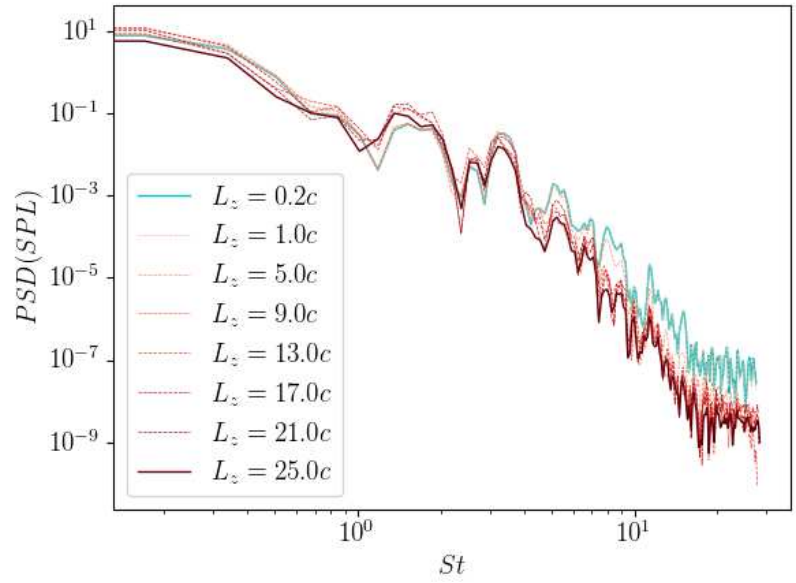


(b) The PSD of SPL.

Figure 5.13. The convergence of the pressure perturbation time history and PSD of SPL at the far-field observer using multiple sets of data surface duplications.

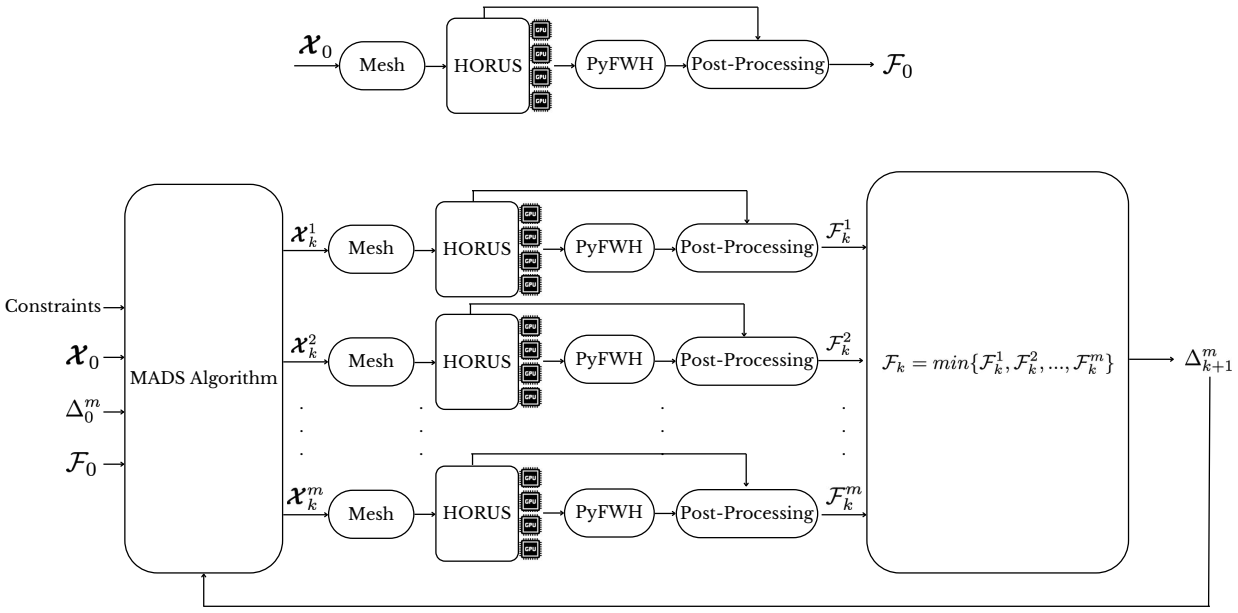


Figure 5.14. The aeroacoustic shape optimization framework.

far-field observer point. The objective function is then evaluated using the SPL obtained from the acoustic solver and the lift and drag coefficients obtained from HORUS, as defined by Equation 4.2. In this proposed framework, design candidates are analyzed simultaneously, and HORUS performs in parallel, employing a two-layered parallelism strategy to eliminate the runtime dependency of the MADS algorithm on the number of design parameters. The results of this optimization process are given in the following section.

### 5.5.1 Results and Discussions

The optimization procedure converges after 25 MADS iterations, consisting of a total of 192 objective function evaluations. The design space and the objective function convergence are depicted in Figure 5.16. The optimal airfoil design has a maximum camber of $c^a_{max} = 0.236206$ percent of the chord, at a 7.8086 tenth of the chord distance from the leading edge, with a thickness of $t^a_{max} = 8.783206$ percent of the chord, at an angle of attack of $\alpha = 6.054932$ degrees. The baseline and optimum airfoils are demonstrated in Figure 5.15. The SPL of the optimized airfoil is

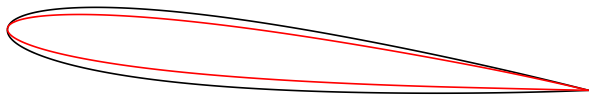

Figure 5.15. The baseline, in black, and optimum, in red, designs of the NACA 4-digits airfoil.

decreased to 95.0 $dB$, the mean lift coefficient is $\overline{C_L} = 0.6489$, and finally, the mean drag coefficient is decreased by 14.07% to $\overline{C_D} = 0.0475$.

The Q-criterion coloured by velocity magnitude along with the pressure perturbation are shown in Figures 5.17 and 5.18 for the baseline and optimum designs, respectively. Similar to Section 4.4, the separation point is closer to the leading edge in the optimum design and the turbulence structures are qualitatively smaller than the baseline design. This results in a substantial decrease of 14.4 $dB$ in SPL at the far-field observer.

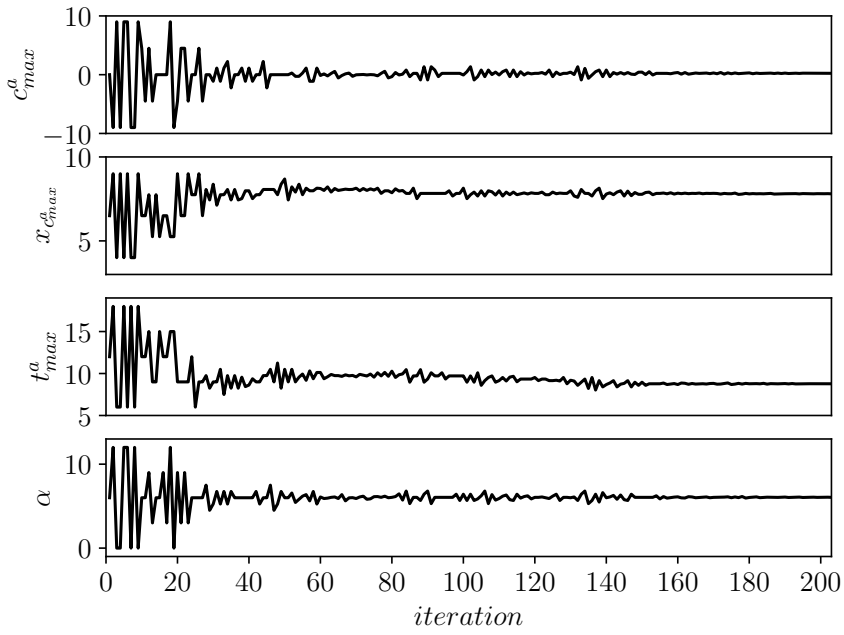


(a) The design space.

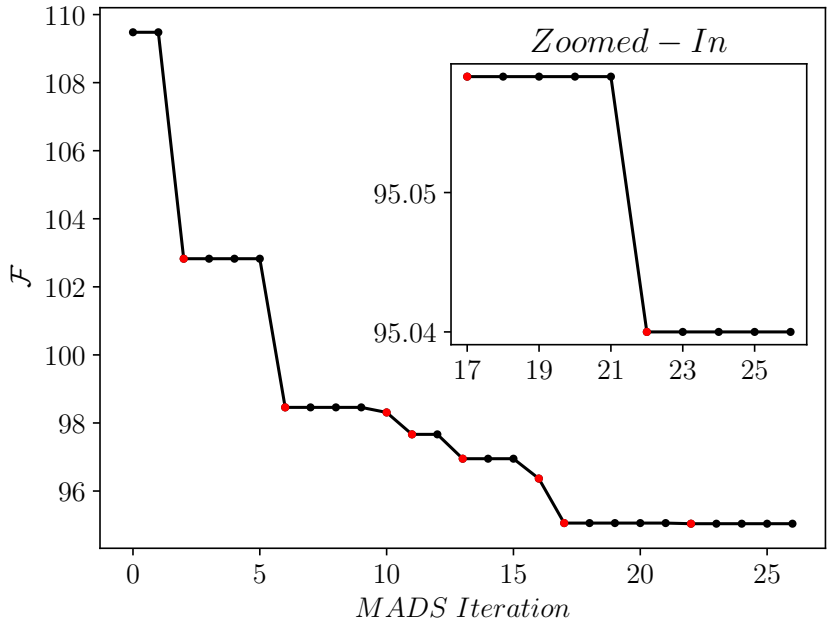


(b) The objective function convergence with the new incumbent design highlighted in red.

Figure 5.16. The design space and objective function convergence of the NACA 4-digit airfoil optimization.

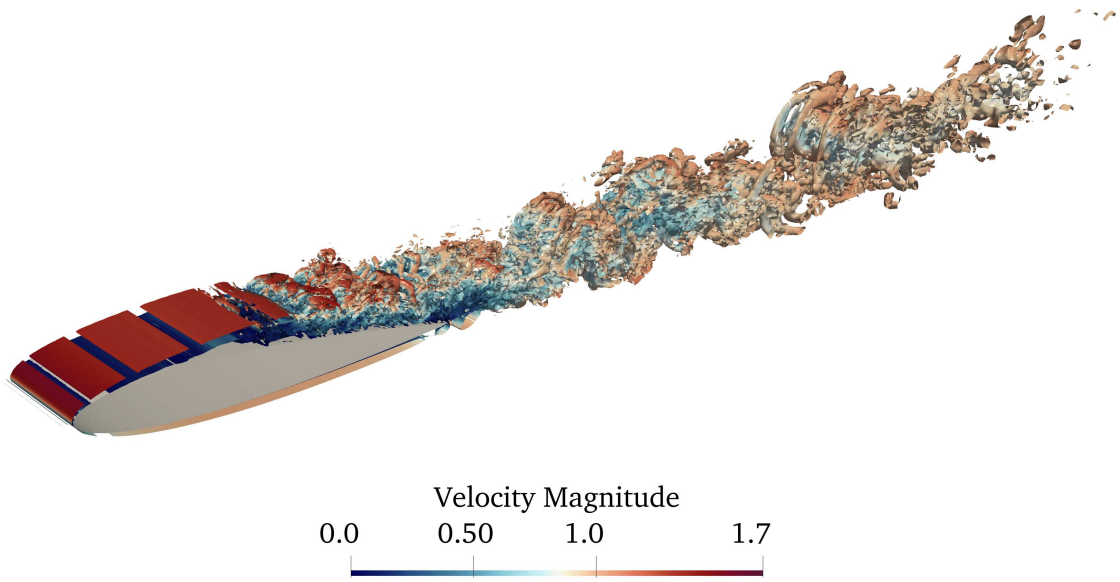


(a) Q-criterion coloured by velocity magnitude.

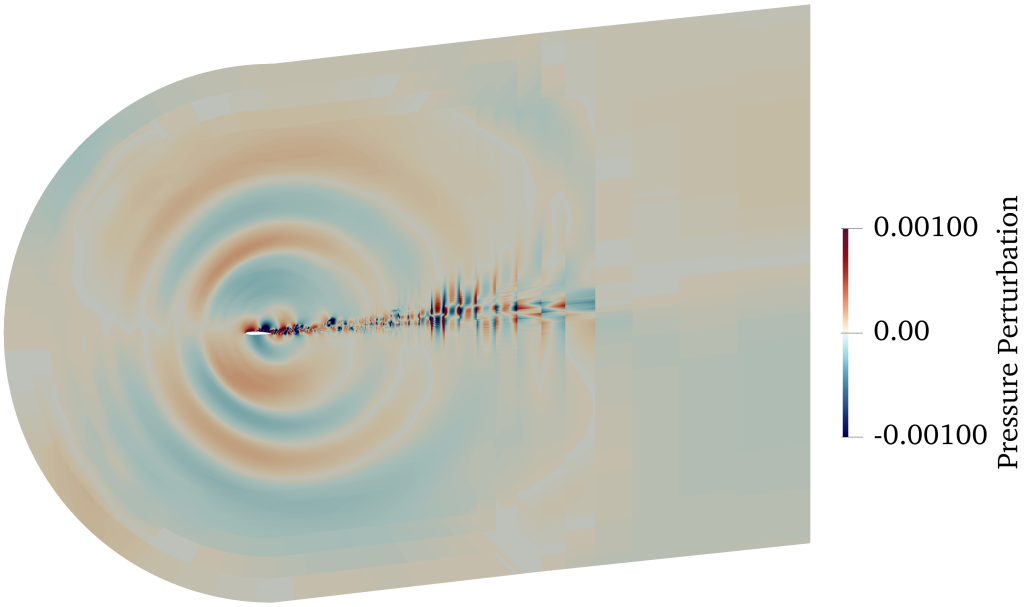


(b) Acoustic pressure field at mid-plane.

Figure 5.17. The baseline airfoil at $t_c = 70$.

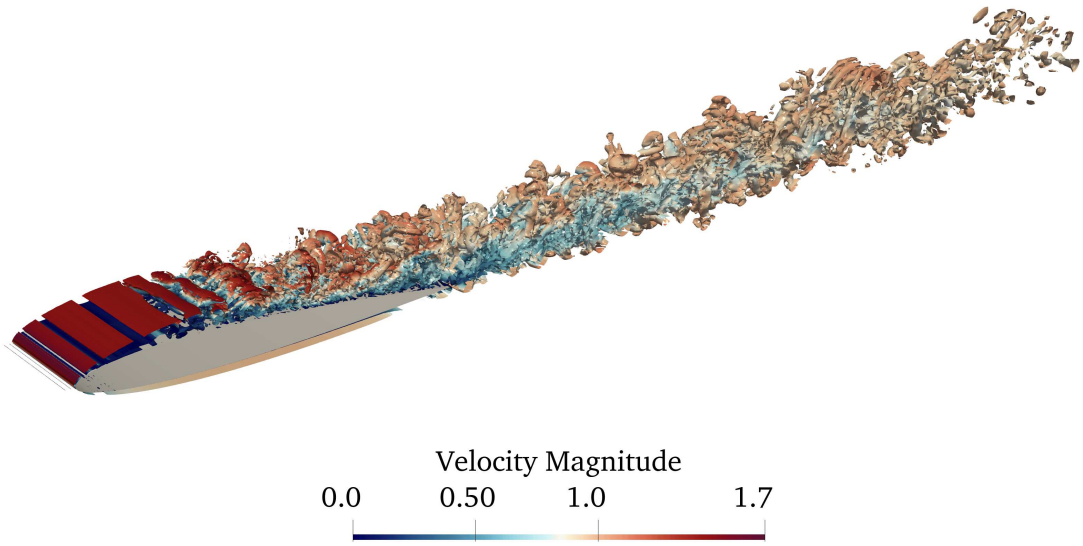


(a) Q-criterion coloured by velocity magnitude.

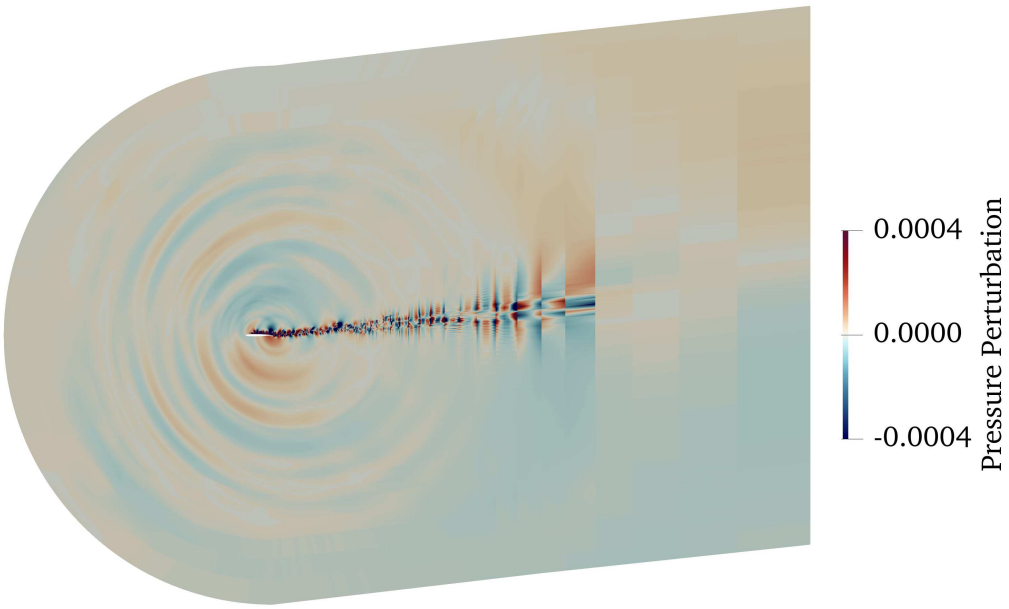


(b) Acoustic pressure field at mid-plane.

Figure 5.18. The optimum airfoil at $t_c$ = 70.

# Chapter 6

# Conclusions and Future Works

An optimization framework has been developed using the gradient-free MADS algorithm, coupled with a high-order unstructured flow solver and an acoustic solver based on the FW-H formulation. This framework performs objective function evaluations in parallel during each optimization iteration, significantly reducing computational runtime. Notably, in this approach, the runtime of gradient-free MADS optimization no longer depends on the number of design variables, provided ample resources are available.

Near-field aeroacoustic shape optimization has been performed for an open deep cavity, tandem cylinders, and NACA 4-digit airfoils. This led to noise reductions of 7.9 $dB$ and 16.5 $dB$ for the cavity and cylinder cases, respectively. The noise is completely eliminated for the NACA 4-digit airfoil, while decreasing the mean drag coefficient by 24.95% and maintaining the mean lift coefficient. This approach extends to three-dimensional turbulent flows, resulting in noise reductions of 12.9 $dB$ and 18.9 $dB$ for the cavity and tandem cylinder problems, respectively. 5.7 $dB$ noise reduction is achieved for the airfoil problem, while decreasing the mean drag coefficient by 7.4% and maintaining the mean lift coefficient. These outcomes demonstrate the suitability of the MADS algorithm when coupled with the flow solver for low Reynolds number problems. Furthermore, the acoustic solver has been validated through analytical test cases involving a stationary monopole and a stationary dipole, affirming its accuracy. It is also verified by solving Euler equations using

the flow solver, emphasizing the strong dependence of the acoustic solver's accuracy on that of the flow solver. The integration of the MADS optimization algorithm with the acoustic solver has been employed to minimize noise for NACA 4-digit airfoils, resulting in a 14.4 $dB$ reduction in noise while reducing the mean drag coefficient by 14.07% and maintaining the mean lift coefficient.

Consequently, this aeroacoustic shape optimization framework effectively reduces noise and enhances aerodynamic performance, demonstrated here in low Reynolds number flows and turbulent conditions, both in the near and far field.

In this investigation, the optimizer has yet to be fully maximized in its capabilities. Our examination of its efficacy and efficiency on simplified industrial problems has showcased promising prospects. By integrating additional engineering constraints to address structural failure and stability within the optimization framework, we can aim to enhance its applicability and robustness. In addition, the effects of observer point locations on optimized shapes and their impact on the optimization process is another intriguing avenue for future work. Furthermore, investigating the influence of turbulent inflow conditions, considering factors like angle of incidence, uniformity, and turbulence, on the optimal shape is vital for comprehensive understanding and improved optimization outcomes. Other future directions for this work may involve parallelizing the acoustic solver to further reduce computational costs. Additionally, the study can be extended to address noise reduction in moving and deforming domains, such as propellers or wind turbines, as well as investigating problems at higher Reynolds numbers. Higher-order surface integration techniques can also be employed within the acoustic solver to reduce the number of samples on the data surface, ultimately lowering the computational cost of each objective function evaluation.

# Bibliography


[1] C. C. Gillispie. *The Montgolfier brothers and the invention of aviation 1783-1784: with a word on the importance of ballooning for the science of heat and the art of building railroads*, volume 684. Princeton University Press, 2014.

[2] O. Anschutz. Otto lilienthal and his glider. https://ghdi.ghi-dc.org/sub_image.cfm?image_id=1595, 1893.

[3] Wright's first powered airplane. https://pixabay.com/photos/plane-wright-brothers-74020/.

[4] Messerschmid me 262 aircraft. https://pixabay.com/photos/messerschmid-me-262-ww2-planes-1412094/.

[5] Airbus a300 aircraft. https://upload.wikimedia.org/wikipedia/commons/2/2c/Airbus_A300B4-603%2C_Lufthansa_AN0520385.jpg.

[6] P. Mills. *Flux Reconstruction as a Direct Method for Near-Field Computational Aeroacoustics*. PhD thesis, Concordia University, 2021.

[7] World Health Organization et al. *Burden of disease from environmental noise: Quantification of healthy life years lost in Europe*. World Health Organization. Regional Office for Europe, 2011.

[8] A. Mahashabde, P. Wolfe, A. Ashok, C. Dorbian, Q. He, A. Fan, S. Lukachko, A. Mozdzanowska, C. Wollersheim, S. R. H. Barrett, et al. Assessing the environmen-

tal impacts of aircraft noise and emissions. *Progress in Aerospace Sciences*, 47(1):15–52, 2011.

[9] M. Basner, C. Clark, A. Hansell, J. I. Hileman, S. Janssen, K. Shepherd, and V. Sparrow. Aviation noise impacts: state of the science. *Noise & health*, 19(87):41, 2017.

[10] C. B. Pepper, M. A. Nascarella, and R. J. Kendall. A review of the effects of aircraft noise on wildlife and humans, current control mechanisms, and the need for further study. *Environmental Management*, 32:418–432, 2003.

[11] Air passenger market analysis, International Air Transport Association (IATA). September, 2020.

[12] Air passenger market analysis, International Air Transport Association (IATA). October, 2018.

[13] J. E. Green. Greener by design—the technology challenge. *The Aeronautical Journal*, 106(1056):57–113, 2002.

[14] N. E. Antoine and I. M. Kroo. Framework for aircraft conceptual design and environmental performance studies. *AIAA Journal*, 43(10):2100–2109, 2005.

[15] O. Turan. An exergy way to quantify sustainability metrics for a high bypass turbofan engine. *Energy*, 86:722–736, 2015.

[16] S. Pinheiro Melo, A. Barke, F. Cerdas, C. Thies, M. Mennenga, T. S. Spengler, and C. Herrmann. Sustainability assessment and engineering of emerging aircraft technologies—challenges, methods and tools. *Sustainability*, 12(14):5663, 2020.

[17] L. Leylekian, A. Covrig, and A. Maximova. *Aviation Noise Impact Management: Technologies, Regulations, and Societal Well-being in Europe*. Springer Nature, 2022.

[18] D. Halliday, R. Resnick, and J. Walker. *Fundamentals of physics*. John Wiley & Sons, 2013.

[19] O. Reynolds. *Papers on Mechanical and Physical Subjects: The sub-mechanics of the universe*, volume 3. The University Press, 1903.

[20] J. Slotnick, A. Khodadoust, J. Alonso, D. Darmofal, W. Gropp, E. Lurie, and D. Mavriplis. CFD vision 2030 study: A path to revolutionary computational aerosciences. 2014.

[21] P. Davidson. *Turbulence: an introduction for scientists and engineers*. Oxford University Press, 2015.

[22] J. Smagorinsky. General circulation experiments with the primitive equations: I. the basic experiment. *Monthly Weather Review*, 91(3):99–164, 1963.

[23] M. Germano, U. Piomelli, P. Moin, and W. H. Cabot. A dynamic subgrid-scale eddy viscosity model. *Physics of Fluids A: Fluid Dynamics*, 3(7):1760–1765, 1991.

[24] F. Sarghini, U. Piomelli, and E. Balaras. Scale-similar models for large-eddy simulations. *Physics of Fluids*, 11(6):1596–1607, 1999.

[25] C. Y. Lee and S. Cant. Assessment of LES subgrid-scale models and investigation of hydrodynamic behaviour for an axisymmetrical bluff body flow. *Flow, Turbulence and Combustion*, 98:155–176, 2017.

[26] Y. Zhiyin. Large-eddy simulation: Past, present and the future. *Chinese Journal of Aeronautics*, 28(1):11–24, 2015.

[27] N. A. Adams and S. Hickel. Implicit large-eddy simulation: Theory and application. In *Advances in Turbulence XII*, pages 743–750. Springer, 2009.

[28] T. Dairay, E. Lamballais, S. Laizet, and J. C. Vassilicos. Numerical dissipation vs. subgrid-scale modelling for large eddy simulation. *Journal of Computational Physics*, 337:252–274, 2017.

[29] Z. L. Chen, S. Hickel, A. Devesa, J. Berland, and N. A. Adams. Wall modeling for implicit large-eddy simulation and immersed-interface methods. *Theoretical and Computational Fluid Dynamics*, 28:1–21, 2014.

[30] K. Chipongo, M. Khiadani, and K. Sookhak Lari. Comparison and verification of turbulence Reynolds-averaged Navier–Stokes closures to model spatially varied flows. *Scientific Reports*, 10(1):19059, 2020.

[31] R. Maulik, H. Sharma, S. Patel, B. Lusch, and E. Jennings. Accelerating RANS turbulence modeling using potential flow and machine learning. *arXiv preprint arXiv:1910.10878*, 2019.

[32] M. Wang, J. B. Freund, and S. K. Lele. Computational prediction of flow-generated sound. *Annu. Rev. Fluid Mech.*, 38:483–512, 2006.

[33] T. Colonius and S. K. Lele. Computational aeroacoustics: progress on nonlinear problems of sound generation. *Progress in Aerospace sciences*, 40(6):345–416, 2004.

[34] F. Magagnato, E. Sorgüven, and M. Gabi. Far field noise prediction by large eddy simulation and Ffowcs Williams Hawkings analogy. In *9th AIAA/CEAS Aeroacoustics Conference and Exhibit*, page 3206, 2003.

[35] D. J. Bodony and S. K. Lele. Current status of jet noise predictions using large-eddy simulation. *AIAA Journal*, 46(2):364–380, 2008.

[36] H. M. Frank and C. Munz. Direct aeroacoustic simulation of acoustic feedback phenomena on a side-view mirror. *Journal of Sound and Vibration*, 371:132–149, 2016.

[37] K. Ritos, I. W. Kokkinakis, D. Drikakis, and S. M. Spottswood. Implicit large eddy simulation of acoustic loading in supersonic turbulent boundary layers. *Physics of Fluids*, 29(4):046101, 2017.

[38] M. A. Alhawwary and Z. J. Wang. Implementation of a FWH approach in a high-order LES tool for aeroacoustic noise predictions. In *AIAA Scitech 2020 Forum*, page 1724, 2020.

[39] J. D. Anderson and J. Wendt. *Computational Fluid Dynamics*, volume 206. Springer, 1995.

[40] J. S. Hesthaven and T. Warburton. *Nodal Discontinuous Galerkin Methods: Algorithms, Analysis, and Applications*. Springer Science & Business Media, 2007.

[41] M. Hamedi and B. C. Vermeire. Optimized filters for stabilizing high-order large eddy simulation. *Computers & Fluids*, 237:105301, 2022.

[42] S. C. Spiegel, H. T. Huynh, and J. R. DeBonis. De-aliasing through over-integration applied to the flux reconstruction and discontinuous Galerkin methods. In *22nd AIAA Computational Fluid Dynamics Conference*, page 2744, 2015.

[43] G. Mengaldo, D. De Grazia, D. Moxey, P. E. Vincent, and S. J. Sherwin. Dealiasing techniques for high-order spectral element methods on regular and irregular grids. *Journal of Computational Physics*, 299:56–81, 2015.

[44] J. S. Park, F. D. Witherden, and P. E. Vincent. High-order implicit large-eddy simulations of flow over a NACA0021 aerofoil. *AIAA Journal*, 55(7):2186–2197, 2017.

[45] B. C. Vermeire, F. D. Witherden, and P. E. Vincent. On the utility of GPU accelerated high-order methods for unsteady flow simulations: A comparison with industry-standard tools. *Journal of Computational Physics*, 334:497–521, 2017.

[46] E. Ching, Y. Lv, and M. Ihme. Entropy residual as a feature-based adaptation indicator for simulations of unsteady flow. In *54th AIAA Aerospace Sciences Meeting*, page 0837, 2016.

[47] M. Tugnoli, A. Abbà, L. Bonaventura, and M. Restelli. A locally p-adaptive approach for large eddy simulation of compressible flows in a DG framework. *Journal of Computational Physics*, 349:33–58, 2017.

[48] R. Ghoreishi and B. C. Vermeire. Vorticity-based polynomial adaptation for moving and deforming domains. *Computers & Fluids*, 231:105160, 2021.

[49] J. Ims and Z. J. Wang. A comparison of three error indicators for adaptive high-order large eddy simulation. *Journal of Computational Physics*, page 112312, 2023.

[50] L. Wang and D. J. Mavriplis. Adjoint-based h-p adaptive discontinuous Galerkin methods for the 2D compressible Euler equations. *Journal of Computational Physics*, 228(20):7643–7661, 2009.

[51] C. Roy. Strategies for driving mesh adaptation in CFD. In *47th AIAA Aerospace Sciences Meeting Including the New Horizons Forum and Aerospace Exposition*, page 1302, 2009.

[52] C. A. Pereira and B. C. Vermeire. Performance and accuracy of hybridized flux reconstruction schemes. *Journal of Computational Physics*, 457:111039, 2022.

[53] B. C. Vermeire, N. A. Loppi, and P. E. Vincent. Optimal embedded pair Runge-Kutta schemes for pseudo-time stepping. *Journal of Computational Physics*, 415:109499, 2020.

[54] B. C. Vermeire. Paired explicit Runge-Kutta schemes for stiff systems of equations. *Journal of Computational Physics*, 393:465–483, 2019.

[55] B. C. Vermeire. Embedded paired explicit Runge-Kutta schemes. *Journal of Computational Physics*, 487:112159, 2023.

[56] S. Hedayati Nasab, C. A. Pereira, and B. C. Vermeire. Optimal Runge-Kutta stability polynomials for multidimensional high-order methods. *Journal of Scientific Computing*, 89(1):11, 2021.

[57] J. Nordström and M. H. Carpenter. High-order finite difference methods, multidimensional linear problems, and curvilinear coordinates. *Journal of Computational Physics*, 173(1):149–174, 2001.

[58] M. R. Visbal and D. V. Gaitonde. On the use of higher-order finite-difference schemes on curvilinear and deforming meshes. *Journal of Computational Physics*, 181(1):155–185, 2002.

[59] N. Nikitin. Finite-difference method for incompressible Navier–Stokes equations in arbitrary orthogonal curvilinear coordinates. *Journal of Computational Physics*, 217(2):759–781, 2006.

[60] A. Harten and S. Osher. Uniformly high-order accurate nonoscillatory schemes. i. *SIAM Journal on Numerical Analysis*, 24(2):279–309, 1987.

[61] X. Liu, S. Osher, and T. Chan. Weighted essentially non-oscillatory schemes. *Journal of Computational Physics*, 115(1):200–212, 1994.

[62] B. Van Leer. Towards the ultimate conservative difference scheme. V. A second-order sequel to Godunov's method. *Journal of Computational Physics*, 32(1):101–136, 1979.

[63] F. D. Witherden, A. M. Farrington, and P. E. Vincent. Pyfr: An open source framework for solving advection–diffusion type problems on streaming architectures using the flux reconstruction approach. *Computer Physics Communications*, 185(11):3028–3040, 2014.

[64] H. T. Huynh. A flux reconstruction approach to high-order schemes including discontinuous Galerkin methods. In *18th AIAA Computational Fluid Dynamics Conference*, page 4079, 2007.

[65] P. Vincent, F. Witherden, B. Vermeire, J. S. Park, and A. Iyer. Towards green aviation with python at petascale. In *SC'16: Proceedings of the International Conference for High Performance Computing, Networking, Storage and Analysis*, pages 1–11. IEEE, 2016.

[66] P. Moriarty and P. Migliore. Semi-empirical aeroacoustic noise prediction code for wind turbines. Technical report, National Renewable Energy Lab., Golden, CO.(US), 2003.

[67] J. M. Jonkman, M. L. Buhl, et al. *FAST user's guide*, volume 365. National Renewable Energy Laboratory Golden, CO, USA, 2005.

[68] M. Kamruzzaman, D. Bekiropoulos, T. Lutz, W. Würz, and E. Krämer. A semi-empirical surface pressure spectrum model for airfoil trailing-edge noise prediction. *International Journal of Aeroacoustics*, 14(5-6):833–882, 2015.

[69] R. D. Sandberg. Compressible-flow DNS with application to airfoil noise. *Flow, Turbulence and Combustion*, 95:211–229, 2015.

[70] J. Winkler, H. Wu, S. Moreau, T. Carolus, and R. D. Sandberg. Trailing-edge broadband noise prediction of an airfoil with boundary-layer tripping. *Journal of Sound and Vibration*, 482:115450, 2020.

[71] E. R. Hawkes, R. Sankaran, J. C. Sutherland, and J. H. Chen. Direct numerical simulation of turbulent combustion: fundamental insights towards predictive models. In *Journal of Physics: Conference Series*, volume 16, page 65. IOP Publishing, 2005.

[72] R. D. Sandberg and N. D. Sandham. Direct numerical simulation of turbulent flow past a trailing edge and the associated noise generation. *Journal of Fluid Mechanics*, 596:353–385, 2008.

[73] R. D. Sandberg, L. E. Jones, N. D. Sandham, and P. F. Joseph. Direct numerical simulations of tonal noise generated by laminar flow past airfoils. *Journal of Sound and Vibration*, 320(4-5):838–858, 2009.

[74] W. P. Song, Z. H. Han, and Z. D. Qiao. Prediction of hovering rotor noise based on Reynolds-averaged Navier-Stokes simulation. *Journal of Aircraft*, 44(4):1391–1395, 2007.

[75] R. Self and A. Bassetti. A RANS based jet noise prediction scheme. In *9th AIAA/CEAS Aeroacoustics Conference and Exhibit*, page 3325, 2003.

[76] X. L. Zhang, H. Xiao, T. Wu, and G. He. Acoustic Inversion for Uncertainty Reduction in Reynolds-Averaged Navier–Stokes-Based Jet Noise Prediction. *AIAA Journal*, 60(4):2407–2422, 2022.

[77] J. E. Ffowcs Williams and D. L. Hawkings. Sound generation by turbulence and surfaces in arbitrary motion. *Philosophical Transactions of the Royal Society of London. Series A, Mathematical and Physical Sciences*, 264(1151):321–342, 1969.

[78] M. J. Lighthill. On sound generated aerodynamically I. General theory. *Proceedings of the Royal Society of London. Series A. Mathematical and Physical Sciences*, 211(1107):564–587, 1952.

[79] M. J. Lighthill. On sound generated aerodynamically ii. turbulence as a source of sound. *Proceedings of the Royal Society of London. Series A. Mathematical and Physical Sciences*, 222(1148):1–32, 1954.

[80] N. Curle. The influence of solid boundaries upon aerodynamic sound. *Proceedings of the Royal Society of London. Series A. Mathematical and Physical Sciences*, 231(1187):505–514, 1955.

[81] D. Casalino, M. Jacob, and M. Roger. Prediction of rod-airfoil interaction noise using the Ffowcs-Williams-Hawkings analogy. *AIAA Journal*, 41(2):182–191, 2003.

[82] S. Mendez, M. Shoeybi, S. K. Lele, and P. Moin. On the use of the Ffowcs Williams-Hawkings equation to predict far-field jet noise from large-eddy simulations. *International Journal of Aeroacoustics*, 12(1-2):1–20, 2013.

[83] M. Cianferra, S. Ianniello, and V. Armenio. Assessment of methodologies for the solution of the Ffowcs Williams and Hawkings equation using LES of incompressible single-phase flow around a finite-size square cylinder. *Journal of Sound and Vibration*, 453:1–24, 2019.

[84] P. R. Spalart and M. L. Shur. Variants of the Ffowcs Williams-Hawkings equation and their coupling with simulations of hot jets. *International Journal of Aeroacoustics*, 8(5):477–491, 2009.

[85] I. Z. Naqavi, Z. Wang, P. G. Tucker, M. Mahak, and P. Strange. Far-field noise prediction for jets using large-eddy simulation and Ffowcs Williams–Hawkings method. *International Journal of Aeroacoustics*, 15(8):757–780, 2016.

[86] A. Uzun, A. S. Lyrintzis, and G. A. Blaisdell. Coupling of integral acoustics methods with LES for jet noise prediction. *International Journal of Aeroacoustics*, 3(4):297–346, 2004.

[87] H. Xia, P. G. Tucker, and S. Eastwood. Large-eddy simulations of chevron jet flows with noise predictions. *International Journal of Heat and Fluid Flow*, 30(6):1067–1079, 2009.

[88] A. L. Bodling and A. Sharma. Implementation of the Ffowcs Williams-Hawkings equation: Predicting the far field noise from airfoils while using boundary layer tripping mechanisms. In *Fluids Engineering Division Summer Meeting*, volume 51555, page V001T08A006. American Society of Mechanical Engineers, 2018.

[89] H. Wu, M. Sanjose, S. Moreau, and R. D. Sandberg. Direct numerical simulation of the self-noise radiated by the installed controlled-diffusion airfoil at transitional Reynolds number. In *2018 AIAA/CEAS Aeroacoustics Conference*, page 3797, 2018.

[90] X. Gloerfelt, C. Bailly, and D. Juvé. Direct computation of the noise radiated by a subsonic cavity flow and application of integral methods. *Journal of Sound and Vibration*, 266(1):119–146, 2003.

[91] M. P. Rumpfkeil and D. W. Zingg. A hybrid algorithm for far-field noise minimization. *Computers & Fluids*, 39(9):1516–1528, 2010.

[92] J. Tao and G. Sun. A novel optimization method for maintaining aerodynamic performances in noise reduction design. *Aerospace Science and Technology*, 43:415–422, 2015.

[93] B. Zhou, T. A. Albring, N. R. Gauger, C. Ilario, T. D. Economon, and J. J. Alonso. Reduction of airframe noise components using a discrete adjoint approach. In *18th AIAA/ISSMO Multidisciplinary Analysis and Optimization Conference*, page 3658, 2017.

[94] A. Jameson and K. Ou. Optimization methods in computational fluid dynamics. *Encyclopedia of Aerospace Engineering*, 2010.

[95] W. K. Anderson, J. C. Newman, D. L. Whitfield, and E. J. Nielsen. Sensitivity analysis for Navier-Stokes equations on unstructured meshes using complex variables. *AIAA Journal*, 39(1):56–63, 2001.

[96] D. W. Zingg, M. Nemec, and T. H. Pulliam. A comparative evaluation of genetic and gradient-based algorithms applied to aerodynamic optimization. *European Journal of Computational Mechanics/Revue Européenne de Mécanique Numérique*, 17(1-2):103–126, 2008.

[97] A. Jameson. Aerodynamic design via control theory. *Journal of Scientific Computing*, 3:233–260, 1988.

[98] O. Pironneau. On optimum design in fluid mechanics. *Journal of Fluid Mechanics*, 64(1):97–110, 1974.

[99] J. J. Reuther, A. Jameson, J. J. Alonso, M. J. Rimllnger, and D. Saunders. Constrained multipoint aerodynamic shape optimization using an adjoint formulation and parallel computers, part 2. *Journal of Aircraft*, 36(1):61–74, 1999.

[100] J. Elliott and J. Peraire. Practical three-dimensional aerodynamic design and optimization using unstructured meshes. *AIAA Journal*, 35(9):1479–1485, 1997.

[101] E. J. Nielsen and W. K. Anderson. Aerodynamic design optimization on unstructured meshes using the Navier-Stokes equations. *AIAA Journal*, 37(11):1411–1419, 1999.

[102] M. Nemec and D. W. Zingg. Newton-Krylov algorithm for aerodynamic design using the Navier-Stokes equations. *AIAA Journal*, 40(6):1146–1154, 2002.

[103] A. Griewank et al. On automatic differentiation. *Mathematical Programming: Recent Developments and Applications*, 6(6):83–107, 1989.

[104] J. Luo, J. Xiong, and F. Liu. Aerodynamic design optimization by using a continuous adjoint method. *SCIENCE CHINA Physics, Mechanics & Astronomy*, 57(7):1363–1375, 2014.

[105] P. He, C. A. Mader, J. R. R. A. Martins, and K. J. Maki. Dafoam: An open-source adjoint framework for multidisciplinary design optimization with OpenFOAM. *AIAA Journal*, 58(3):1304–1319, 2020.

[106] Y. Shi, C. A. Mader, S. He, G. L. O. Halila, and J. R. R. A. Martins. Natural laminar-flow airfoil optimization design using a discrete adjoint approach. *AIAA Journal*, 58(11):4702–4722, 2020.

[107] P. J. Blonigan, P. Fernandez, S. M. Murman, Q. Wang, G. Rigas, and L. Magri. Toward a chaotic adjoint for LES. *arXiv preprint arXiv:1702.06809*, 2017.

[108] S. N. Sivanandam, S. N. Deepa, S. N. Sivanandam, and S. N. Deepa. *Genetic algorithms*. Springer, 2008.

[109] L. M. Schmitt. Theory of genetic algorithms II: models for genetic operators over the string-tensor representation of populations and convergence to global optima for arbitrary fitness function under scaling. *Theoretical Computer Science*, 310(1-3):181–231, 2004.

[110] C. Praveen and R. Duvigneau. Low cost pso using metamodels and inexact pre-evaluation: Application to aerodynamic shape design. *Computer Methods in Applied Mechanics and Engineering*, 198(9-12):1087–1096, 2009.

[111] Y. Wang, B. Zhang, and Y. Chen. Robust airfoil optimization based on improved particle swarm optimization method. *Applied Mathematics and Mechanics*, 32:1245–1254, 2011.

[112] Y. Zhang, S. Wang, G. Ji, et al. A comprehensive survey on particle swarm optimization algorithm and its applications. *Mathematical Problems in Engineering*, 2015, 2015.

[113] C. Audet and J. E. Dennis Jr. Mesh adaptive direct search algorithms for constrained optimization. *SIAM Journal on Optimization*, 17(1):188–217, 2006.

[114] M. A. Abramson, C. Audet, J. E. Dennis Jr, and S. L. Digabel. OrthoMADS: A deterministic MADS instance with orthogonal directions. *SIAM Journal on Optimization*, 20(2):948–966, 2009.

[115] V. Torczon. On the convergence of pattern search algorithms. *SIAM Journal on Optimization*, 7(1):1–25, 1997.

[116] I. D. Coope and C. J. Price. On the convergence of grid-based methods for unconstrained optimization. *SIAM Journal on Optimization*, 11(4):859–869, 2001.

[117] C. Davis. Theory of positive linear dependence. *American Journal of Mathematics*, 76(4):733–746, 1954.

[118] A. L. Marsden, M. Wang, J. E. Dennis, and P. Moin. Trailing-edge noise reduction using derivative-free optimization and large-eddy simulation. *Journal of Fluid Mechanics*, 572:13–36, 2007.

[119] L. S. Brar and K. Elsayed. Analysis and optimization of multi-inlet gas cyclones using large eddy simulation and artificial neural network. *Powder Technology*, 311:465–483, 2017.

[120] L. S. Brar and K. Elsayed. Analysis and optimization of cyclone separators with eccentric vortex finders using large eddy simulation and artificial neural network. *Separation and Purification Technology*, 207:269–283, 2018.

[121] H. R. Karbasian and B. C. Vermeire. Gradient-free aerodynamic shape optimization using large eddy simulation. *Computers & Fluids*, 232:105185, 2022.

[122] J. C. Hardin and S. L. Lamkin. Computational aeroacoustics—present status and future promise. In *Aero-and Hydro-Acoustics: IUTAM Symposium, Ecole Centrale de Lyon, 3–6 July, 1985*, pages 253–259. Springer, 1986.

[123] H. Nishikawa, Y. Nakashima, and N. Watanabe. Effects of high-frequency damping on iterative convergence of implicit viscous solver. *Journal of Computational Physics*, 348:66–81, 2017.

[124] J. C. Butcher and N. Goodwin. *Numerical Methods for Ordinary Differential Equations*, volume 2. Wiley Online Library, 2008.

[125] J. C. Butcher. *The Numerical Analysis of Ordinary Differential Equations: Runge-Kutta and General Linear Methods*. Wiley-Interscience, 1987.

[126] H. J. Stetter et al. *Analysis of Discretization Methods for Ordinary Differential Equations*, volume 23. Springer, 1973.

[127] E. Hairer, S. P. Nørsett, and G. Wanner. *Solving Ordinary Differential Equations. 1, Nonstiff Problems*. Springer-Vlg, 1993.

[128] S. H. Nasab and B. C. Vermeire. Third-order Paired Explicit Runge-Kutta schemes for stiff systems of equations. *Journal of Computational Physics*, 468:111470, 2022.

[129] L. M. Skvortsov. Third-and fourth-order ESDIRK methods for stiff and differential-algebraic problems. *Computational Mathematics and Mathematical Physics*, 62(5):766–783, 2022.

[130] C. Wang and H. Luo. A reconstructed discontinuous Galerkin method for compressible flows on moving curved grids. *Advances in Aerodynamics*, 3(1):1–28, 2021.

[131] B. C. Vermeire and P. E. Vincent. On the properties of energy stable flux reconstruction schemes for implicit large eddy simulation. *Journal of Computational Physics*, 327:368–388, 2016.

[132] Z. J. Wang and H. Gao. A unifying lifting collocation penalty formulation including the discontinuous Galerkin, spectral volume/difference methods for conservation laws on mixed grids. *Journal of Computational Physics*, 228(21):8161–8186, 2009.

[133] D. M. Williams, L. Shunn, and A. Jameson. Symmetric quadrature rules for simplexes based on sphere close packed lattice arrangements. *Journal of Computational and Applied Mathematics*, 266:18–38, 2014.

[134] L. Shunn and F. Ham. Symmetric quadrature rules for tetrahedra based on a cubic close-packed lattice arrangement. *Journal of Computational and Applied Mathematics*, 236(17):4348–4364, 2012.

[135] H. Karbasian and W. M. van Rees. A deep-learning surrogate model approach for optimization of morphing airfoils. In *AIAA SCITECH 2023 Forum*, page 1619, 2023.

[136] M. Nemec, D. W. Zingg, and T. H. Pulliam. Multipoint and multi-objective aerodynamic shape optimization. *AIAA Journal*, 42(6):1057–1065, 2004.

[137] J. E. Hicken and D. W. Zingg. Aerodynamic optimization algorithm with integrated geometry parameterization and mesh movement. *AIAA Journal*, 48(2):400–413, 2010.

[138] A. Aubry, H. R. Karbasian, and B. C. Vermeire. High-fidelity gradient-free optimization of low-pressure turbine cascades. *Computers & Fluids*, 248:105668, 2022.

[139] P. Kholodov and S. Moreau. Optimization of serrations for broadband trailing-edge noise reduction using an analytical model. In *25th AIAA/CEAS Aeroacoustics Conference*, page 2655, 2019.

[140] J. Rottmayer, E. Özkaya, S. Satcunanathan, B. Zhou, M. Aehle, N. R. Gauger, M. Meinke, W. Schröder, and S. Pullin. Trailing-edge noise reduction using porous treatment and surrogate-based global optimization. *arXiv preprint arXiv:2301.13047*, 2023.

[141] D. Xue, Q. Yan, Z. Li, and K. Wei. Multidisciplinary optimization design of low-noise propellers. *Aerospace*, 10(3):254, 2023.

[142] Y. Peixun, P. Jiahui, B. Junqiang, H. Xiao, and S. Xiang. Aeroacoustic and aerodynamic optimization of propeller blades. *Chinese Journal of Aeronautics*, 33(3):826–839, 2020.

[143] B. Marinus, M. Roger, and R. Van Den Braembussche. Aeroacoustic and aerodynamic optimization of aircraft propeller blades. In *16th AIAA/CEAS Aeroacoustics Conference*, page 3850, 2010.

[144] M. Gharib and A. Roshko. The effect of flow oscillations on cavity drag. *Journal of Fluid Mechanics*, 177:501–530, 1987.

[145] T. Colonius, A. Basu, and C. Rowley. Numerical investigation of the flow past a cavity. In *5th AIAA/CEAS Aeroacoustics Conference and Exhibit*, page 1912, 1999.

[146] C. W. Rowley, T. Colonius, and A. J. Basu. On self-sustained oscillations in two-dimensional compressible flow over rectangular cavities. *Journal of Fluid Mechanics*, 455:315–346, 2002.

[147] J. Larsson, L. Davidson, M. Olsson, and L. Eriksson. Aeroacoustic investigation of an open cavity at low mach number. *AIAA Journal*, 42(12):2462–2473, 2004.

[148] J. Ask and L. Davidson. Sound generation and radiation of an open two-dimensional cavity. *AIAA Journal*, 47(6):1337–1349, 2009.

[149] R. Martin, M. Soria, O. Lehmkuhl, A. Gorobets, and A. Duben. Noise radiated by an open cavity at low mach number: Effect of the cavity oscillation mode. *International Journal of Aeroacoustics*, 18(6-7):647–668, 2019.

[150] X. Shan. Effect of an upstream cylinder on the wake dynamics of two tandem cylinders with different diameters at low Reynolds numbers. *Physics of Fluids*, 33(8):083605, 2021.

[151] H. Ding, C. Shu, K. S. Yeo, and D. Xu. Numerical simulation of flows around two circular cylinders by mesh-free least square-based finite difference methods. *International Journal for Numerical Methods in Fluids*, 53(2):305–332, 2007.

[152] B. Sharman, F. Lien, L. Davidson, and C. Norberg. Numerical predictions of low Reynolds number flows over two tandem circular cylinders. *International Journal for Numerical Methods in Fluids*, 47(5):423–447, 2005.

[153] J. A. Fitzpatrick. Flow/acoustic interactions of two cylinders in cross-flow. *Journal of Fluids and Structures*, 17(1):97–113, 2003.

[154] A. Mohany and S. Ziada. Numerical simulation of the flow-sound interaction mechanisms of a single and two-tandem cylinders in cross-flow. *Journal of Pressure Vessel Technology*, 131(3), 2009.

[155] S. L. Finnegan, C. Meskell, and S. Ziada. Experimental investigation of the acoustic power around two tandem cylinders. *Journal of Pressure Vessel Technology*, 132(4), 2010.

[156] T. Igarashi. Characteristics of the flow around two circular cylinders arranged in tandem: 1st report. *Bulletin of JSME*, 24(188):323–331, 1981.

[157] B. C. Vermeire and P. E. Vincent. On the behaviour of fully-discrete flux reconstruction schemes. *Computer Methods in Applied Mechanics and Engineering*, 315:1053–1079, 2017.

[158] R. W. Paterson, P. G. Vogt, M. R. Fink, and C. L. Munch. Vortex noise of isolated airfoils. *Journal of Aircraft*, 10(5):296–302, 1973.

[159] R. E. Longhouse. Vortex shedding noise of low tip speed, axial flow fans. *Journal of Sound and Vibration*, 53(1):25–46, 1977.

[160] H. Arbey and J. Bataille. Noise generated by airfoil profiles placed in a uniform laminar flow. *Journal of Fluid Mechanics*, 134:33–47, 1983.

[161] E. C. Nash, M. V. Lowson, and A. McAlpine. Boundary-layer instability noise on aerofoils. *Journal of Fluid Mechanics*, 382:27–61, 1999.

[162] T. Atobe and T. Ikeda. Flow instability around a 2D airfoil induced by acoustic disturbances at low Reynolds numbers. In *Proc. 27th Congress of Int. Council of Aeronautical Sciences, Ëession*, volume 3, pages 1–13.

[163] T. Ikeda, T. Atobe, and S. Takagi. Direct simulations of trailing-edge noise generation from two-dimensional airfoils at low Reynolds numbers. *Journal of Sound and Vibration*, 331(3):556–574, 2012.

[164] G. Desquesnes, M. Terracol, and P. Sagaut. Numerical investigation of the tone noise mechanism over laminar airfoils. *Journal of Fluid Mechanics*, 591:155–182, 2007.

[165] L. T. Clark. The radiation of sound from an airfoil immersed in a laminar flow. 1971.

[166] A. S. Hersh and R. E. Hayden. Aerodynamic sound radiation from lifting surfaces with and without leading-edge serrations. Technical report, 1971.

[167] C. K. W. Tam. Discrete tones of isolated airfoils. *The Journal of the Acoustical Society of America*, 55(6):1173–1177, 1974.

[168] A. L. Marsden, M. Wang, B. Mohammadi, and P. Moin. Shape optimization for aerodynamic noise control. *Center for Turbulence Research Annual Brief*, pages 241–47, 2001.

[169] A. L. Marsden, M. Wang, P. Koumoutsakos, and P. Moin. Optimal aeroacoustic shape design using approximation modeling. *Cent. Turb. Res. Briefs*, 201:213, 2002.

[170] A. L. Marsden, M. Wang, J. E. Dennis, and P. Moin. Optimal aeroacoustic shape design using the surrogate management framework. *Optimization and Engineering*, 5(2):235–262, 2004.

[171] J-C Jouhaud, P. Sagaut, M. Montagnac, and J. Laurenceau. A surrogate-model based multi-disciplinary shape optimization method with application to a 2D subsonic airfoil. *Computers & Fluids*, 36(3):520–529, 2007.

[172] T. Ikeda and T. Atobe. Numerical studies of acoustic effects on 2D airfoil aerodynamics at a low Reynolds number. In *50th AIAA Aerospace Sciences Meeting including the New Horizons Forum and Aerospace Exposition*, page 700, 2012.

[173] D. J. Maull and L. F. East. Three-dimensional flow in cavities. *Journal of Fluid Mechanics*, 16(4):620–632, 1963.

[174] D. Rockwell and C. Knisely. Observations of the three-dimensional nature of unstable flow past a cavity. *The Physics of Fluids*, 23(3):425–431, 1980.

[175] S. J. Lawson and G. N. Barakos. Review of numerical simulations for high-speed, turbulent cavity flows. *Progress in Aerospace Sciences*, 47(3):186–216, 2011.

[176] X. Gloerfelt, C. Bogey, and C. Bailly. LES of the noise radiated by a flow over a rectangular cavity. In *ERCOFTAC Workshop on LES for Acoustics*, pages 7–8, 2002.

[177] H. Lai and K. H. Luo. A three-dimensional hybrid LES-acoustic analogy method for predicting open-cavity noise. *Flow, Turbulence and Combustion*, 79:55–82, 2007.

[178] X. Gloerfelt. Large-eddy simulation of a high Reynolds number flow over a cavity including radiated noise. In *10th AIAA/CEAS Aeroacoustics Conference*, page 2863, 2004.

[179] P. Welch. The use of fast Fourier transform for the estimation of power spectra: a method based on time averaging over short, modified periodograms. *IEEE Transactions on Audio and Electroacoustics*, 15(2):70–73, 1967.

[180] C. H. K. Williamson. Vortex dynamics in the cylinder wake. *Annual Review of Fluid Mechanics*, 28(1):477–539, 1996.

[181] G. V. Papaioannou, D. K. P. Yue, M. S. Triantafyllou, and G. E. Karniadakis. Three-dimensionality effects in flow around two tandem cylinders. *Journal of Fluid Mechanics*, 558:387–413, 2006.

[182] R. Kojima, T. Nonomura, A. Oyama, and K. Fujii. Large-eddy simulation of low-Reynolds-number flow over thick and thin NACA airfoils. *Journal of Aircraft*, 50(1):187–196, 2013.

[183] K. S. Brentner and F. Farassat. Analytical comparison of the acoustic analogy and Kirchhoff formulation for moving surfaces. *AIAA Journal*, 36(8):1379–1386, 1998.

[184] K. S. Brentner. Prediction of helicopter rotor discrete frequency noise: A computer program incorporating realistic blade motions and advanced acoustic formulation. *Technical Memorandum*, 1986.

[185] F. Farassat and G. P. Succi. A review of propeller discrete frequency noise prediction technology with emphasis on two current methods for time domain calculations. *Journal of Sound and Vibration*, 71(3):399–419, 1980.

[186] A. Najafi-Yazdi, G. A. Brès, and L. Mongeau. An acoustic analogy formulation for moving sources in uniformly moving media. *Proceedings of the Royal Society A: Mathematical, Physical and Engineering Sciences*, 467(2125):144–165, 2011.

[187] G. Ghorbaniasl and C. Lacor. A moving medium formulation for prediction of propeller noise at incidence. *Journal of Sound and Vibration*, 331(1):117–137, 2012.

[188] F. Farassat. *Introduction to Generalized Functions with Applications in Aerodynamics and Aeroacoustics*, volume 3428. National Aeronautics and Space Administration, Langley Research Center, 1994.

[189] K. S. Brentner. Prediction of helicopter rotor discrete frequency noise for three scale models. *Journal of Aircraft*, 25(5):420–427, 1988.

[190] K. S. Brentner and F. Farassat. Modeling aerodynamically generated sound of helicopter rotors. *Progress in Aerospace Sciences*, 39(2-3):83–120, 2003.

[191] F. Farassat. Derivation of Formulations 1 and 1A of Farassat. 2007.

[192] A. S. Lyrintzis. Surface integral methods in computational aeroacoustics—From the (CFD) near-field to the (Acoustic) far-field. *International Journal of Aeroacoustics*, 2(2):95–128, 2003.

[193] P. Di Francescantonio. A new boundary integral formulation for the prediction of sound radiation. *Journal of Sound and Vibration*, 202(4):491–509, 1997.

[194] F. Farassat. *Theory of Noise Generation from Moving Bodies with An Application to Helicopter Rotors*. National Aeronautics and Space Administration, 1975.

[195] D. Lockard. A comparison of Ffowcs Williams-Hawkings solvers for airframe noise applications. In *8th AIAA/CEAS Aeroacoustics Conference & Exhibit*, page 2580, 2002.

[196] D. P. Lockard. An efficient, two-dimensional implementation of the Ffowcs Williams and Hawkings equation. *Journal of Sound and Vibration*, 229(4):897–911, 2000.

[197] G. Ghorbaniasl, Z. Huang, L. Siozos-Rousoulis, and C. Lacor. Analytical acoustic pressure gradient prediction for moving medium problems. *Proceedings of the Royal Society A: Mathematical, Physical and Engineering Sciences*, 471(2184):20150342, 2015.

[198] K. S. Brentner. Numerical algorithms for acoustic integrals with examples for rotor noise prediction. *AIAA Journal*, 35(4):625–630, 1997.

[199] V. L. Wells and A. Y. Han. Acoustics of a moving source in a moving medium with application to propeller noise. *Journal of Sound and Vibration*, 184(4):651–663, 1995.

[200] G. A. Brès, K. S. Brentner, G. Perez, and H. E. Jones. Maneuvering rotorcraft noise prediction. *Journal of Sound and Vibration*, 275(3-5):719–738, 2004.

[201] A. P. Dowling, M. M. Sevik, and J. E. Ffowcs-Williams. Sound and sources of sound. 1984.